N° d'ordre :

الجمهورية الجزائرية الديمقراطية الشعبية

République Algérienne Démocratique et Populaire

وزارة التعليم العالي والبحث العلمي

Ministère de L'enseignement Supérieur et de La Recherche Scientifique

جامعة عين تموشنت بلحاج بوشعيب

Universite Ain Témouchent-Belhadj Bouchaib

Faculté : Faculté des Sciences et de la Technologie
Departement : Sciences de la Matière
Laboratoire : Sciences des Matériaux et leurs Applications

THESE

Présentée pour l'obtention du **diplôme de DOCTORAT**
Domaine : Sciences de la Matière
Filière : Physique
Spécialité : Physique de la matière condensée et ses applications

Par : HADBI Mohammed

Intitulé
Etude des défauts ponctuels dans les demi-Heusler à 18 électrons : méthodes de premiers principes

Soutenue publiquement, le 04 /01/2026 , devant le jury composé de :

Nom & Prénom(s)	Grade	Qualité	Etablissement de rattachement
NEBATTI ECH CHERGUI Abdelkader	Pr	Président	Université Belhadj Bouchaib d'Ain Témouchent
DEMMOUCHE Kamel	MCA	Rapporteur	Université Belhadj Bouchaib - Ain Témouchent
BENCHERIF Kaddour	Pr	Examinateur	Université Belhadj Bouchaib -Ain Témouchent
BENSAID Djillali	Pr	Examinateur	Université Djilali Liabes - Sidi Bel Abbes
MOULAY Nour Eddine	Pr	Examinateur	Université Djilali Liabes - Sidi Bel Abbes

Année Universitaire : 2025/2026

N° d'ordre :

الجمهورية الجزائرية الديمقراطية الشعبية

Democratic and Popular Republic of Algeria

وزارة التعليم العالي والبحث العلمي

Ministry of Higher Education and Scientific Research

جامعة عين تموشنت بلحاج بوشعيب

University of Ain Temouchent-Belhadj Bouchaib

Faculty: Faculty of Science and Technology
Department: Materials Science
Laboratory: Materials Science and Applications Laboratory

THESIS

Submitted in partial fulfillment of the requirements for Doctorate degree in Physics
Domain: Materials science
Field: Physics
Specialization: Condensed Matter Physics and Its Applications

Presented by HADBI Mohammed

Theme

Study of Point Defects in 18-Electron Half-Heusler: A First-Principles Method

Publicly defended on 04/01/2026 , before the jury composed of:

Name & Surname (s)	Grade	Title	Affiliated Institution
NEBATTI ECH CHERGUI Abdelkader	Pr	Chairman	Belhadj Bouchaib University of Ain Témouchent
DEMMOUCHE Kamel	MCA	Supervisor	Belhadj Bouchaib University – Ain Témouchent
BENCHERIF Kaddour	Pr	Member	Belhadj Bouchaib University – Ain Témouchent
BENSAID Djillali	Pr	Member	Djilali Liabes University of Sidi Bel Abbes
MOULAY Nour Eddine	Pr	Member	Djilali Liabes University – Sidi Bel Abbes

Academic Year: 2025/2026

Abstract

This thesis investigates 18-electron half-Heusler compounds TiIrSb, ZrIrSb, TaIrGe, and TaIrSn in terms of their structural, electronic, optical, and thermoelectric properties using first-principles calculations. Particular emphasis is placed on the TiIrSb compound, where the effect of substituting titanium (Ti) atoms with zirconium (Zr) atoms in the $2 \times 2 \times 1$ supercell on its physical properties, including dynamical stability, is examined, in addition to studying the influence of point defects of vacancy and antisite types on its structural, electronic, and optical stability. The VASP package, based on DFT, is employed with the PBE-GGA exchange–correlation functional, together with the Meta-GGA-SCAN functional to improve the accuracy of the predictions, while the calculations are performed within the supercell approach to assess the thermodynamic stability through formation energies and the dynamical stability through phonon calculations. Moreover, the hybrid functional HSE06 is used to investigate the electronic properties of the four compounds TiIrSb, ZrIrSb, TaIrGe, and TaIrSn, aiming at a more accurate description of the band gap and electronic structure.
Keywords: Half-Heusler, point defects, DFT, VASP.

Résumé

Cette thèse porte sur l’étude des composés half-Heusler à 18 électrons TiIrSb, ZrIrSb, TaIrGe et TaIrSn en termes de propriétés structurales, électroniques, optiques et thermoélectriques, au moyen de calculs ab initio. Un accent particulier est mis sur le composé TiIrSb, pour lequel l’effet de la substitution des atomes de titane (Ti) par des atomes de zirconium (Zr) dans la supercellule $2 \times 2 \times 1$ sur ses propriétés physiques, y compris la stabilité dynamique, est examiné, en plus de l’étude de l’influence des défauts ponctuels de type lacune (vacancy) et antisite sur sa stabilité structurale, électronique et optique. Le code VASP, basé sur la DFT, est utilisé avec la fonctionnelle d’échange-corrélation PBE-GGA, ainsi que la fonctionnelle Meta-GGA-SCAN afin d’améliorer la précision des prédictions, tandis que les calculs sont réalisés dans le cadre de l’approche supercellule pour évaluer la stabilité thermodynamique à partir des énergies de formation et la stabilité dynamique à partir du calcul des phonons. De plus, la fonctionnelle hybride HSE06 est employée pour étudier les propriétés électroniques des quatre composés TiIrSb, ZrIrSb, TaIrGe et TaIrSn, dans le but d’obtenir une description plus précise de la bande interdite et de la structure électronique.

Mots clés: Demi-Heusler, défauts ponctuels, DFT, VASP.

ملخص

تتناول هذه الأطروحة دراسة أنصاف هوسلر ذات 18 إلكترونًا للمركّبات TiIrSb و ZrIrSbو TaIrGeو TaIrSn، من حيث البنية والخصائص الإلكترونية والبصرية والكهروحرارية، وذلك بالاعتماد على حسابات المبادئ الأولى. وقد تم التركيز

بشكل خاص على المركّبTiIrSb ، حيث جرى فحص تأثير استبدال ذرات التيتانيوم (Ti) بذرات الزركونيوم (Zr) في الخلية الفائقة $1 \times 2 \times 2$ على خصائصه الفيزيائية، بما في ذلك الاستقرار الديناميكي، إضافةً إلى دراسة تأثير العيوب النقطية من نوع الشغور (vacancy) والعيوب المضادة (antisite) في استقراره البنيوي والإلكتروني والبصري. استُخدمت حزمة VASP المبنية على نظرية دوال الكثافة مع اعتماد تقريب PBE-GGA للدالة التبادلية-الارتباطية، إلى جانب تقريب Meta-GGA-SCAN لتحسين دقة التنبؤات، كما أُنجزت الحسابات ضمن نهج الخلية الفائقة مع تقييم الاستقرار الترموديناميكي من خلال طاقات التكوين، والاستقرار الديناميكي من خلال حساب الفونونات. بالإضافة إلى ذلك، تم استخدام الدالة الهجينة HSE06 لدراسة الخصائص الإلكترونية للمركّبات الأربعة TiIrSb و ZrIrSbو TaIrGeوTaIrSn، بهدف الحصول على توصيف أكثر دقة للفجوة الطاقية والبنية الإلكترونية.
الكلمات المفتاحية: أنصاف هوسلر، العيوب النقطية، DFT، VASP.

Dedication

To my beloved parents, whose unwavering support, guidance, and prayers have been the light that illuminated my path. Their sacrifices and encouragement have been the foundation of my journey, and for that, I will always be grateful.

To my dear wife, my companion and source of strength, whose patience, love, and support have been invaluable throughout this endeavor.

To my precious daughter, *Shadha Al-Yasmin*, whose presence fills our lives with light, joy, and endless love.

To my dear brothers and sisters, whose support and encouragement have always been a driving force in my life.

To my entire family, whose love and presence have given me warmth and reassurance, always being the safe haven I turn to.

This work is dedicated to you all, with deep love, gratitude, and appreciation.

Hadbi_Mohammed

Acknowledgment

Praise be to Allah, by whose grace good deeds are accomplished. I thank Him Almighty for His guidance and support in completing this work. Without His help and mercy, this effort would not have been possible.

I extend my sincere thanks and appreciation to my esteemed supervisor, **Dr. DAMMOUCHE Kamel**, for his continuous support and wise guidance, which played a major role in the completion of this research.

I also express my gratitude to the members of my dissertation committee, **Prof. NEBATTI ECH CHERGUI Abdelkader,** Prof. **BENCHERIF Kaddour,** Prof **BENSAID Djillali and** Prof. **MOULAY Nour Eddine**, for their valuable time, effort, and insightful scientific comments that have enriched this work.

My sincere gratitude also goes to my colleague, **Dr. MELLAH Djallal Eddine**, for his continuous assistance and valuable advice. I would also like to thank my colleagues at **LPM (Laboratoire de Physique des Matériaux), Laghouat**, including **Dr. SERHANI Mohammed Esaid, KHAMLOUL Fakherdinne, BELKHIER Mohammed Lamine, and FODEILI Mohammed Lamine**, for their collaboration, knowledge exchange, and contributions that have significantly enhanced this research.

I am also deeply grateful to **Dr. FADLA Mohamed Abdelilah** *from the* **School of Mathematics and Physics, Queen's University Belfast, United Kingdom**, *for his invaluable support and assistance throughout this journey.*

Finally, I would like to thank my beloved family for their unwavering support and encouragement, and my dear friends who have always been a source of motivation. May Allah reward them all abundantly.

Hadbi_Mohammed

List of Figures

I.1 Crystal structure of (a) Half-Heusler and (b) Full-Heusler compounds[1] . 6

I.2 Periodic table represent Half-Heusler and Full-Heusler compounds. [1–3] . 6

I.3 Types of point defects: (a) vacancy, (b) interstitial atom, (c) small substitutional atom, (d) large substitutional atom, (e) Frenkel defect, and (f) Schottky defect.[4] 8

I.4 Antisite defect 9

I.5 Type of line Defects [5] 9

I.6 Types of Planar Defects: (a) Grain and Grains Boundary, (b) Twin Boundaries.[6] 10

I.7 Types of Planar Defects : (a) Stacking Faults, (b) Phase Boundarie.[7] . . 11

I.8 N–X–$(8-N)$ compounds represent the introduction of a group X element (Ni, Pd, Pt) into a crystal lattice with eight valence electrons. The compounds are classified according to their structural stability, some of which have been reported previously, while others have been predicted to be stable or unstable theoretically. Some of these compounds crystallize in the cubic LiAlSi $F\bar{4}3m$ pattern, and seven major structural types have been identified, with 41 structural types theoretically studied to assess their stability.Where ✓ indicates previously reported compounds, (+) represents previously unreported compounds that are predicted to be stable according to theoretical calculations, (-) indicates unreported compounds that are predicted to be unstable, and ∘ indicates cases whose stability has not been definitively determined[?]. 12

I.9 The $(N+1)$–IX–$(8-N)$ compounds represent the introduction of a group IX element (Co, Rh, Ir) into a crystal lattice with nine valence electrons. The compounds are classified according to their structural stability, some having been reported previously, while others have been predicted to be stable or unstable theoretically. Some of these compounds crystallize in the cubic LiAlSi $F\bar{4}3m$ pattern, and 41 structural types have been analyzed to evaluate their stability..[?] 13
I.10 Comparison of electronic band structures: (a) Band structures of different materials, (b) Direct and indirect bandgap semiconductors [8]. 18

II.1 Schematic of a pseudo wave function and pseudopotentials. 34
II.2 Schematic of : a) Unit cell, b) Pristine (perfect) 222 supercell, c) Defective supercell. 38

III.1 Band structure plots calculated using SCAN and PBE for the ABX (HH) compounds. 46
III.2 Total (TDOS) and Partial (PDOS) density of states plots calculated using SCAN and PBE for the studied compounds. 47
III.3 Band structure plots calculated using the HSE06 hybrid functional for the ABX (HH) compounds. 48
III.4 Total and partial density of states calculated using the HSE06 hybrid functional for the studied compounds. 49
III.5 2D and 3D anisotropy representations of Young's and Bulk moduli for **TiIrSb**. 52
III.6 2D and 3D anisotropy representations of Young's and Bulk moduli for **ZrIrSb**. 53
III.7 2D and 3D anisotropy representations of Young's and Bulk moduli for **TaIrGe**. 54
III.8 2D and 3D anisotropy representations of Young's and Bulk moduli for **TaIrSn**. 55
III.9 Real and imaginary parts of the dielectric function for ABX Half-Heusler. . 56
III.10 Absorption coefficient and reflectivity for ABX Half-Heusler. 57
III.11 Refractive index and extinction coefficient for ABX Half-Heusler. 57
III.12 Energy loss function $L(\omega)$ for ABX Half-Heusler. 57

III.13 Thermoelectric properties of ABX at different temperatures 60
III.14 Structure of XIrSb (X = Ti, Zr) compounds, (a) and (b) represent conventional and primitive cells, respectively. 64
III.15 Schematic representation 2×2×1 perfect supercell of XIrSb (M=Ti, Zr) with 48 atoms. 64
III.16 The lowest energy configurations for each composition of $Zr_xTi_{(1-x)}IrSb$ alloys, determined using the GGA-PBE functional. 66
III.17 The variations of formation energy $E_f[eV/atom]$ (blue line) and enthalpy $\Delta H_f[eV//atom]$(red line) for $Zr_xTi_{1-x}IrSb$ as a function of concentration (x) 68
III.18 phonon band dispersion of bulk structure and partial density of states of the pristine 2x2x1 super-cell. 70
III.19 Phonon band structure and density of states of individual atoms in $Zr_xTi_{1-x}IrSb$ alloys at x={0,0.0625, 0.125, 0.1875. 70
III.20 Phonon band structure and density of states of individual atoms in $Zr_xTi_{1-x}IrSb$ alloys at x=0,0.25, 0.50, 0.75 71
III.21 The band structures of TiIrSb and ZrIrSb are re-displayed for comparison with the defective structures. 73
III.22 Calculated band structure of $Zr_xTi_{1-x}IrSb$ alloys using PBE, (a) x=0.00, (b) x=0.0625, (c) x=0.125, (d) x=0.1875, (e) x=0.25, (f) x=0.5, (g) x=0.75, (h) x=1.00. 73
III.23 Calculated band structure of $Zr_xTi_{1-x}IrSb$ alloys using SCAN, (a) x=0.00, (b) x=0.0625, (c) x=0.125, (d) x=0.1875, (e) x=0.25, (f) x=0.5, (g) x=0.75, (h) x=1.00. 74
III.24 The variation energies band gap values as a function concentrations x of $Zr_xTi_{1-x}IrSb$ alloys using PBE and SCAN. 75
III.25 Total and partial density of states for $Zr_xTi_{1-x}IrSb$ alloys at x= 0, 1, calculated using PBE and SCAN functional. 76
III.26 Total and partial density of states for $Zr_xTi_{1-x}IrSb$ alloys at x= 0.0625, 0.125, 0.1875, 0.25, 0.50, 0.75, calculated using PBE and SCAN functionals. 76
III.27 Variations effective mass $m^*(m_0)$ of electrons and holes in gamma-x and gamma-L direction for $Zr_xTi_{1-x}IrSb$ alloys. 78

III.28 Calculated optical coefficients: (a) Real part $\varepsilon_1(\omega)$ and (b) imaginary part $\varepsilon_2(\omega)$ of the dielectric function. (c) Extinction coefficient . (d) Reflectivity index. (e) Refractive index. (f) Loss energy for each concentration (x). . . 81
III.29 Absorption coefficient of $Zr_xTi_{1-x}IrSb$ alloys as a function of concentration (x) using SCAN approach. 82
III.30 Thermodynamic stability region of the ternary TiIrSb compound. The gray region represents the stability range where the TiIrSb phase is formed, using the GGA-PBE functional. 89
III.31 Formation energy of neutral point defects (vacancies and antisites) as a function of chemical potential variation between rich and poor regions for element i. Here, i represents the removed element in the case of vacancy defects, and the substituted element in the case of antisite defects, using the GGA-PBE functional. 90
III.32 Total and Partial Density of States for TiIrSb 2×2×1 Supercell with Vacancy Defects: (a) for V_{Ti}, (b) for V_{Ir} and (c) V_{Sb}, using SCAN functional. 92
III.33 Band Structure for TiIrSb 2×2×1 Supercell with Vacancy Defects: (a) for V_{Ti}, (b) for V_{Ir} and (c) V_{Sb}, using SCAN functional. 92
III.34 Electronic band structures for the six studied antisite defects in TiIrSb. Each plot shows the influence of antisite substitution on the band gap and electronic states. 93
III.35 Electronic Density of States (DOS) for antisite defects in TiIrSb, ordered according to the sequence used in the band structure analysis. 96
III.36 The optical properties of TiIrSb with and without a vacancy defect, including: (a) Real part of the dielectric function, (b) Imaginary part of the dielectric function, (c) Absorption coefficient, (d) Extinction coefficient, (e) Refractive index, and (f) Refractivity. 102
III.37 The variation of the Loss energy as a function of photon energy for the perfect and defective structures (vacancies defects). 103
III.38 Optical properties of the system with anti-site defects. 105
III.39 The variation of the Loss energy as a function of photon energy for the perfect and defective structures (antisite defects). 106

List of Tables

II.1 Atomic units used in DFT and their equivalents in the International System (SI). 26

III.1 Structural parameters and elastic constants for ABX compounds calculated using PBE (SCAN), with comparison to previous works. Experimental data from [9, 10]; GGA-PBE calculations [11, 12]; GGA-PBEsol [13]; PBE+U and SCAN [14]. 44

III.2 Band-gap values E_g (eV) of the ABX half-Heusler compounds: this work (PBE, SCAN, HSE06) and selected literature data. 45

III.3 The number of possible substitutions in sites $N_S[Sites]$, the total number of configurations (C_T), and the number of inequivalent configurations (C) calculated for $Zr_xTi_{(1-x)}IrSb$ alloys using the SOD package. 66

III.4 The calculated energy band gap Eg (eV) of $Zr_xTi_{1-x}IrSb$ alloys using PBE and SCAN. 74

III.5 Relative distortions (%) and density (g/cm^3) for the pristine and defective structures using PBE and SCAN functionals, with volume change (%) relative to the pristine structure. 87

III.6 Magnetic moments and electronic impact of vacancies and antisite defects in TiIrSb. 99

Contents

List of Figures I

List of Tables V

Contents VI

Introduction 1

I Theoretical Framework 4

I.1 Introduction . . . 4

I.2 Literature Review . . . 5

I.2.1 Heusler Alloys: Overview and Applications . . . 5

I.3 The defects in material . . . 6

I.4 Previous Studies on ABX Half-Heusler compounds . . . 11

I.5 Physical Properties (Overview) . . . 15

I.5.1 Structural, Elastic and Mechanical Properties . . . 15

I.5.2 Electronic Properties . . . 17

I.5.3 Optical Properties . . . 19

I.5.4 Thermoelectric Properties . . . 20

I.6 Conclusion . . . 22

II Principles and Theoretical Approach 24

II.1 Introduction . . . 24

II.2 The Schrodinger equation . . . 25

II.3 The Born-Oppenheimer Approximation . . . 26

II.4 Hartree and Hartree-Fock approximation . . . 27

II.5 Density Functional Theory (DFT) . . . 28

II.6 Thomas-Fermi model . . . 28
II.7 Hohenberg-Kohn theorems . . . 29
II.8 Exchange-Correlation Approximation . . . 30
II.9 Calculation Methods . . . 33
II.10 Technical Calculation . . . 35
II.11 Calculation Codes and Analyses Tools . . . 35
II.12 Ab-intio Point Defects Calculation . . . 37
II.13 Conclusion . . . 40

III Results and Discussion **41**
III.1 18-Electrons ABX Half-Heusler Alloys Properties . . . 41
III.1.1 Introduction . . . 41
III.1.2 Computational Details . . . 41
III.1.3 Structural Properties . . . 42
III.1.4 Electronic Properties . . . 43
III.1.5 Elastic and Mechanical Properties . . . 49
III.1.6 Optical Properties . . . 55
III.1.7 Thermoelectric properties of ABX Half-Heusler alloys . . . 58
III.1.8 Conclusion . . . 60
III.2 Theoretical insights into off-stoichiometric $Zr_xTi_{1-x}IrSb$ . . . 62
III.2.1 Introduction . . . 62
III.2.2 Computational methodology . . . 63
III.2.3 Configuration built using the Site Occupation Disorder (SOD) . . . 65
III.2.4 Thermodynamic Stability of $Zr_xTi_{1-x}IrSb$ Alloys . . . 67
III.2.5 Dynamical Stability . . . 68
III.2.6 Electronic Properties of $Zr_xTi_{1-x}IrSb$ Alloys . . . 71
III.2.7 Optical Properties . . . 77
III.2.8 Conclusion . . . 82
III.3 Vacancies and Antisite Point Defects Impact Study in the TiIrSb Structure 84
III.3.1 Introduction . . . 84
III.3.2 Calculation details . . . 84
III.3.3 Effect of Defects on the Crystal Structure . . . 85
III.3.4 Energies and Stability Analysis . . . 87

III.3.5 Effects of Vacancies on Electronic Properties 91
III.3.6 Effects of Antisite Point Defects on Electronic Properties 92
III.3.7 The effect of defects on magnetic and electronic properties 98
III.3.8 Impact of Vacancies and Anti-site Defects on Optical Properties . . 100
III.3.9 Conclusion 107

Summary and conclusion **109**

Bibliography **112**

Introduction

Background

Materials science has witnessed remarkable progress in recent decades, thanks to rapid developments in computer modeling and simulation techniques. These techniques have become an indispensable tool for studying and characterizing the physical and chemical properties of materials at the atomic level [15, 16]. These methodologies provide profound insights into the electronic structure of materials and enable an understanding of their structural dynamics with unprecedented precision, contributing to improved materials design and the development of new, highly efficient applications. Among the crystalline systems that have received increasing attention in recent years are half-Heusler (HH) compounds, which are among the most promising materials due to their versatility in various technological fields, from thermoelectric devices to solar cells, advanced electronics, and energy conversion systems.

Half-Heusler compounds consist of three elements with the general formula ABX, where A and B represent metallic elements, often transition metals, and X is a main group element in the periodic table. These compounds have a crystal structure following the $F\bar{4}3m$ space group, where each of the three elements occupies a specific position within the crystal lattice, resulting in a geometrically ordered structure. This unique structure allows Half-Heusler compounds to comply with the 18-electron rule, ensuring electronic stability through a full valence band. This gives these materials a suitable energy gap between semiconductors and insulators [17–19], making them candidates for a wide range of electronic and thermoelectric applications.

Furthermore, Half-Heusler compounds combine metallic and semiconductor properties, offering them multiple potential technological applications. For example, these materials are used in thermoelectric conversion due to their ability to achieve a high Seebeck coefficient and low lattice thermal conductivity, making them prime candidates for im-

proving the efficiency of converting thermal energy to electrical energy. Furthermore, some half-Heusler compounds exhibit magnetic properties, opening the way for their use in spintronics, an emerging technology that aims to harness the magnetic moment of electrons to improve the performance of electronic devices.

Although Half-Heusler have distinctive properties that make them strong candidates for many applications, the presence of point defects can significantly impact their performance [20, 21]. Structural defects, such as atomic vacancies, anti-site defects, and lattice dislocations, play a critical role in modifying the electronic properties, electrical conductivity, and structural stability of these materials. In some cases, point defects can improve the functional performance of the material, such as controlling the concentration of charge carriers in semiconductors, enhancing the material's efficiency in applications such as solar cells and thermoelectrics[22, 23]. However, structural defects may be undesirable in some other contexts, as they can contribute to reduced thermal stability or limit the efficiency of electronic transport, making their study essential to understanding how to improve the performance of these materials.

Main objectives of this thesis

This study aims to analyze the physical and electronic properties of iridium (Ir)-containing Half-Heusler compounds, focusing on the effect of substitution and point defects. The main objectives can be summarized as follows:

- Study the physical properties of four 18-electron ABX Half-Heusler compounds, namely: TaIrGe, TaIrSn, TiIrSb, and ZrIrSb, by analyzing their structural, electronic, and optical properties.
- Analysis of the effect of titanium (Ti) substitution by zirconium (Zr) in the TiIrSb compound in order to understand the effect of the gradual formation towards the ZrIrSb compound on electronic transitions, physical properties, and dynamic stability.
- Study the effect of point defects, including vacancies and anti-sits on the TiIrSb compound, focusing on their effect on thermodynamic stability and electronic properties.

Thesis Structure

In this thesis, we present the following structure:

1. **Introduction**
2. **Literature Review and Theoretical Background**
   (a) Literature Review
   (b) Principles and Theoretical Approach
3. **Results and Discussion**
   (a) 18-Electrons ABX Half-Heusler Alloys Properties
   (b) Theoretical insights into off-stoichiometric $Zr_xTi_{1-x}IrSb$
   (c) Vacancies and antisites point defects impact study in the TiIrSb structure
4. **Conclusion**

Chapter I

Theoretical Framework

I.1 Introduction

Theoretical study is one of the basic pillars of any scientific research, as it enables the researcher to understand the physical and chemical foundations that govern the phenomena under study, and also establishes a clear cognitive framework that helps in interpreting the results later. In this context, this chapter focuses on reviewing the basic concepts and theoretical models related to the structural, electronic, thermoelectric and optical properties of Half-Heusler Compounds.

Half-Heusler compounds are characterized by having a regular crystal structure belonging to the cubic system, and they often crystallize within the space group **Space Group:** $F\bar{4}3m$

These compounds are known for their diverse electronic properties that range between metallic, semi-metallic and semi-conductive behavior, which makes them promising materials for applications in various fields, such as thermoelectric conversion, electronic and photovoltaic devices. In this context, this section reviews the basic theoretical background on which our study is based, starting from the structural properties and basic equations describing the interaction between electrons and the crystal lattice, through the concepts related to electronic structure and determining the energy gap (band gap), and reaching the laws governing the thermoelectric and optical properties of these materials. Numerical methods based on Density Functional Theory (DFT) are also addressed as the main tool used in this work.

I.2 Literature Review

I.2.1 Heusler Alloys: Overview and Applications

Heusler compounds have received extensive attention in theoretical and experimental studies due to their promising physical properties in many fields and their manufacturability and use in various modern technologies[24, 25]. The Heusler compounds are ternary metal compounds with simple crystal structure, which has been of great interest in the past decades. It was found that these alloys have many advantages, such as the ability to convert waste heat into electrical energy, or what is known as thermoelectric materials[26, 27], as well as their use in spin-electronics devices due to their electronic composition[28, 29], they are ferromagnetic semi-metallic materials[30], and antiferromagnets,[26] also classified with semiconductors and even superconductors[31, 32], in addition to other applications that we will mention later.

The discovery of these materials dates back to 1903, when researcher Fritz Heussler discovered these alloys through his study of the compound Cu_2MnAl, consisting of copper, aluminum, and manganese and found that they are ferromagnetic compounds. Hence, these materials were known by his name[3, 33]. According to the chemical formula, Heusler alloys are divided into two groups, Half-Heussler alloys with the formula ABX and full Heusler alloys with the formula AB_2X, where A and B are transition metals and the third element X is a non-magnetic element belonging to groups III to V of the periodic table (see Figure I.2. These alloys crystallize in face-centered cubes, FCC with $\mathbf{C1}_b$ structure, F-43m (spcac group number: 216) for Half Heusler alloys, and to obtain Full-Heusler compounds, B atoms are inserted into tetrahedral sites where the B elements form a cubic sublattice within the full cube, see Figure I.1, then the group space becomes Fm-3m (No. 225) $L2_1$ [3, 33, 34], according to the initial model of Cu_2MnAl[35]. Changing the chemical formula of full Heusler compounds to the formula A_2BX gives us new sub-family of compounds called inverse Heusler compounds. The alloy Hg_2CuTi is the prototype of the structure[36, 37].All of the above were about ternary Heusler compounds, while quaternary compounds are a type of Heusler compounds that contain four elements in their chemical structure, and their formula is AA'BX. These compounds are characterized by the presence of additional atoms compared to full or half-Heusler compounds, which gives them distinctive physical properties, and they are used in a variety of applications. Examples include ZrCoTiSi, ZrCoTiGe, ZrCoTiGa and ZrCoTiAl[38], A

quaternary Heusler structure with altered symmetry is obtained, the so-called LiMgPdSn or Y-type structure (space group F43m) [39].

Diverse physical properties of Heusler alloys (full or Half), They can be metallic, half-metallic, or semiconducting. Show magnetic properties, such as ferromagnetism or anti-ferromagnetism. Distinctive mechanical, electrical, and thermoelectric properties[19, 40]. Made them used in the manufacture of microelectronic devices, such as thermal conductors and temperature sensors[41]. Half-metallic Heusler alloys are used in spintronics due to their high electronic polarization[42, 43]. Due to their flexible chemical structure, their properties can be easily changed by switching between elements or creating point defects (such as vacancies, interstitials, substitutions, etc.)[44–47].

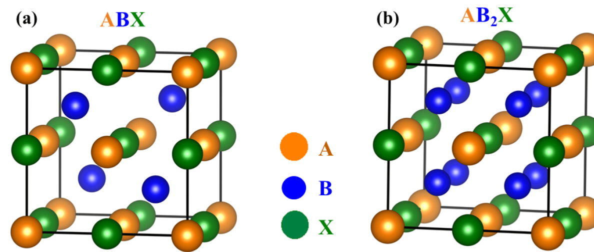

Figure I.1: Crystal structure of (a) Half-Heusler and (b) Full-Heusler compounds[1]

Figure I.2: Periodic table represent Half-Heusler and Full-Heusler compounds. [1–3]

I.3 The defects in material

The arrangement of atoms in crystals in a specific way arranged in a symmetrical order has made it possible to classify them into main groups and specific subgroups (Braves lattice) [4, 48], groups that we can say are very ideal without any defects, and due to the

effects of temperature and pressure according to the principles of thermodynamics, their existence in nature is rare and almost non-existent, or the manufacture of materials with perfect single crystals (single crystal) is very difficult. Even the properties of materials that are sought for certain applications may not be available in compounds with an ideal structure.

In order to improve certain functions of materials, researchers resort to changing the ideal arrangement of crystals by adding an extraneous atom within super-crystals in interstitial positions, replacing an atom with another in its place, or by removing one of the atoms from the sites in large crystals, which causes irregularity in the crystals, and this is what we call crystal defects. The concentration of defects can be expressed according to the Boltzmann relation[48]:

$$n = Ne^{-\frac{\Delta H_f}{k_B T}} \tag{I.1}$$

where N is the number of available sites in the crystal, ΔH_f is the defect formation energy, k_B is the Boltzmann constant, and T represent the temperature. The formation energy of defects energy can be calculated using the first principle-based. The presence of defects within crystals leads to symmetry breaking, which contributes to the presence of local distortions that affect the energy levels of the electron in the energy gap of semiconductors.

For example, in order to increase the strength and hardness of iron, very small amounts of carbon (impurities) are added to molten iron during its manufacture and formation.

To increase the conductivity efficiency of pure semiconductors, they are doped with other pentavalent atoms in order to increase the negative charge carriers (electrons) of the N-type semiconductor, or trivalent atoms in order to increase the number of positive charge carriers (holes) to become a P-type semiconductor[48], for example, doping the pure silicon semiconductor by pentavalent arsenic atoms, or tirivalent galium atoms, etc[49]. as a brief definition of crystal defects, they are changes that occur in the ideal crystal arrangement and play an important role in determining the physical and chemical properties of materials and improving them (structural, elastic, electrical, thermoelectric, optical, etc.) [4, 48].

Defects in the material are divided into points, linear, planar, and volume. We will present brief definitions for each one of them.

Point defects

Point defects (zero-dimension) are a type of crystalline defect that occurs at the atomic level in solid materials. These defects can significantly affect the physical and chemical properties of materials, such as electrical, thermal, and mechanical properties[4]. Point defects are usually classified into:

- Vacancy: The absence (removal) of an atom from its location within the crystal lattice, see Figure:I.3(a)

.

- Interstitial: An atom present in a place not assigned to it in the crystal lattice (within the interstitial sites between atoms), see Figure:I.3(b).
- Substitutional defect: occurs when an atom of another element replaces an atom of the main element in the crystal lattice, see Figure:I.3(c;d).
- Frenkel defect: A defect is formed when a smaller atom or ion (usually a cation) leaves its original location in the structure, creating a void and settling into a nearby location as an interstitial atom, see Figure:I.3(e)..
- Schottky defect: A Schottky defect is a point defect that occurs when an atom leaves its position in the crystal lattice and settles on the surface of the crystal, see Figure:I.3(f).
- Antisite defect: Occurs when an atom moves from its normal location in the crystal lattice to a location reserved for another type of atom, see Figure:I.4.

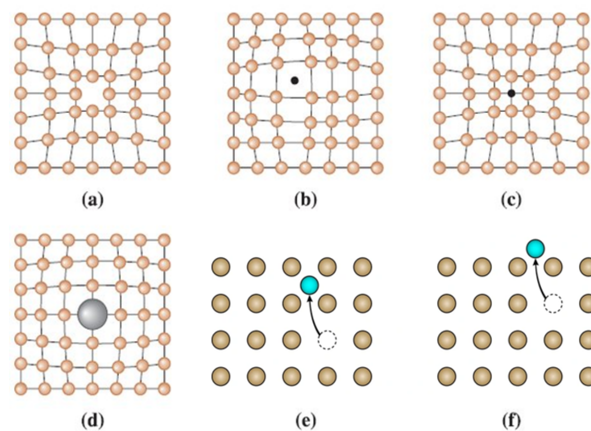

Figure I.3: Types of point defects: (a) vacancy, (b) interstitial atom, (c) small substitutional atom, (d) large substitutional atom, (e) Frenkel defect, and (f) Schottky defect.[4]

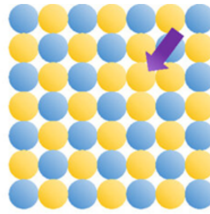

Figure I.4: Antisite defect

Line Defects

Linear defects (One-Dimension), also known as dislocations, are a type of crystal defect that occurs when atoms in a material are arranged irregularly along a particular line within the crystal lattice.

Types of Linear Defects

- Edge Dislocations: Occurs when there is an extra plane of atoms partially inserted into the crystal lattice. This type causes stress on the lattice in one area and tension in another. It is represented by a line of dislocations that is perpendicular to the direction of motion.

- Screw Dislocations: Occurs as a result of the crystal lattice being displaced in a spiral manner along the line of dislocations. This type is usually caused by shear forces.It is represented by a line of dislocations that is parallel to the direction of motion.

- Mixed Dislocations: Combine the properties of edge dislocations and screw dislocations.

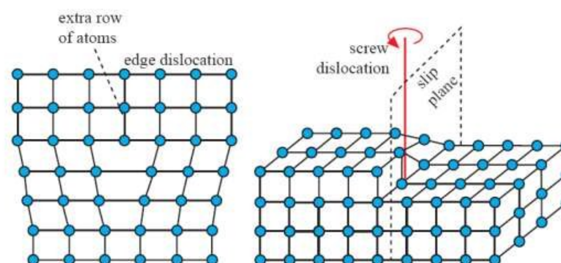

Figure I.5: Type of line Defects [5]

Planar Defects

Planar defects (Two-Dimensions) are a type of crystalline defect that occurs on a surface or entire plane within the crystal lattice.

Types of Planar Defects

- Grain Boundaries: They occur when two or more grains with different atomic arrangement meet. These boundaries are irregular areas that affect mechanical properties such as ductility and strength (Figure:I.6 (a)).
- Twin Boundaries: They occur when atoms are mirrored across a specific plane (Figure:I.6 (b)).
- Stacking Faults: They occur when there is an incorrect arrangement of atomic layers. They cause distortion of the crystal lattice and may affect mechanical properties (Figure:I.7 (a)).
- Phase Boundaries: They occur when two different materials or two different phases meet within the material. They are observed in composite materials and alloys (Figure:I.7 (b)).

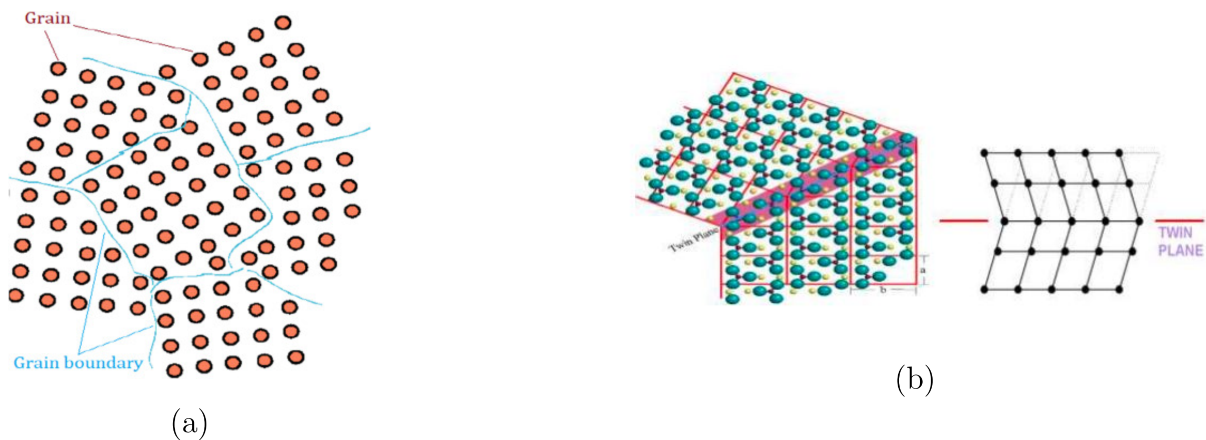

(a)

(b)

Figure I.6: Types of Planar Defects: (a) Grain and Grains Boundary, (b) Twin Boundaries.[6]

Volumetric Defects

Volumetric defects, or bulk defects (Three- Dimensions) are disturbances in the crystal lattice that occur on a large scale, covering relatively large regions within the material.

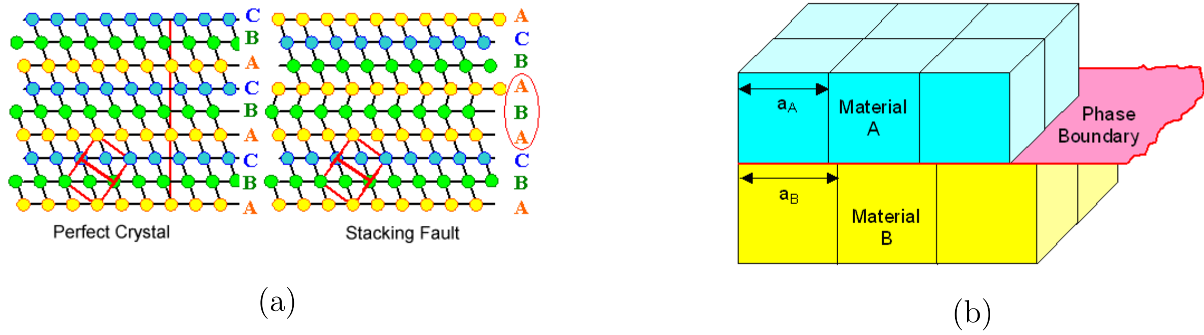

Figure I.7: Types of Planar Defects : (a) Stacking Faults, (b) Phase Boundarie.[7]

- Precipitates: Small aggregates of atoms of a second substance within the original substance.
- Inclusions: Foreign particles or atoms trapped within a substance.
- Voids: Areas completely devoid of atoms or ions, created by defects in the casting process or rapid cooling.
- Cracks: Fractures within a material that may be superficial or internal. Result in reduced strength and fracture toughness. Occur as a result of stress or defects during manufacturing.

I.4 Previous Studies on ABX Half-Heusler compounds

As mentioned earlier, Half-Heusler compounds, with the general formula ABX where A and B are metal elements and X is a main group element, are promising materials for many applications, especially in the fields of optoelectronics and thermoelectrics[3, 33]. These compounds are characterized by their unique crystalline structure and distinctive electronic properties, which have made them the focus of many theoretical and experimental studies. The following is a review of the most important previous studies that dealt with these compounds:

Many previous studies have focused on known reported compounds, while a large number of theoretically possible compounds remain unexplored, despite their potential to have important functional properties. In this context, Romain Gautier and colleagues investigated the possibility of predicting previously undiscovered Half-Heusler compounds belonging to the ABX class with 18 valence electrons. Although this class includes 483 possible compounds, experimental studies have been limited to only 83 compounds[9].

The researchers relied on thermodynamic calculations to study 400 previously unreported compounds, and found that 54 of them are theoretically stable. Of these compounds, 15 were synthesized in the laboratory, and their structures were confirmed by X-ray diffraction techniques with theoretical predictions[?].

The results of the study indicate that some of the newly discovered compounds may have distinct electronic and functional properties, including transparent conductivity, thermoelectric properties, and semimetallic topology. This study highlights the importance of using advanced theoretical modeling as an effective tool for discovering new compounds with promising applications in the fields of energy and advanced electronics.

N–X–(8–N)

I–X–VII

	Ni	Pd	Pt
Rb Cl	–	–	–
K Cl	–	–	–
Na Cl	–	–	–
Li Cl	–	–	–
Au Cl	–	–	–
Ag Cl	–	–	–
Cu Cl	–	–	–
Rb F	–	–	–
K F	–	–	–
Na F	–	–	–
Li F	–	–	–
Au F	–	–	–
Ag F	–	–	–
Cu F	–	–	–

II–X–VI

	Ni	Pd	Pt		Ni	Pd	Pt
Hg S	–	–	–	Hg Te	–	–	○
Cd S	–	–	–	Cd Te	–	–	–
Zn S	–	–	–	Zn Te	–	–	–
Ba S	–	–	–	Ba Te	–	–	–
Sr S	–	–	–	Sr Te	–	–	–
Ca S	–	–	–	Ca Te	–	–	–
Mg S	–	–	–	Mg Te	–	+	–
Be S	–	–	–	Be Te	–	–	–
Hg O	–	–	–	Hg Se	–	–	–
Cd O	–	–	–	Cd Se	–	–	–
Zn O	–	–	–	Zn Se	–	–	–
Ba O	–	–	–	Ba Se	–	–	–
Sr O	–	–	–	Sr Se	–	–	–
Ca O	–	–	–	Ca Se	–	–	–
Mg O	–	–	–	Mg Se	–	–	–
Be O	–	–	–	Be Se	–	–	–

III–X–V

	Ni	Pd	Pt		Ni	Pd	Pt
In Bi	○	–	–	La Bi	–	✓	✓
Ga Bi	+	–	○	Y Bi	✓	✓	✓
Al Bi	–	–	–	Sc Bi	✓	✓	+
In Sb	+	+	+	La Sb	✓	✓	✓
Ga Sb	+	–	+	Y Sb	✓	✓	✓
Al Sb	+	–	+	Sc Sb	✓	✓	✓
In As	–	–	–	La As	+	✓	+
Ga As	–	–	–	Y As	+	+	✓
Al As	+	–	–	Sc As	+	+	–
In P	–	–	–	La P	✓	✓	✓
Ga P	–	–	–	Y P	✓	+	✓
Al P	+	–	–	Sc P	✓	+	✓
In N	–	–	–	La N	+	–	–
Ga N	–	–	–	Y N	–	–	–
Al N	–	–	–	Sc N	–	–	–

IV–X–IV

	Ni	Pd	Pt
Hf Pb	+	+	+
Zr Pb	+	+	+
Ti Pb	–	–	–
Hf Sn	✓	✓	✓
Zr Sn	✓	✓	✓
Ti Sn	✓	+	✓
Hf Ge	✓	✓	✓
Zr Ge	✓	✓	✓
Ti Ge	✓	✓	✓
Hf Si	✓	✓	✓
Zr Si	✓	✓	✓
Ti Si	✓	✓	✓
Hf C	–	–	–
Zr C	–	–	–
Ti C	–	–	–

Figure I.8: N–X–$(8-N)$ compounds represent the introduction of a group X element (Ni, Pd, Pt) into a crystal lattice with eight valence electrons. The compounds are classified according to their structural stability, some of which have been reported previously, while others have been predicted to be stable or unstable theoretically. Some of these compounds crystallize in the cubic LiAlSi $F\bar{4}3m$ pattern, and seven major structural types have been identified, with 41 structural types theoretically studied to assess their stability.Where ✓ indicates previously reported compounds, (+) represents previously unreported compounds that are predicted to be stable according to theoretical calculations, (-) indicates unreported compounds that are predicted to be unstable, and ∘ indicates cases whose stability has not been definitively determined[?].

(N+1)–IX–(8–N)

II–IX–VII

	Co	Rh	Ir
Hg Cl	–	–	–
Cd Cl	–	–	–
Zn Cl	–	–	–
Ba Cl	–	–	–
Sr Cl	–	–	–
Ca Cl	–	–	–
Mg Cl	–	–	–
Be Cl	–	–	–
Hg F	–	–	–
Cd F	–	–	–
Zn F	–	–	–
Ba F	–	–	o
Sr F	–	–	–
Ca F	–	–	–
Mg F	–	–	–
Be F	–	–	–

III–IX–VI

	Co	Rh	Ir
In Te	–	–	–
Ga Te	–	–	+
Al Te	–	–	–
In Se	–	–	–
Ga Se	–	–	–
Al Se	–	–	+
In S	–	–	–
Ga S	–	–	–
Al S	–	–	–
In O	–	–	–
Ga O	–	–	–
Al O	–	–	–

	Co	Rh	Ir
La Te	–	–	–
Y Te	–	–	–
Sc Te	–	+	–
La Se	–	–	–
Y Se	–	–	–
Sc Se	–	–	–
La S	–	–	–
Y S	–	–	–
Sc S	–	–	–
La O	–	–	–
Y O	–	–	–
Sc O	–	–	–

IV–IX–V

	Co	Rh	Ir
Hf Bi	–	+	+
Zr Bi	✓	+	+
Ti Bi	–	–	–
Hf Sb	✓	✓	+
Zr Sb	✓	✓	+
Ti Sb	✓	✓	+
Hf As	✓	+	+
Zr As	–	✓	+
Ti As	✓	✓	+
Hf P	✓	+	+
Zr P	✓	✓	✓
Ti P	✓	+	+
Hf N	–	–	–
Zr N	–	–	–
Ti N	–	–	–

V–IX–IV

	Co	Rh	Ir
Ta Pb	–	–	–
Nb Pb	–	–	–
V Pb	–	–	–
Ta Sn	+	+	+
Nb Sn	✓	✓	✓
V Sn	–	–	–
Ta Ge	✓	✓	+
Nb Ge	✓	✓	✓
V Ge	✓	+	+
Ta Si	✓	✓	✓
Nb Si	✓	✓	✓
V Si	✓	+	+
Ta C	–	–	–
Nb C	–	–	–
V C	–	–	–

Figure I.9: The $(N+1)$–IX–$(8-N)$ compounds represent the introduction of a group IX element (Co, Rh, Ir) into a crystal lattice with nine valence electrons. The compounds are classified according to their structural stability, some having been reported previously, while others have been predicted to be stable or unstable theoretically. Some of these compounds crystallize in the cubic LiAlSi $F\bar{4}3m$ pattern, and 41 structural types have been analyzed to evaluate their stability..[?]

Miller Elly Shatsala and colleagues' study, "Thermodynamic Stability of ABX Heavy Elements of TaIrGe, TiIrSb, TaIrSn and ZrIrSb TCOs Using the Half-Heusler Technique," focuses on using electronic structure theory to design and evaluate the stability of ABX heavy elements, such as TaIrGe, TiIrSb, TaIrSn, and ZrIrSb. The study aims to explore new materials with functional applications in areas such as transparent conductors (TCOs), which are used in solar cell technologies, light-emitting diodes (LEDs), and flat-panel displays[50].

These compounds have the unique property of combining optical transparency with electrical conductivity, a property rarely found in conventional materials, as insulators are typically transparent but lack electrical conductivity, while metals are conductive but optically opaque.

The study relied on computational modeling techniques to evaluate the stability of these compounds dynamically and thermally, focusing on the effect of atomic number and electronic structure in achieving specific electron vacancy levels, which contributes to

improving electrical conductivity without affecting transparency. The results showed that the stability of these compounds depends on the crystal growth conditions, where stability is higher in environments rich in element X and poor in elements A and B. This study highlights the importance of using advanced theoretical predictions in the design of new materials, paving the way for the discovery of high-performance transparent conductors with great potential in future technological applications, especially in the fields of energy and advanced electronics.

Poulmi Dey *et all* investigated the effect of interstitial defects on the electronic structure of Half-Heusler thermoelectric alloys, which obey the 18-electron rule. The challenge lies in the discrepancy between theoretical predictions and experimental results on the type of charge carriers in these alloys[51].

First-hand calculations showed that interstitial defects of Ni and Co elements are the most stable, significantly affecting the location of the Fermi level and the value of the band gap, achieving greater agreement with experimental results.

The study suggests that controlling interstitial defects could be an effective way to modify electronic and thermoelectric properties, opening the way to design materials that are more efficient in converting thermal energy into electrical energy.

Mi Zhong *et all* studied four 18-electron Half-Heusler compounds (TaIrGe, TaIrSn, ZrIrSb, and TiIrSb) to understand their behavior as transparent conductors[11]. The study presented two key points:

1. Effect of hole-killing defects: TaIrGe was found to have more hole-killing defects than ZrIrSb, leading to a lower hole concentration and thus lower conductivity in TaIrGe compared to ZrIrSb.

2. Effective mass of holes: The study suggests that the effective mass of holes near the sub-valence band maximum (Sub-VBM) can be used to predict the electrical transport performance of materials. The results showed that TaIrGe and TaIrSn have more promising transport performance than TiIrSb and ZrIrSb.

3. In addition, the study provided an analysis of the mechanical properties of these compounds, indicating that TaIrGe, TaIrSn, ZrIrSb, and TiIrSb have high ductility, making them promising materials for ductile transparent conductors.

MeLLAH *et all* studied the structural and electronic properties of two transparent Half-Heusler conductors (TiIrSb and ZrIrSb) using DFT, focusing on the effect of

exchange-correlation (XC) and spin-orbit coupling (SOC). The study showed that SCAN gives a larger band gap compared to PBE, which improves the accuracy of electronic predictions. SOC also leads to a significant splitting of the VBM, which increases with increasing atomic weight of element X, making it a key factor in determining the electronic structure and band gap of these compounds[14].

I.5 Physical Properties (Overview)

Physical properties play a pivotal role in determining the behavior of materials and their response to different conditions, making them a key factor in many scientific and industrial applications. The analysis of these properties includes the study of structural, mechanical, electronic, optical, and thermal aspects, which contribute to understanding the nature of the material and its performance in different environments. These studies often rely on density functional theory (DFT) and quantum mechanical calculation tools, where the effect of atomic configuration, substitutions, and point defects on the stability and functional properties of the material are explored[4, 48].

I.5.1 Structural, Elastic and Mechanical Properties

Structural properties express the atomic structure of a substance, determining how atoms are arranged within a crystal lattice and how this affects its stability and other physical properties. The study of structural properties depends on determining the crystal structure, lattice constants, volumetric volume, and atomic density. Crystal structure describes the arrangement of atoms within a substance according to a specific periodic system. Crystalline materials are classified according to different crystal systems, such as cubic, hexagonal..., and orthorhombic. The type of crystal structure is determined by X-ray diffraction (XRD) techniques or by theoretical calculations using density functional theory (DFT). The lattice constant is defined as the distance between atoms in a crystal structure and is a fundamental factor that determines the cohesion and stability of a material. It can be calculated experimentally via XRD analysis or theoretically using DFT through the principle of lowest total energy of the material. The stability of the structure is checked by calculating the formation energy and the total energy of the system. The stability of the structure requires that the formation energy be negative, indicating that the material is thermally stable. Its dynamic stability is also studied by calculating

the vibrational frequencies (phonon dispersion) to ensure that there are no imaginary frequencies, indicating that the material is stable at absolute zero temperature[4, 48].

Elastic properties are a key factor in determining a material's ability to withstand external stresses and resist deformation. They reflect how well a material responds to applied forces and how well it can return to its original shape after the forces are removed[48]. These properties can be evaluated by calculating elastic constants, which provide an accurate view of a material's stability and mechanical behavior, helping to understand how stiff or flexible it is in different applications. Elastic constants are defined as coefficients that determine the relationship between stress and deformation according to Hooke's law[4, 48, 52]:

$$\sigma_{ij} = C_{ijkl}\varepsilon_{kl} \tag{I.2}$$

where σ is the stress, C_{ijkl} is the elastic constant matrix, and ε_{kl} is the deformation.

The values of C_{ij} vary depending on the crystal symmetry. In cubic materials, there are only three main constants:

- C_{11}: Expresses the response of the material to longitudinal stress.
- C_{12}: Reflects the effect of lateral deformations.
- C_{44}: Represents the resistance of the material to shear deformations.

Elasticity constants matrix for cubic crystal system:

$$C_{ij} = \begin{bmatrix} C_{11} & C_{12} & C_{12} & 0 & 0 & 0 \\ C_{12} & C_{11} & C_{12} & 0 & 0 & 0 \\ C_{12} & C_{12} & C_{11} & 0 & 0 & 0 \\ 0 & 0 & 0 & C_{44} & 0 & 0 \\ 0 & 0 & 0 & 0 & C_{44} & 0 \\ 0 & 0 & 0 & 0 & 0 & C_{44} \end{bmatrix} \tag{I.3}$$

Bulk Modulus (B)

Represents the material's resistance to compression:

$$B = \frac{C_{11} + 2C_{12}}{3} \tag{I.4}$$

Shear Modulus (G)

Reflects the material's resistance to shear deformations:

$$G = \frac{C_{11} - C_{12} + 3C_{44}}{5} \tag{I.5}$$

Young's Modulus (E)

Indicates the stiffness of the material under tensile stress:

$$E = \frac{9BG}{3B + G} \tag{I.6}$$

Poisson's Ratio (ν)

Provides information about the nature of bonding in the material:

$$\nu = \frac{3B - 2G}{2(3B + G)} \tag{I.7}$$

Importance of Elastic Properties

- Determine the mechanical stability of the material.
- Predict the behavior of the material under different stresses.
- Evaluate its potential for use in structural and mechanical applications.

I.5.2 Electronic Properties

Electronic properties are a key factor in determining the behavior and functional properties of materials, making their study essential to understanding their potential in advanced technological applications, such as microelectronics, photovoltaics, and thermoelectric materials. The analysis of these properties relies on density functional theory (DFT), which provides an accurate picture of the electronic band structure and density of electronic states, enabling prediction of the performance and electronic stability of materials[4, 48**?**].

The electronic band structure reflects the distribution of energy levels within a material and is a fundamental element in determining its electronic behavior. This structure is

analyzed by studying the relationship between electron energy and crystal momentum, which allows materials to be classified into the following categories:

- Insulators: They have a wide band gap that prevents the movement of electrons at room temperature, making them non-conductors of electricity.
- Semiconductors: They have a relatively narrow band gap, which enables electrons to move when sufficient energy is available, which makes them essential in electronic applications.
- Metals: They do not have a band gap, as the energy bands overlap, allowing electrons to move freely, making them effective conductors of electricity.

Analyzing the electronic band structure is essential for understanding the electronic properties of materials and determining their suitability for various technological applications, such as microelectronics and thermoelectric materials.

The density of states (DOS) of electrons expresses the number of electronic states available per unit energy at a given level, allowing us to understand how electrons are distributed across different energy bands. The density of states can be classified according to the nature of the material as follows:

In insulators and semiconductors: the density of states is zero within the energy gap (band gap), which limits the transfer of electrons under normal conditions.

In metals: the density of states extends across the Fermi level E_F, allowing free electrons to contribute to electrical conduction.

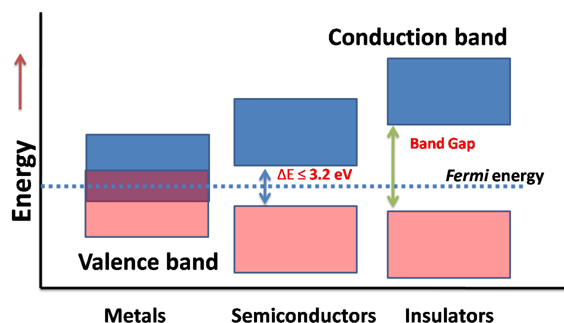

(a) Electronic band structure for insulators, semiconductors, and conductors.

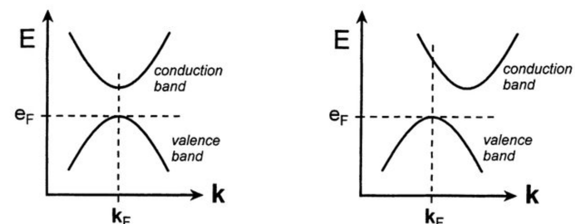

(b) Comparison between direct and indirect bandgap semiconductors.

Figure I.10: Comparison of electronic band structures: (a) Band structures of different materials, (b) Direct and indirect bandgap semiconductors [8].

I.5.3 Optical Properties

Optical properties are a fundamental factor in the study of the interaction of materials with electromagnetic radiation, making them of great importance in many fields, such as solar cells, sensors, and optoelectronics. These properties are analyzed based on density functional theory (DFT) and dielectric function calculations, which show how a material responds to electric fields and their effect on the absorption and reflection of light[53, 54].

Dielectric Function $\varepsilon(\omega)$

The complex dielectric function $\varepsilon(\omega)$ consists of two parts: The real part $\varepsilon_1(\omega)$ expresses the extent of light refraction in the material[55]. The imaginary part $i\varepsilon_2(\omega)$ reflects the amount of light absorption of the material. is calculated using the relationship:

$$\varepsilon(\omega) = \varepsilon_1(\omega) + i\varepsilon_2(\omega) \tag{I.8}$$

The real part of the dielectric function, $i\varepsilon_1(\omega)$ is obtained using the Kramers-Kronig relation:

$$\varepsilon_1(\omega) = 1 + \frac{2}{\pi}\mathcal{P}\int_0^{\infty} \frac{\omega' \varepsilon_2(\omega')}{\omega'^2 - \omega^2} d\omega' \tag{I.9}$$

The imaginary part of the dielectric function,$i\varepsilon_2(\omega)$ is calculated using the following relation:

$$\varepsilon_2(\omega) = \frac{m^2\omega^2}{4\pi e^2} \sum_{c,v} \int |M_{cv}|^2 \delta(E_c - E_v - \hbar\omega)\, d^3k \tag{I.10}$$

Absorption Coefficient $\alpha(\omega)$

The absorption coefficient $\alpha(\omega)$ determines the ability of a material to absorb light at a certain energy[55, 56], and is calculated by the relationship:

$$\alpha(\omega) = \frac{\omega}{c}\sqrt{2}\left[\sqrt{\varepsilon_1^2(\omega) + \varepsilon_2^2(\omega)} - \varepsilon_1(\omega)\right]^{\frac{1}{2}} \tag{I.11}$$

Where: c is the speed of light in vacuum. ω is the angular frequency of the incident radiation.

Reflectivity $R(\omega)$

It expresses the amount of light reflected from the surface of the material, and is calculated as follows:

$$R(\omega) = \left| \frac{\varepsilon(\omega) - 1}{\varepsilon(\omega) + 1} \right|^2 \tag{I.12}$$

The higher the value of (ω), the more the material reflects light, which is important in mirror and reflective coating applications.

Optical Conductivity $\sigma(\omega)$

The optical conductivity $\sigma(\omega)$ represents the material's response to an electromagnetic field, it plays a crucial role in analyzing the behavior of materials in optoelectronic applications, and is calculated using the relation:

$$\sigma(\omega) = \frac{\omega \varepsilon_2(\omega)}{4\pi} \tag{I.13}$$

Studying optical properties helps in designing advanced optical materials for solar cells and photovoltaic materials. Provides clear insight into the transmission of electrons and photons within the material. Helps in identifying suitable materials for reflective coatings, lenses, and laser applications[57, 58].

I.5.4 Thermoelectric Properties

Thermoelectric properties are among the most important physical properties that determine the efficiency of materials in converting thermal energy into electrical energy, which makes them of great importance in modern applications related to energy generation and waste heat utilization. These properties depend on several basic parameters, which are linked together by a relationship that determines the performance of the material in thermoelectric systems[59, 60].

Seebeck Coefficient (S)

The Seebeck coefficient represents the ability to generate an electric voltage when there is a temperature difference across a material. If two ends of a material are placed at different temperatures, electrons or holes within the material will move from the hot end to the cold end, creating an electric voltage.[61] The Seebeck coefficient is defined by the

relationship:

$$S = \frac{\Delta V}{\Delta T} \tag{I.14}$$

Where ΔV is the electrical potential difference and $\Delta T$is the temperature difference. The higher the value of , the more capable the material is of generating electricity from heat, but this property must be accompanied by adequate electrical conductivity to ensure efficient current flow.

Electrical Conductivity σ

Electrical conductivity σ is a physical property that expresses the ability of a material to conduct electric current when an external voltage is applied. Electrical conductivity depends on the density of charge carriers (electrons or holes) and their mobility within the material[61]. Electrical conductivity σ is defined by the relationship:

$$\sigma = nq\mu \tag{I.15}$$

Where:

n : Carrier concentration (cm^{-3})

q : Elementary charge (1.6×10^{-19} C)

μ : Carrier mobility ($cm^2/V.s$)

The electrical conductivity can also be related to the resistivity ρ through the following relation:

$$\sigma = \frac{1}{\rho} \tag{I.16}$$

In metallic materials, electrical conductivity typically decreases with increasing temperature due to enhanced electron-phonon scattering. Conversely, in semiconductors, electrical conductivity tends to increase with temperature as more charge carriers are thermally excited into the conduction band.

Power Factor (PF)

For thermoelectric materials, optimizing electrical conductivity is crucial since it directly influences the power factor[62], defined as:

$$PF = S^2\sigma \tag{I.17}$$

where S is the Seebeck coefficient.

Figure of merit(ZT)

The balance between electrical conductivity and the Seebeck coefficient is essential for achieving high thermoelectric performance[60], as both properties contribute to the dimensionless figure of merit (ZT):

$$ZT = \frac{S^2\sigma T}{\kappa} \tag{I.18}$$

where κ is the thermal conductivity and T is the absolute temperature.

Understanding and controlling electrical conductivity is therefore a key aspect in the design of efficient thermoelectric materials.

Thermal Conductivity (κ)

Thermal conductivity is divided into two main parts:

Electronic thermal conductivity κ_e which results from the movement of electrons and other charge carriers. Lattice thermal conductivity κ_l, which results from the vibrations of the crystal lattice (phonons).

$$\kappa = \kappa_\mathrm{e} + \kappa_\mathrm{l} \tag{I.19}$$

To obtain a highly efficient thermoelectric material, the thermal conductivity must be reduced as much as possible, so that the temperature difference within the material remains for as long as possible, which enhances the Seebeck effect[63].

I.6 Conclusion

In this chapter, we have presented and discussed the most important aspects related to Literature. We have covered the most prominent scientific concepts and foundations

associated with it, with a focus on Half-Heusler (HH) alloys, Point defects in solids, and physical properties (Overview) .

These results and data form an important basis for a deeper understanding of the physical, mechanical, thermoelectrical and optical properties of the system under study. These data will contribute to building an integrated vision in the coming chapters, as they will be linked to the practical and theoretical results with the aim of reaching a comprehensive and accurate analysis.

In the next chapter, we will move to the theoretical framework (DFT), where we will provide a comprehensive overview of the methodology of density functional theory calculations, review the basic principles on which they are based, and focus on how they can be used to study the electronic, energy, and physical properties of the system under study.

Chapter II

Principles and Theoretical Approach

II.1 Introduction

In this chapter, the theoretical framework adopted in this study is presented, with emphasis on density functional theory (DFT), which is one of the most prominent methods used to study the structural and electronic properties of solid materials. The chapter also discusses computational methods for describing and treating point defects in crystalline materials, as an essential part of the study.

Electron interactions in solids are essential for influencing a wide range of physical attributes, including mechanical, optical, and electrical capabilities. In many situations, we may theoretically predict material behavior without the requirement of experimental evidence by examining these interactions and learning how they relate to these attributes[64]. Erwin Schrödinger made a significant contribution to this discipline in 1926 when he developed an equation that described electron mobility and the likelihood that an electron would be discovered in a given area. The electronic structure of a solid can be inferred by solving the Schrödinger equation for its electrons, which is essential for forecasting a variety of characteristics. This equation allows us to examine the distribution and interactions of electrons inside the atomic lattice as well as how these interactions show up as quantifiable characteristics like mechanical strength, electrical conductivity, and light absorption[65].

II.2 The Schrodinger equation

For a solid consisting of N atomic nuclei (cores) and ne electrons, the generalized Schrödinger equation describes the quantum mechanical behavior of all particles in the system. This equation takes into account the positions and interactions of both the electrons and the nuclei[66]. It is written as follows:

$$\hat{H}\Psi(\overrightarrow{R}, \overrightarrow{r}, t) = E\Psi(\overrightarrow{R}, \overrightarrow{r}, t) \tag{II.1}$$

Where $\hat{H}$ is the Hamiltonian of the system given by the following relation:

$$\hat{H} = \hat{T_N} + \hat{T_e} + \hat{U}_{ee} + \hat{U}_{Ne} + \hat{U}_{NN} \tag{II.2}$$

Wheres:

- $\hat{T_N} = -\sum_{I=1}^{N} \frac{\hbar^2}{2M_I}\nabla_I^2$: The kinetic energy of the nuclei.
- $\hat{T_e} = -\sum_{i=1}^{n} \frac{\hbar^2}{2m_e}\nabla_i^2$: The kinetic energy of the electrons.
- $\hat{U}_{ee} = \sum_{i=1}^{n}\sum_{j\succ i}^{n} \frac{e^2}{4\pi\epsilon_0}\frac{1}{|\overrightarrow{r}_i - \overrightarrow{r}_j|}$ The interaction energy between electrons.
- $\hat{U}_{Ne} = \sum_{i=1}^{n}\sum_{I=1}^{N} \frac{e^2}{4\pi\epsilon_0}\frac{Z_I}{|\overrightarrow{r}_i - \overrightarrow{R}_I|}$: The potential energy of the Coulomb attraction between electrons and nuclei
- $\hat{U}_{NN} = \sum_{I=1}^{N}\sum_{J\succ I}^{N} \frac{e^2}{4\pi\epsilon_0}\frac{Z_I Z_j}{|\overrightarrow{R}_I - \overrightarrow{R}_J|}$ The potential energy due to repulsion between nuclei.
- E : The value clean of the Hamiltonian represents the total energy of the system.
- $\Psi(\overrightarrow{R}, \overrightarrow{r}, t)$: Represent the wave function of all coordinates $\overrightarrow{R_I}$ nuclei position $I = 1, \ldots, N$. And N is the position of the electrons $i = 1, \ldots, n$; t is the time) of all nuclei and electrons of the system.

Atomic units are used to simplify the equation. These units are summarized in **Table II.1**, and Equation 2.3 illustrates how to write the Schrödinger equation [67].

$$\left[-\sum_{i=1}^{n}\frac{1}{2}\nabla_i^2 - \sum_{I=1}^{N}\frac{1}{2M_I}\nabla_I^2 + \sum_{i=1}^{n}\sum_{j>i}^{n}\frac{1}{|\overrightarrow{r_i} - \overrightarrow{r_j}|} + \sum_{I=1}^{N}\sum_{J>I}^{N}\frac{Z_I Z_J}{|\overrightarrow{R_I} - \overrightarrow{R_J}|} - \sum_{i=1}^{n}\sum_{I=1}^{N}\frac{Z_I}{|\overrightarrow{r_i} - \overrightarrow{R_I}|}\right]\Psi(\overrightarrow{R}_I, \overrightarrow{r_i}) = E\Psi(\overrightarrow{R}_I, \overrightarrow{r_i}) \tag{II.3}$$

Solving this equation becomes very challenging when dealing with multiple particles. To address this, physicists have developed approximate methods to find solutions.

Table II.1: Atomic units used in DFT and their equivalents in the International System (SI).

Size	**Symbol**	**SI Unit**	**Atomic Units (u.a)**
Electron mass	m_e	$9.1096 \cdot 10^{-31}$ kg	1 u.a
Charge of electron	e	$-1.6022 \cdot 10^{-19}$ C	1 u.a
Reduced Planck constant	$\hbar$	$1.0646 \cdot 10^{-34}$ J·s	1 u.a
Length (Bohr radius)	$a_0 = \frac{4\pi\varepsilon_0\hbar}{m_e e^2}$	$0.52918 \cdot 10^{-10}$ m	1 u.a = 1 Bohr
Energy (Hartree)	$E_0 = \frac{\hbar^2}{m_e a_0^2}$	$4.3598 \cdot 10^{-18}$ J	1 u.a = 1 Hartree

II.3 The Born-Oppenheimer Approximation

The Born-Oppenheimer approximation [68] aims to separate the motion of electrons from that of the nuclei. Given the substantial difference between the mass of an electron and any atomic nucleus, electrons move significantly faster than nuclei. This approximation assumes that electrons remain in their ground state, regardless of the positions of the nuclei. Consequently, the problem simplifies from a system of $N_e + N_n$ interacting particles to an N_e system, where electrons interact within an external potential generated by the nuclei. The positions of the nuclei serve as parameters in solving the problem. The interaction term between the nuclei only factors into the calculation of the system's total energy and not the electronic wave functions. The Hamiltonian, therefore, reduces to include only electronic components and is expressed as follows:

$$\hat{H} = \hat{T}_e + \hat{U}_{ee} + \hat{U}_{Ne} \tag{II.4}$$

We can write a Schrödinger equation on electrons:

$$\hat{H}_e \Psi_e = E_e \Psi_e \tag{II.5}$$

The wave function of system as a product of two wave functions:

$$\Psi \left[\left\{ \overrightarrow{R}_I \right\}, \{ \overrightarrow{r_i} \} \right] = \Psi_e \left[\left\{ \overrightarrow{R}_I \right\}, \{ \overrightarrow{r_i} \} \right] \times \varphi_N \left[\left\{ \overrightarrow{R_I} \right\} \right] \tag{II.6}$$

Since the multi-electron Schrödinger equation is too complex for an analytical solution, additional approximations are employed, such as the Hartree-Fock and Hartree methods, which use a Slater determinant to describe the wave function. Density Functional Theory (DFT) offers an alternative approach by using electron density as the core basis for

describing the system.

II.4 Hartree and Hartree-Fock approximation

In the Hartree approximation [69], it is assumed that each electron moves in a mean-field generated by all other electrons, without considering the direct interaction between the electrons themselves. Basic Equation: The Schrödinger equation is solved for each electron independently in the mean field generated by the other electrons:

$$\hat{H}\Psi_i(\overrightarrow{r_i}) = \varepsilon_i \Psi_i(\overrightarrow{r_i}) \tag{II.7}$$

Where $\Psi_i(r_i)$ represent the electron's wave function can be written as a product of electronic mono waves:

$$\Psi_i(\overrightarrow{r}_1, \overrightarrow{r}_2 ..., \overrightarrow{r}_{Ne}) = \prod_{i}^{Ne} \Psi_i(\overrightarrow{r}_i) \tag{II.8}$$

ε_i is the energy associated with the i-th electron. And H_H is the Hamiltonian of the system given by the following expression:

$$\hat{H}_H = -1/2\nabla_i^2 + U_{ext}(\overrightarrow{r}, \overrightarrow{R}) + U_H(\overrightarrow{r}) \tag{II.9}$$

Where:

- $U_{ext}(\overrightarrow{r}, \overrightarrow{R})$: The potential to the electron-nuclei interactions and those of other electrons, nuclei.
- $U_H(\overrightarrow{r})$: The potential of Hartree associated with Coulomb interaction with other electrons. In Hartree-Fock [70], the wave function is represented by a Slater determinant to ensure antisymmetriy under electron exchange:

$$\Psi_e = \Psi_{DS} = \frac{1}{\sqrt{N!}} \begin{vmatrix} \Psi_1(\overrightarrow{r_1}) & \Psi_2(\overrightarrow{r_1}) & \cdots & \Psi_N(\overrightarrow{r_1}) \\ \Psi_1(\overrightarrow{r_2}) & \Psi_2(\overrightarrow{r_2}) & \cdots & \Psi_N(\overrightarrow{r_2}) \\ \vdots & \vdots & \ddots & \vdots \\ \Psi_1(\overrightarrow{r_N}) & \Psi_2(\overrightarrow{r_N}) & \cdots & \Psi_N(\overrightarrow{r_N}) \end{vmatrix} \tag{II.10}$$

The exchange of two particles is analogous to swapping two columns, which results in a sign change due to a well-known property of determinants. It's important to note that if two rows are identical, the determinant becomes zero, meaning all Ψ_i must be distinct.

This illustrates Pauli's exclusion principle: two (or more) identical fermions cannot occupy the same quantum state. (Ψ_i Composed two parts: orbital function and spatial function, and $1/\sqrt{N!}$ normalization factor). After simplifying the Hamiltonian H_H find:

Where:

- $-\frac{1}{2}\nabla_i^2$: The kinetic energy of the electron i.
- $U_{ext}(\overrightarrow{r}, \overrightarrow{R})$: The energy of attraction between nuclei and electrons.
- $\sum_{\substack{i=1 \\ j\neq i}}^{n} \int \frac{\left|\varphi_i(\overrightarrow{r}')\right|^2}{\left|\overrightarrow{r}-\overrightarrow{r}'\right|}$: The integral of Coulomb noted (the potential of Hartree)
- $\sum_{\substack{i=1 \\ j\neq i}}^{n} \int \frac{\varphi_j(\overrightarrow{r}')\varphi_j^*(\overrightarrow{r}')}{\left|\overrightarrow{r}-\overrightarrow{r}'\right|} d\overrightarrow{r}$: The exchange integral.

II.5 Density Functional Theory (DFT)

All the previous approximations are based on the electronic wave function, making the calculation and solution of the Schrödinger equation quite difficult. One of the most widely used ab-initio methods is Density Functional Theory (DFT) [71], which reformulates the quantum N-body problem into a problem of electronic density alone. Thomas and Fermi (1927, 1928) [72, 73] were the first to propose a theory in this direction, but it proved to be defective in many aspects. Later, Hohenberg, Kohn, and Sham expanded on this idea and developed a more refined theory that better accounts for kinetic energy as well as exchange and correlation energies.

II.6 Thomas-Fermi model

The Thomas–Fermi (TF) model[72, 73], named after Llewellyn Thomas and Enrico Fermi, is a quantum mechanical framework for describing the electronic structure of many-body systems. Developed semiclassically shortly after the Schrödinger equation was introduced [66], it differs from wave function theory by focusing exclusively on electronic density, making it a foundational step toward modern Density Functional Theory (DFT). The TF model is strictly accurate only under the condition of an infinite nuclear charge. When applied to real-world systems, it often produces poor quantitative results, unable to capture key density characteristics like atomic shell structures and Friedel oscillations in solids. Despite these limitations, the TF model has gained applications across various fields,

thanks to its ability to reveal qualitative trends analytically and its computational simplicity. Furthermore, the TF kinetic energy expression is incorporated into more advanced density approximations for kinetic energy in modern orbital-free DFT methods.

In 1927, working independently, Thomas and Fermi developed a statistical model to approximate the distribution of electrons within an atom. While electron distribution in an atom is inherently nonuniform, they approximated that electrons are uniformly distributed within each small volume element ΔV (i.e., locally), allowing the electron density $n(\overrightarrow{r})$ to vary from one volume element to another.

$$E_0 = [n] \tag{II.11}$$

$$T_{TF} = [n] \int t[(\overrightarrow{r})]dr \tag{II.12}$$

$$t[n(\overrightarrow{r})] = \frac{3}{5} n(\overrightarrow{r}) E_F \tag{II.13}$$

$$E\left[\Psi\right] = E\left[n\right] = T\left[n\right] + U_{ee}\left[n\right] + \int U_{ext}(\overrightarrow{r}) n(\overrightarrow{r}) dr \tag{II.14}$$

$t[n(\overrightarrow{r})]$ represent the kinetic energy density of an electron system without interaction. If the electronic density of a system is whatever is given, this functional allows to calculate explicitly the total energy, from which we obtain the minimization of the functional over all possible densities.

II.7 Hohenberg-Kohn theorems

- **First Theorem:** "For any system of interacting particles in an external potential $U_{ext}\overrightarrow{r}$, the density uniquely determines the system"—that is, the external potential is a unique functional of the density proven by reductio ad absurdum, showing that a contradiction would arise otherwise [74].

- **Second Theorem:** The energy reaches its minimum at the true ground-state density, meaning that the electronic density of the system in its ground state corresponds to the lowest possible total energy [74].

$$E[n_0(t)] \leq E[n(t)] \tag{II.15}$$

Kohn-Sham Equation

Kohn and Sham proposed replacing interacting multi-particle systems with a simpler system of non-interacting particles, which is easier to solve [75]. Their approach assumes that the electron density in the ground state of the real system is identical to that of a fictitious system of non-interacting particles. This leads to solving a set of equations for independent particles, similar to those in the Hartree or Hartree-Fock methods.

$$\hat{H}_{KS} = \varphi_i(\overrightarrow{r}) = \varepsilon_i \varphi_i(\overrightarrow{r}) \tag{II.16}$$

With:

$$\hat{H}_{KS} = -\frac{1}{2}\nabla_i^2 + U_{eff}(\overrightarrow{r}) \tag{II.17}$$

And:

$$U_{eff} = U_{ext}(\overrightarrow{r}) + \int \frac{n(\overrightarrow{r})}{|\overrightarrow{r} - \overrightarrow{r}'|} dr' + U_{xc}(\overrightarrow{r}) \tag{II.18}$$

The challenge lies in the inability to precisely define the exchange and correlation terms in their exact form. Therefore, approximations must be made to handle these terms.

II.8 Exchange-Correlation Approximation

Local Density Approximation (LDA)

The Local Density Approximation (LDA) [74, 75] assumes that the density at a point $\overrightarrow{r}$ depends solely on the density at that point. It is approximated as being equal to the correlation energy per particle of a homogeneous gas with density $n(\overrightarrow{r}$:

$$E_{xc}^{LDA}[n(\overrightarrow{r})] = \int n(\overrightarrow{r}) \varepsilon_{xc}^{LDA}(n(\overrightarrow{r}))dr \tag{II.19}$$

The exchange-correlation energy can be decomposed into the sum of the exchange energy and the correlation energy.

$$\varepsilon_{xc}^{LDA}[n(\overrightarrow{r})] = \varepsilon_x[n(\overrightarrow{r})] + \varepsilon_c[n(\overrightarrow{r})] \tag{II.20}$$

The exchange energy term is known and is given by the Thomas-Fermi-Dirac exchange functional:

$$\varepsilon_x^{LDA}[n(\overrightarrow{r})] = -\frac{3}{4}(\frac{3}{\pi})^{\frac{1}{3}}n(\overrightarrow{r})^{\frac{1}{3}} \tag{II.21}$$

The correlation part cannot be expressed exactly. The approximation of this term, established by Vosko, Wilk, and Nussair (VWN) [76], has been highly successful. It is based on an interpolation of very precise quantum Monte Carlo calculations on the uniform electron gas, performed by Ceperly and Alder. The effectiveness of this approximation became evident in the 1970s through the works of Zunger and Freeman, as well as Moruzzi et al. Today, there are excellent references on the subject, including works by Lundqvist and March, Callaway and March, Dreizler and Provincia, and Parr and Yang. In particular, the LDA approximation is best suited for strongly bound periodic systems [77].

Generalized Gradient Approximation (GGA)

The LDA approach is based on the homogeneous electron gas model, which assumes a uniform electron density. However, atomic or molecular systems are typically quite different from a homogeneous electron gas. More generally, we can consider that real systems are inhomogeneous, meaning that the electronic density varies spatially. Many of the corrections introduced to the LDA are based on the idea of accounting for these local variations in density. For this reason, the gradient of the electronic density has been introduced, leading to the Generalized Gradient Approximation (GGA) [78], where the exchange energy and correlation depend on both the electron density and its gradient. In this approximation, the exchange energy and correlation are functions of the electron density and its gradient:

$$E_{xc}^{GGA}[n(\overrightarrow{r}), \nabla n(\overrightarrow{r})] = \int n(\overrightarrow{r})\varepsilon_{xc}^{GGA}[n(\overrightarrow{r}), \nabla n(\overrightarrow{r})]dr \tag{II.22}$$

Density Functional Theory with Hubbard Correction (DFT+U)

Strongly correlated systems are composed of structures that include transition metals or rare earth ions. The phenomenon of electron correlation arises due to the partially filled d or f orbitals. Traditional approaches like LDA and GGA fail to accurately describe these systems. To address this limitation, Dudarev et al. proposed a correction within the framework of DFT, known as DFT+U (or LDA+U, GGA+U) [79]. In this method, U

represents the effective intrasite Coulomb repulsion between localized electrons (Hubbard term). The core idea of this approximation is to add an additional term, U, to the LDA or GGA potential for each d and f orbitals. This adjustment helps achieve a more accurate representation of the electronic gap and magnetic properties of magnetic materials. The DFT+U method modifies the standard DFT functional by introducing an energy correction, expressed as:

$$E^{DFT+U} = E^{DFT} + E^{Hub} - E^{dc} \tag{II.23}$$

Where:

- E^{DFT}: represents the energy contribution from the standard DFT (LDA or GGA).
- E^{Hub} : is a correction to the electron-electron interaction energy.
- E^{dc}: is a double-counting term that removes contributions included in both E^{DFT} and E^{Hub}.

The evaluation of energy using this formula requires explicit expressions for E^{Hub} and E^{dc}. Numerous formulations for these terms have been proposed in the literature:

$$E_{DFT+U} = E_{DFT} + \frac{(U-J)}{2} \sum_{m,s} (n_{l,m,} - n^2_{l,m,s}) \tag{II.24}$$

where m and s stand for the magnetic quantum number and spin, respectively, and l is the angular momentum on an electron with orbital occupation n. The energy penalty can be added using the Dudarev approach by using a single $U - J$ factor; the penalty can be administered as a purely coulombic interaction if J is taken to be zero. The applied U value, which yields the system-dependent variation accuracy of correction, is usually obtained by fitting DFT+U results to empirical data. DFT+U has the advantage of being a straightforward correction that doesn't significantly increase the computational cost of the LDA or GGA functionals that it is commonly employed with[79].

Meta-Generalized Gardient Approximation (Meta-GGA)

In the context of increasing accuracy and efficiency in quantum computing, meta-GGA is one of the approximations that have been developed to do this, as it is an extension of the

GGA where the kinetic energy density has been inserted into the correlation and exchange expression [**eq:II.25**]. This allows meta-GGAs to address different chemical bonds (e.g., covalent, metallic, weak) more accurately compared to LDAs and GGAs[80, 81].

$$E_{xc}^{mGGA} = \int d^3 r n \varepsilon_{xc}^{mGGA}(n\uparrow, n\downarrow, \nabla n\uparrow, \nabla n\downarrow, \nabla^2 n\uparrow, \nabla^2 n\downarrow, \tau\uparrow, \tau\downarrow) \tag{II.25}$$

Where $\tau_\sigma(r) = \sum_i \frac{1}{2}|\nabla\varphi_{\sigma i}(r)|^2$ is the Kohn-Sham orbital kinetic energy density for electrons with spin σ. And $\nabla\varphi_{\sigma i}(r)$ they are single-particle Kohen-Sham wave functions. Common meta-GGA functions include mBj[82], LMBJ[83], TPSS[81], M06-L[84], revTPSS[85], R2SCAN[86], and SCAN[87]...

Hybrid Functional: Heyd-Scuseria-Ernzerhof (HSE)

The use of the LDA or GGA under the DFT allows a surprisingly accurate description of most of the properties of solids and molecules. However, using these two approximations still generates some large errors, especially when calculating the fundamental energy of small molecules and the gap-extended systems. In order to compensate for these shortcomings, a new generation of functionalities has been recently developed. In these models, the correlation and exchange energy functional makes both Hartree-Fock and other formalisms of the DFT (LDA or GGA), hence their name of functional hybrid. Currently, the most common hybrid functionals are PBE0, HSE03, HSE06, and B3LYP [78, 88–90]. The use of such functionalities makes it possible to get closer to the data known experimentally, such as lattice parameters or the energy gap in some systems. In general, hybrid functionalities are particularly effective for describing molecules and insulating materials, semiconductors, and transition metal oxides. Their main drawback of these calculations is that they are generally more greedy in computing resources than for conventional functionals because of the incorporation of the terms Hartree-Fock[89].

II.9 Calculation Methods

Pseudopotential method

The pseudopotential approach is based on the assumption that most properties of physical systems and electronic systems depend more on valence electrons than on core electrons.

The bonding of atoms is mainly due to the valence electrons, while the core electrons can be considered stabilized, so they can be ignored in most cases. Practically, pseudo-

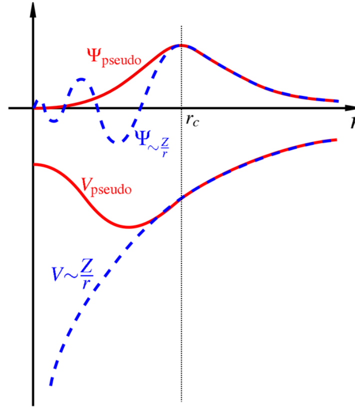

Figure II.1: Schematic of a pseudo wave function and pseudopotentials.

potentials are constructed so that beyond a certain ray of Cut-off r_c, defining a sphere inside which the electrons are ocated of the core, the pseudo-potential and the valence wave pseudo-functions must be identical true potential and true valence wave functions [91–93].

Plane Waves

Plane waves are exactly the proper functions of a homogeneous electron gas system [94]. This is the natural choice of the base in the case of simple metals. Waves planes are orthonormal and independent of energy, so the Schrödinger equation transforms into a simple eigenvalue matrix problem, and since plane waves do not depend on the atomic positions, we can apply the Hellman-Feynman directly to calculate the forces acting on the atoms. On the other hand, convergence is simple since increasing the number of waves increases accuracy [75]. The choice of number of plane waves to use is truncated by a so-called cutoff energy E_{cut} such as:

$$\frac{1}{2}\left|K+G\right|^2 \leq E_{cut} \tag{II.26}$$

II.10 Technical Calculation

Periodic Systems and Bloch theorem

The Bloch theorem is a consequence of the periodicity of the crystalline potential; it illustrates the invariance of the system by translational symmetry. The wave function is then written as the product of a periodic function, U_j^k clean lattice, and a plane wave, which translates the lattice translation[95].

$$\Psi_j^k(\overrightarrow{r}) = U_j^k(\overrightarrow{r}) \exp i(\overrightarrow{k}.\overrightarrow{r}) \tag{II.27}$$

$$U_j^k(\overrightarrow{r}) = \sum_G \widetilde{u}(\overrightarrow{G}) \exp i(\overrightarrow{G}.\overrightarrow{r}) \tag{II.28}$$

The vectors $\overrightarrow{k}$ and $\overrightarrow{G}$ are defined in reciprocal space within the first Zone Brillouin (ZB). The wave vector $\overrightarrow{k}$ is a quantum number own orbital bloch. The solving of Kohn and Sham equations within a periodic system is done necessarily for a finite number of points K obtained by representative sampling and suitable of the ZB that allows to reproduce faithfully its symmetry[4, 48, 96].

Sampling of The Brillouin Zone

Brillouin-zone sampling in total-energy calculations of aperiodic systems using periodic boundary conditions is considered. Although the energies converge to the exact result in the limit of large supercells for any k-point sampling scheme, they do not converge at the same rate. In particular, it has been shown that the use of a single sampling point at the origin of reciprocal space is especially inefficient. A k-point sampling scheme is proposed, which is computationally efficient and its efficacy relative to other common approaches is demonstrated[4, 48, 97].

II.11 Calculation Codes and Analyses Tools

VASP Code

The Vienna Ab initio Simulation Package (VASP)[98] is a software package for performing DFT-based calculations to describe the interactions between ions and electrons using a plane-wave (PW) basis

set[99], the pseudopotentials approach (PP), or the projector augmented wave method (PAW)[98, 100].

VASP gives an approximate solution to the multibody Schrödinger equation within the density functional theory to solve the Kohn-Sham equation or through the Hartery-Fock approximation; it can also implement hybrid functions such as HSE06, and in addition, Green's functions (quasi-particle GW, ACFDT-RPA) and multibody perturbation theory (second-order Møller-Plesset) are available in VASP [99].

PHONOPY Code

Phonopy is a free [101], open-source program that uses the direct force-constant method to calculate phonons using harmonic and quasi-harmonic approximations[102]. The quasi-harmonic approximation can be used to obtain properties at constant pressure, such as izobaric heat capacity and thermal expansion coefficients, while the harmonic level enables the calculation of phonon band structure, phonon DOS and partial-DOS, and phonon thermal properties, such as free energy, izochoric heat capacity, entropy, and other properties at constant volume[103–105].

SITE OCCUPATION DISORDER (SOD)

SOD (short for Site-Occupation Disorder)[106, 107] is a set of tools for computational modeling of periodic systems with site disorder using the supercell ensemble method. The non-periodic occupation of lattice sites in a crystal structure is known as site-occupation disorder, and is common in solid-state chemistry and physics. Such as metal alloys, non-stoichiometric synthetic compounds, and metal solid solutions. Site-occupation disorder is a good tool for generating all possible configurations, and based on the symmetry of the crystal structure, the harmonic and recurring configurations are reduced to facilitate and speed up simulations[107, 108].

BOLTZTRAP2 Code

Boltzmann Transport Properties (BoltzTraP)[109, 110] is software for computing the semi-classic transport parameters. The code uses a mesh of band energies and is interfaced to the WIEN2k, ABINIT, SIESTA, VASP, and QuantumEspresso programs[111]. BoltzTraP2 is a new version implementation of the smoothed Fourier interpolation algorithm

for electronic bands that formed the base of the original and widely used BoltzTraP code[110]. One of the most typical uses of BoltzTraP is the calculation of thermoelectric transport parameters as functions of temperature and chemical potential in the rigid-band picture. (e.g Seebeck coefficient , electrical conductivity,...)[110–112].

VASPKIT

The purpose of VASPKIT is to provide a stable and intuitive interface for high-throughput material property analysis using raw data produced by the popular VASP algorithm. For ease of use, the application offers both command-line mode and an interactive user interface. Both a free (VASPKIT) and a more polished premium version are available (VASPKIT Pro)[113].

II.12 Ab-intio Point Defects Calculation

The theoretical study of the physical properties of compounds using density functional theory in the case of ideal crystals is based mainly on the study of the primitive cell in order to predict its properties due to the infinite repetition of the primitive cell and the symmetry present within the crystals, but in the case of the presence of point defects, this leads to breaking the symmetry, which makes the use of the small primitive cell to predict the properties impossible, so it is necessary to use the supercell approach, which is the most common method that is relied upon in this thesis. The concentration of defects in the supercell is very low, so the interactions between defects are neglected, and the use of small supercells makes the concentration of defects very high, and the effects between defects cannot be neglected[114]. Therefore, it is better to use large supercells, but this matter depends on the efficiency of the devices in implementing heavy calculations, as they usually consume much longer time compared to normal calculations in the case of primitive cells. In our study of point defects, supercells of 2×2×1 dimensions containing 48 atoms were used. The supercell method is illustrated in figureII.2. This method is based on generating an ideal mesh by periodically repeating the unit cell of the host material.

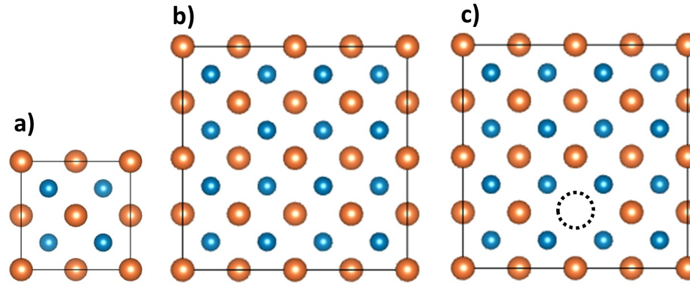

Figure II.2: Schematic of : a) Unit cell, b) Pristine (perfect) 222 supercell, c) Defective supercell.

Formation Energy of Defects in Solids

Formation energy is a fundamental measure used in the study of the stability of defects in crystal lattices of solids. Defects, such as vacancies, substitutions, or atomic insertions, represent disturbances in the ideal crystal structure and have a significant effect on the physical and chemical properties of the material. Formation energy is defined as the energy required to create a specific defect within the material, and is calculated using equations based on the total energy of the system before and after defect formation.

Formation energy for neutral defects can be expressed using the following equation:

$$E_{\mathrm{f}} = E_{tot}[X] - E_{tot}[bulk] + \sum_{i} n_i \mu_i \tag{II.29}$$

where: E_{f} formation energy of the neutral defect, $E_{tot}[X]$ total energy of the system containing the defect. $E_{tot}[bulk]$ total energy of the pristine system, n_i number of atoms of type i added ($n_i > 0$) or removed ($n_i < 0$), and μ_i represents the chemical potential of an atom i in a theoretical external reservoir. In the context of ideal semiconductor crystals, this potential expresses the reference energy that relates to the species that are added or removed when a defect is created. This potential is used to define the changes in energy resulting from modification of the atomic structure of the material during defect formation[115, 116].

The formation energy provides insights into the likelihood of defect formation, with lower values indicating a higher probability of spontaneous defect generation. While defects with high formation energy are less common and require additional energy to form.

In the case of charged defects, the formation energy E_f becomes more complicated, as it also depends on the chemical potential of the electrons mu_e, reflects the position of

the Fermi level E_F , within the energy gap, and this effect is included in the expression for the formation energy as follows:

$$E^f[X^q] = E_{tot}[X^q] - E_{tot}[bulk] - \sum_i n_i\mu_i + q\left(E_{VBM} + \mu_e\right) + E_{corr} \tag{II.30}$$

Where $E_{tot}[X^q]$ represent the total energy of the defect state with charge q and E_{VBM} is the valence band maximum for the bulk material of study, the parameter e can then be treated as a free parameter, allowing the Fermi level shift to be interpreted. In the case of intrinsic semiconductors without doping located in the middle of the band gap $\mu_e = E_{gap}/2$. E_{corr} correction terms are included in the formation energy to adjust for the effect of electrostatic interactions between periodic images of defects resulting from the use of periodic boundary conditions in the calculations. This correction is to address the interactions resulting from the long-range nature of Coulomb forces, which are of great importance when studying systems of finite size. Therefore, corrections are applied to account for the effect of these interactions without having to increase the system size significantly[117, 118].

Chemical Potentials

Chemical potentials change based on temperature and pressure during the manufacture of the material. These conditions indirectly determine the stability of the different phases of the material, which affects the chemical potential of each element in it. There is no standard or general method for determining the chemical potentials for all cases. Instead, theoretical models and calculations are relied upon, taking into account the ambient conditions of the system. In systems containing impurities or defects, the effects of these impurities interfere with the chemical potential, making the determination more complex[119]. The chemical potentials are expressed in terms of thermodynamic quantities as:

$$\mu_i = \left(\frac{\partial G}{\partial n_i}\right)_{T,P} = \left(\frac{\partial H}{\partial n_i}\right)_{P,S} = \left(\frac{\partial F}{\partial n_i}\right)_{V,T} = \left(\frac{\partial U}{\partial n_i}\right)_{V,S} \tag{II.31}$$

However, fixed limits can be set for chemical potentials, providing a clear framework for analyzing the stability of matter and understanding chemical reactions. These limits are a very useful tool in interpreting results. In general, μ_i refers to the total energy E_i of pure solid or molecular elements.

The range of chemical potential μ_i of the elements of matter is determined based on the stability of the phases and the absence of formation of secondary phases or compounds. In multicomponent systems, the range depends on the thermodynamic conditions that maintain the stability of the matter. The following are the basic steps for determining this range: - The chemical potentials of the elements in the compound must satisfy the relationship:

$$\sum_i n_i \mu_i = \Delta H_f \tag{II.32}$$

where ΔH_f Enthalpy of formation of a compound. This relationship defines the range of chemical potential based on the energy required to form the substance from its constituent elements.

- The chemical potential of any element must not exceed the total energy of its bulk state.

$$\mu_i \leq \mu_i^{\text{bulk}} \tag{II.33}$$

- The minimum depends on the stability of the substance and is determined to prevent the formation of secondary compounds or phases

II.13 Conclusion

Finally, this chapter provides a theoretical and methodological basis necessary for understanding the scientific framework on which this study is based. By reviewing the theory of density functions and its physical foundations, in addition to the methods adopted in characterizing point defects, the foundations were laid that will be built upon in the following chapters to analyze the structural and electronic properties of the studied systems, linking them to the effects resulting from the presence of defects.

Chapter III

Results and Discussion

III.1 18-Electrons ABX Half-Heusler Alloys Properties

III.1.1 Introduction

As mentioned earlier, Half-Heusler compounds are among the most important crystalline materials that have promising applications in electronics, spintronics, and thermoelectric materials[3, 33]. These compounds follow the general formula ABX, where A and B represent two metallic elements, while X is a non-metallic or semiconductor element. These compounds are characterized by a crystal structure of the type $C1_b$, which follows the face-centered cubic (FCC) crystal system. TiIrSb, ZrIrSb, TaIrGe, and TaIrSn, these compounds are considered part of the 18-electron Half-Heusler compounds family, which are characterized by their electronic and structural stability. Their physical properties vary according to their atomic composition, which makes them of multiple applications, so in this chapter using first principals we will provide a comprehensive study on the properties of the compounds in their ideal state[9].

III.1.2 Computational Details

The physical properties of the ABX half-Heusler compounds were investigated within density functional theory (DFT), as implemented in the VASP package.[16, 96, 99?] The electronic exchange–correlation effects were treated using the generalized-gradient PBE functional[78] and the meta-GGA SCAN functional,[87, 120] while the screened

hybrid HSE06 functional[89] was employed for selected electronic-structure calculations in order to obtain more accurate band-gap values. The projector augmented-wave (PAW) method[95, 99] was used to describe the interaction between valence electrons and ionic cores.

A plane-wave cutoff energy (`ENCUT`) of 600 eV was adopted to ensure well-converged total energies. Brillouin-zone integrations were carried out using Monkhorst–Pack **k**-point meshes,[97] generated via a `KSPACING` value of 0.030, which corresponds to 11×11×11 and 17×17×17 grids for structural relaxations and density-of-states (DOS) calculations, respectively. The electronic self-consistency criterion (`EDIFF`) was set to 1×10^{-7} eV, and the force-convergence threshold (`EDIFFG`) was fixed at -0.01 eV/Å. After full geometry optimization to reach the equilibrium structure, the electronic band structure, DOS, and optical properties were computed; on top of the converged PBE/SCAN geometries, additional band-structure and DOS calculations were performed using HSE06 for a refined description of the band gaps.

The thermoelectric transport coefficients were subsequently evaluated with the BoltzTraP2 code,[111, 112] which interpolates the DFT band structures and solves the semiclassical Boltzmann transport equation within the constant-relaxation-time approximation. The valence electronic configurations of the constituent atoms were taken from the IUPAC periodic table[121] and read as follows: Ti: [Ar] $3d^2 4s^2$, Zr: [Kr] $4d^2 5s^2$, Ta: [Xe] $4f^{14} 5d^3 6s^2$, Ir: [Xe] $4f^{14} 5d^7 6s^2$, Sb: [Kr] $4d^{10} 5s^2 5p^3$, Ge: [Ar] $3d^{10} 4s^2 4p^2$, and Sn: [Kr] $4d^{10} 5s^2 5p^2$.

III.1.3 Structural Properties

ABX crystallizes in the half-Heusler structure, which follows the space group $F\overline{4}3m(No.216)$ with a total number of 18 valence electrons per unit cell. This structure consists LiAlSi-type of a face-centered cubic (FCC) lattice where atoms occupy three distinct positions in the crystal lattice. Element A is localized at 4a(0,0,0), element B occupies the 4c($\frac{1}{2}$, $\frac{1}{2}$, $\frac{1}{2}$) position, and element X occupies the 4b($\frac{1}{4}$, $\frac{1}{4}$, $\frac{1}{4}$) position. This structure is similar to the Full-Heusler structure but contains partial vaccums in the crystal lattice, making it more flexible to accommodate the effects of defects. Figure I.1 shows the structural structure of the ABX systems[122].

The lattice parameter a is one of the most important crystalline properties that determines the arrangement of atoms within the crystal lattice and directly affects the elec-

tronic, mechanical, and thermal properties of compounds. In our study, the calculated values The lattice parameter a was obtained by relaxing the initial unit cell of each compound within density functional theory (DFT), where: The initial structures were taken from the OQMD database, which provides accurate crystal structures based on previous experimental or computational data. Relaxation of the initial cells was performed to ensure reaching the lowest total energy, which reflects the most stable structure for each compound.

The calculations were performed using the PBE and SCAN approximations. Table III.1 shows the calculated values of the lattice parameter a obtained with these two functionals, together with data from previous studies for comparison. Our results display a very good agreement with the reference values, as the deviations between the calculated and literature data do not exceed 0.02–0.03 Å, which reflects the accuracy of our simulations and the effectiveness of DFT in describing the crystal structure of these compounds. The SCAN approximation provides lattice parameters closer to the experimental values than PBE, as expected, since SCAN usually offers a more accurate description of chemical bonding.

The slight increase in the lattice parameter a observed when moving from Ti to Zr can be ascribed to the larger atomic radius of Zr compared to Ti. This increase in atomic size results in longer interatomic distances, thereby leading to a slight expansion of the crystal lattice. Conversely, the TaIrGe and TaIrSn compounds exhibit relatively smaller lattice parameters. This behavior can be attributed to the nature and strength of the covalent bonds formed between Ta–Ir and Ge/Sn atoms. The enhanced covalent interactions effectively constrain the lattice expansion, resulting in more compact crystal structures

III.1.4 Electronic Properties

At this stage, we discuss the results of the electronic property calculations. Table III.2 summarizes the band-gap (E_g) values of the studied compounds obtained using the PBE, SCAN, and HSE06 exchange–correlation functionals. As expected, SCAN systematically yields larger gaps than PBE, reflecting the well-known underestimation of E_g by semi-local GGAs, while HSE06 further enlarges the gap and provides values that are much closer to the available experimental and hybrid-functional data in the literature. The improved description of exchange and correlation in SCAN and, in particular, the inclusion of a

Table III.1: Structural parameters and elastic constants for ABX compounds calculated using PBE (SCAN), with comparison to previous works. Experimental data from [9, 10]; GGA-PBE calculations [11, 12]; GGA-PBEsol [13]; PBE+U and SCAN [14].

Property	**TiIrSb**	**ZrIrSb**	**TaIrGe**	**TaIrSn**
a (Å)	6.142 (6.164)	6.359 (6.367)	6.013 (5.921)	6.219 (6.131)
Other	6.169[9], (6.191; 6.122)[14]	6.372[9], (6.374; 6.306)[14]	6.026[9], 5.966[10]	6.251[123], 6.233[9]
C_{11} (GPa)	235.50 (257.31)	238.658 (290.492)	279.55 (298.72)	278.99 (295.68)
Other	234.14[14], 255.52[11]	243.17[14]	229.17[11]	244.20[123]
C_{12} (GPa)	121.86 (115.19)	106.867 (116.906)	163.94 (153.45)	139.78 (132.10)
Other	114.47[14], 120.42[11]	105.41[14]	156.01[11]	146.30[123]
C_{44} (GPa)	67.64 (81.27)	72.766 (86.945)	96.09 (106.39)	80.35 (84.29)
Other	64.29[14], 86.87[11]	71.55[14]	119.62[11]	101.89[123]
B (GPa)	159.741 (162.564)	150.797 (174.768)	202.479 (201.877)	186.182 (186.628)
Other	142.82[14], 169.47[14], 173.22[123]	167.47[13]	196.88[11]	175.50[123]
G (GPa)	67.64 (81.27)	72.766 (86.945)	96.10 (106.40)	80.35 (84.27)
Other	69.031[124]	78.28[11]	91.47[11]	75.91[123]
B/G	2.53 (2.11)	2.16 (2.01)	2.58 (2.21)	2.45 (2.24)
Other	2.47[14], 2.17[12]	2.03[11]	2.57[11]	2.35[123]
E (GPa)	177.82 (162.56)	188.049 (223.734)	248.99 (201.87)	210.73 (219.73)
Other	166.52[12]	201.69[11]	238.60[11]	199.45[123]

fraction of exact exchange in HSE06 lead to a more realistic representation of the electronic structure. In all levels of theory, Zr-containing compounds such as ZrIrSb exhibit wider gaps than the Ta-based systems, underlining the crucial role of the heavy cation in setting the separation between the valence and conduction bands.

The analysis of the band structures reveals that the fundamental gap in TiIrSb and ZrIrSb occurs between the Γ and X points, whereas TaIrGe and TaIrSn display a gap located along the L–X direction (Figure III.1). This difference reflects variations in the distribution of the electronic states near the Fermi level, driven by changes in crystal symmetry and orbital hybridization among the constituent atoms. The position of the gap in the Brillouin zone is particularly relevant for charge-transport and optical processes: a gap involving Γ is favourable for direct optical transitions, while an L–X gap is intrinsically indirect and may reduce the optical absorption strength even though it still supports efficient charge-carrier transport, which is relevant for thermoelectric applications.

Substituting Ti by Zr leads to an increase in the band gap, which can be attributed to differences in atomic radii and in the strength of the hybridization between the group-IV/group-V elements and the Ir d orbitals. The heavier Zr cation modifies the effective energy levels of the d states and shifts the conduction-band edge upward, thereby widening the gap. In contrast, the Ta-containing compounds exhibit smaller band gaps than their Ti- and Zr-based counterparts, a trend that can be ascribed to the stronger delocalization of Ta $5d$ states, which enhances the overlap with Ir d orbitals and narrows the energy separation

between the valence and conduction bands.

The analysis of the total and partial density of states (TDOS and PDOS) (Figure III.2) confirms that the d orbitals of the transition metals Ti, Zr, Ta, and Ir dominate the states around the Fermi level and thus control the formation of the band gap in all compounds. In contrast, the p and d orbitals of Sb, Sn, and Ge contribute only weakly in this region, indicating that the electronic interactions are mainly governed by the hybridization between transition-metal d orbitals and the p orbitals of the main-group elements. For TiIrSb and ZrIrSb, a pronounced overlap between Ti/Zr d and Ir d states along the Γ–X path leads to the opening of an indirect band gap, whose width is determined by the strength of this d–d coupling and is larger in ZrIrSb than in TiIrSb.

In TaIrGe and TaIrSn, the Ta d orbitals interact strongly with the Ir d states, giving rise to a gap along the L–X direction. The slightly larger gap in TaIrSn compared to TaIrGe can be linked to subtle differences in Ta–Ir d–d hybridization and to the chemical environment created by Sn versus Ge. Although the p orbitals of Sb, Sn, and Ge are visible in the DOS, their role in defining the fundamental band gap is secondary; for instance, in TaIrSn the Sn p states participate in the hybridization but the gap remains primarily controlled by the transition-metal d manifold.

Table III.2: Band-gap values E_g (eV) of the ABX half-Heusler compounds: this work (PBE, SCAN, HSE06) and selected literature data.

Compound	**E_g(eV) (this work)**			**Gap type**	**E_g(eV) (Other)**
	PBE	**SCAN**	**HSE06**		
TiIrSb	0.825	1.043	1.680	Γ-X	1.63 (HSE06)[9], 1.70 (HSE06)[125]
ZrIrSb	1.449	1.768	2.101	Γ-X	1.416 (PBE)[14], 1.91 (HSE06)[9], 2.06 (HSE06)[125]
TaIrGe	0.994	1.246	1.610	L-X	1.62 (GGA+U), 1.84 (HSE06)[11]
TaIrSn	0.990	1.257	1.583	L-X	1.55[9], 1.54 (GGA+U), 1.75 (HSE06)[11]

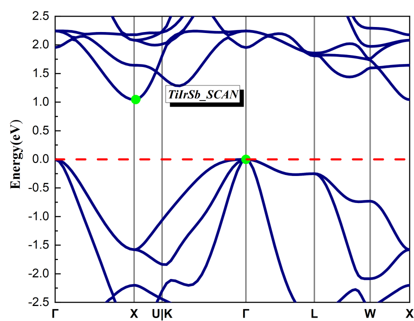

(a) SCAN - TiIrSb

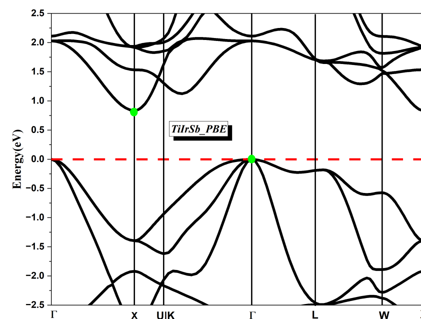

(b) PBE - TiIrSb

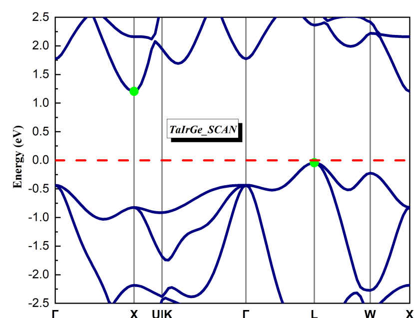

(c) SCAN - TaIrGe

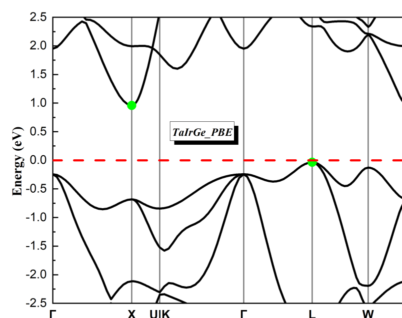

(d) PBE - TaIrGe

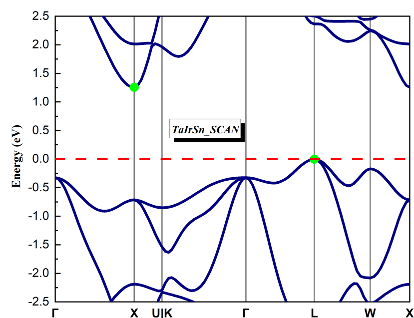

(e) SCAN - TaIrSn

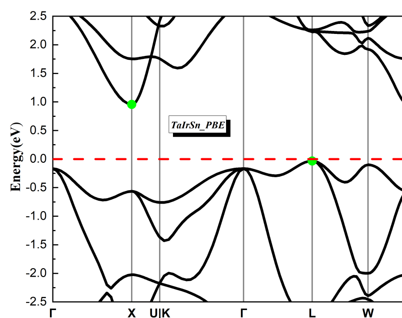

(f) PBE - TaIrSn

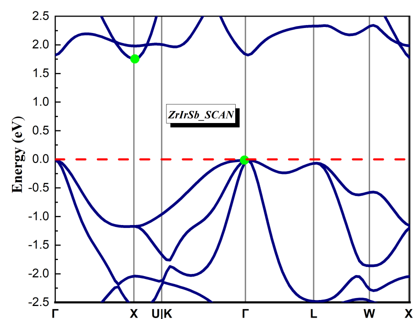

(g) SCAN - ZrIrSb

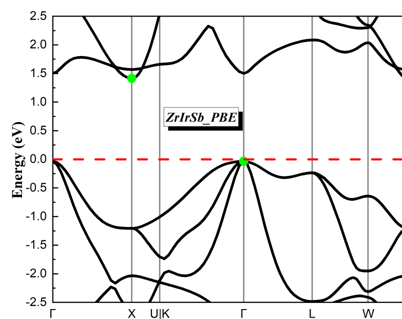

(h) PBE - ZrIrSb

Figure III.1: Band structure plots calculated using SCAN and PBE for the ABX (HH) compounds.

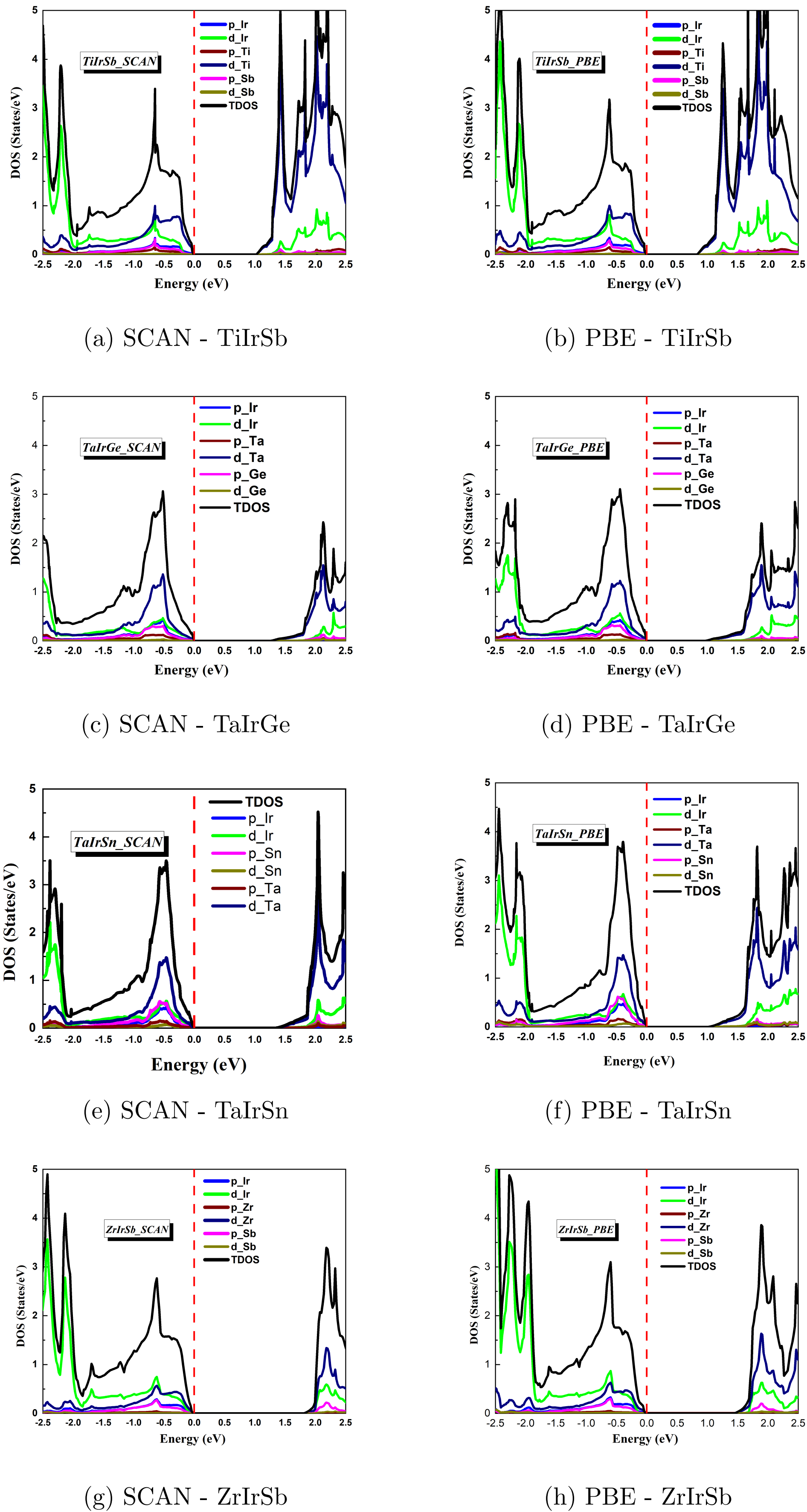

(a) SCAN - TiIrSb

(b) PBE - TiIrSb

(c) SCAN - TaIrGe

(d) PBE - TaIrGe

(e) SCAN - TaIrSn

(f) PBE - TaIrSn

(g) SCAN - ZrIrSb

(h) PBE - ZrIrSb

Figure III.2: Total (TDOS) and Partial (PDOS) density of states plots calculated using SCAN and PBE for the studied compounds.

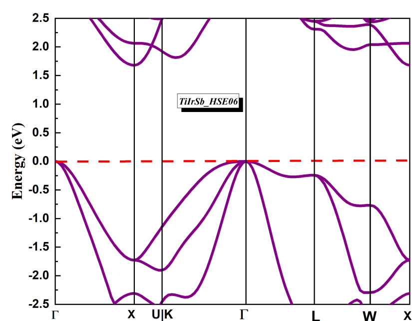

(a) HSE06 - TiIrSb

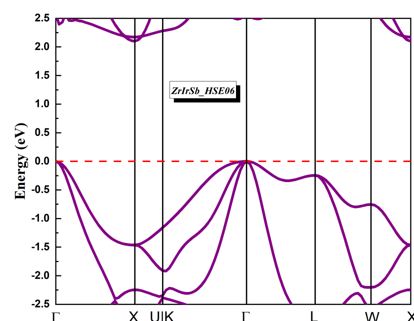

(b) HSE06 - ZrIrSb

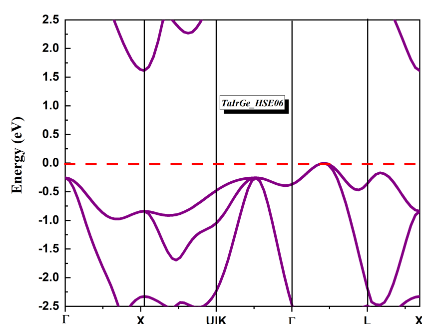

(c) HSE06 - TaIrGe

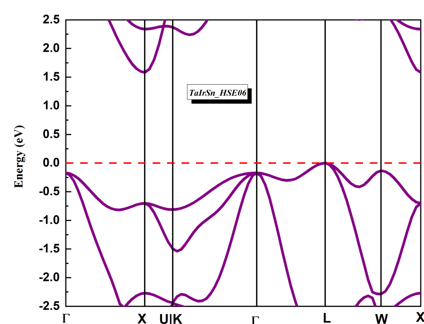

(d) HSE06 - TaIrSn

Figure III.3: Band structure plots calculated using the HSE06 hybrid functional for the ABX (HH) compounds.

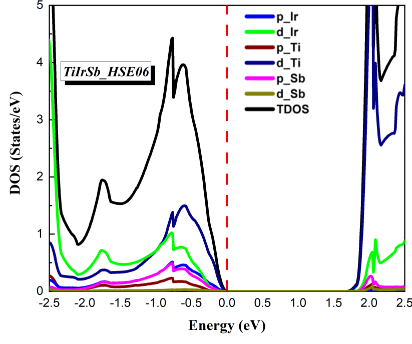

(a) HSE06 DOS - TiIrSb

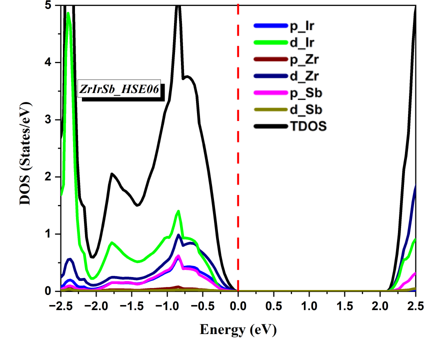

(b) HSE06 DOS - ZrIrSb

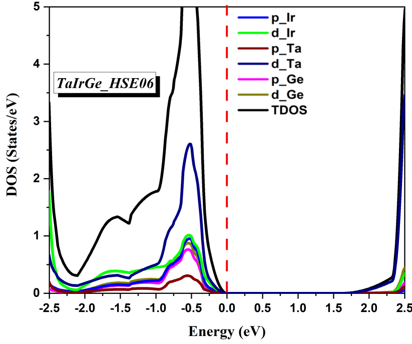

(c) HSE06 DOS - TaIrGe

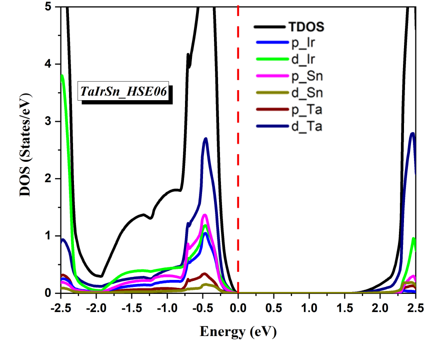

(d) HSE06 DOS - TaIrSn

Figure III.4: Total and partial density of states calculated using the HSE06 hybrid functional for the studied compounds.

III.1.5 Elastic and Mechanical Properties

Regarding the elastic constants, the calculated values of C_{11}, C_{12}, and C_{44} reflect the stiffness of the compounds and their response to various types of deformation. A high value of C_{11} indicates strong bonding strength along the principal crystallographic axes, while C_{12} represents the resistance of the material to volumetric (bulk) deformations. The constant C_{44} describes the material's ability to resist shear deformations.

By comparing the calculated results with previous theoretical and experimental studies, it is observed that the values are generally consistent, with minor discrepancies that can be attributed to differences in computational methods and measurement conditions.

For the Half-Heusler compounds crystallizing in the $F\bar{4}3m$ cubic structure, mechanical stability must satisfy the Born criteria for cubic systems [126]:

Mechanical Stability Criteria:

1. $C_{11} - C_{12} > 0$ **(Satisfied)**

2. $C_{11} + 2C_{12} > 0$ **(Satisfied)**

3. $C_{44} > 0$ **(Satisfied)**

Based on the obtained results, summarized in Table III.1, all investigated compounds fulfill the Born stability conditions, confirming their mechanical stability within the Half-Heusler structure.

To further evaluate the mechanical deformability of the compounds, the Bulk modulus (B) and Shear modulus (G) were calculated. The Bulk modulus represents the material's resistance to uniform compression, while the Shear modulus reflects its ability to withstand shear deformations. The ratio B/G is a useful indicator of the material's ductility, where values greater than 1.75 correspond to ductile and more elastic behavior, whereas smaller values indicate brittle and stiffer nature.

The TiIrSb and TaIrGe compounds exhibit higher B/G ratios, implying a more ductile and elastic character compared to ZrIrSb and TaIrSn, which are relatively more rigid. This observation is consistent with the overall elastic behavior obtained for these systems.

Regarding Young's modulus (E), which quantifies the stiffness of a material, the results show that TaIrGe and TaIrSn possess relatively higher values, indicating greater rigidity compared to the other compounds. These results are particularly relevant when assessing the suitability of these materials for practical mechanical applications.

Overall, the obtained results confirm the reliability of the adopted computational approach in predicting the structural and mechanical properties, showing good agreement with previous theoretical works. Furthermore, slight differences observed between the PBE and SCAN approximations highlight the improved accuracy of the SCAN functional, particularly in describing the mechanical response of semiconductor materials used in advanced technological applications.

Elastic Anisotropy Analyses for ABX Half-Heusler Systems

The elastic anisotropy[127] of ZrIrSb, TiIrSb, TaIrSn, and TaIrGe has been analyzed based on their calculated elastic constants. The Universal Elastic Anisotropy Index (A^U) values are found to be 0.01, 0.04, and 0.02 for ZrIrSb, TiIrSb, and TaIrSn, respectively, whereas TaIrGe exhibits a significantly higher anisotropy index of 0.32.

The two-dimensional (2D) representations of Young's modulus for these materials provide valuable insights into their anisotropic behavior. For ZrIrSb, TiIrSb, and TaIrSn, the

nearly circular contours observed in the three principal planes (ab, ac, and bc) indicate a nearly isotropic character, consistent with their very low anisotropy indices. This suggests that their mechanical response is uniform in all crystallographic directions.

In contrast, TaIrGe displays a more pronounced deviation from the circular pattern in its Young's modulus plots, reflecting higher directional dependence in its mechanical behavior. The relatively high anisotropy index ($A^U = 0.32$) indicates that TaIrGe possesses significantly greater elastic anisotropy compared to TiIrSb. Nevertheless, all compounds exhibit isotropic behavior in their bulk modulus, meaning their response to hydrostatic pressure remains uniform.

The observed increase in elastic anisotropy from ZrIrSb to TaIrGe is primarily attributed to the larger difference between C_{11} and C_{12} in TaIrGe. The higher C_{11} and C_{44} values correspond to greater stiffness, while the increased C_{12} enhances directional dependence. This anisotropic behavior in TaIrGe could influence its mechanical stability under shear and directional stresses, making it potentially suitable for applications requiring controlled directional stiffness.

To further examine the anisotropic behavior, the three-dimensional (3D) representations of Young's modulus were analyzed. For ZrIrSb, TiIrSb, and TaIrSn, the 3D plots exhibit nearly spherical shapes, confirming their isotropic nature. The uniform elastic response across various crystallographic orientations, with minimal variations in Young's modulus, indicates homogeneous mechanical behavior. This makes these compounds excellent candidates for applications where uniform mechanical stability is essential.

Conversely, the 3D Young's modulus surface of TaIrGe displays a more distorted, cube-like shape, significantly deviating from a perfect sphere. The noticeable variations in elastic stiffness along different crystallographic directions highlight its anisotropic mechanical response. This observation is consistent with the higher elastic anisotropy index and suggests that TaIrGe may exhibit direction-dependent mechanical performance under applied stress.

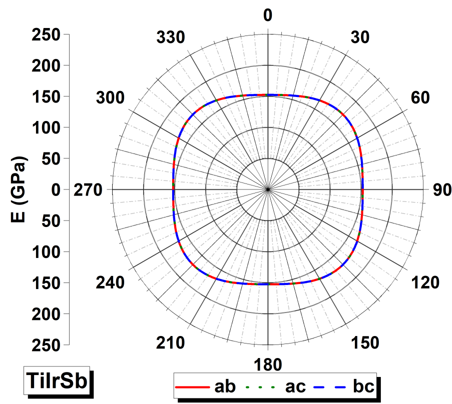

(a) 2D Young's modulus

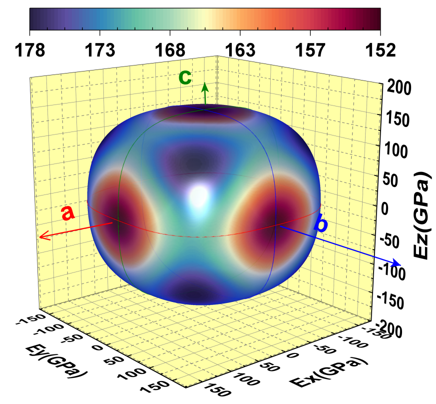

(b) 3D Young's modulus

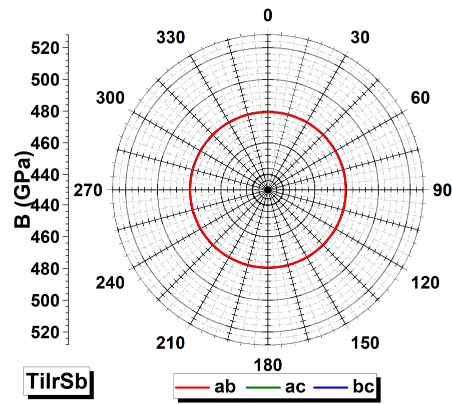

(c) 2D Bulk modulus

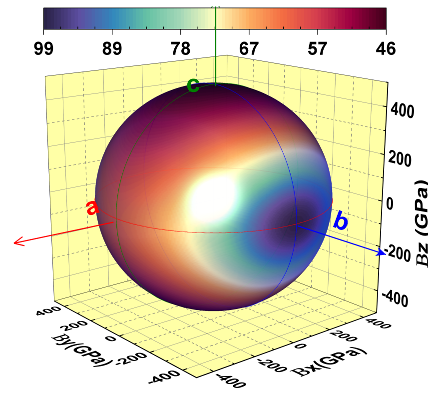

(d) 3D Bulk modulus

Figure III.5: 2D and 3D anisotropy representations of Young's and Bulk moduli for **TiIrSb**.

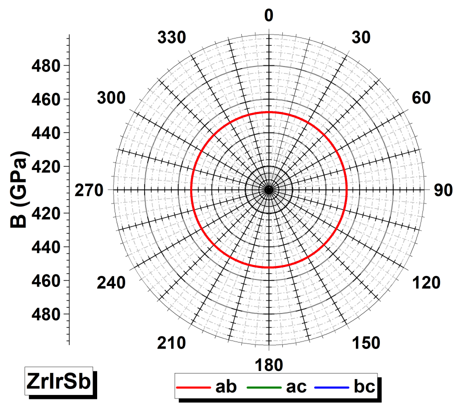

(a) 2D Young's modulus

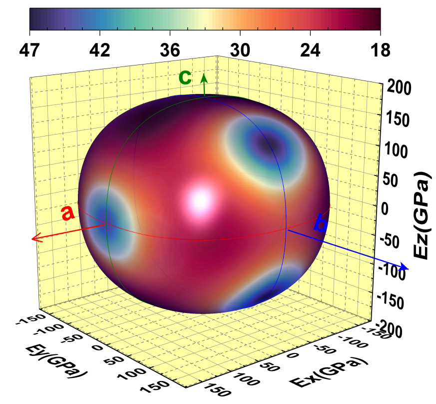

(b) 3D Young's modulus

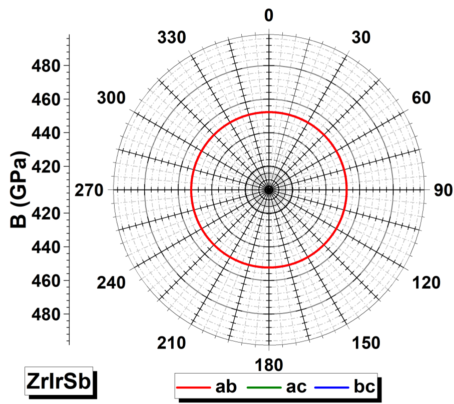

(c) 2D Bulk modulus

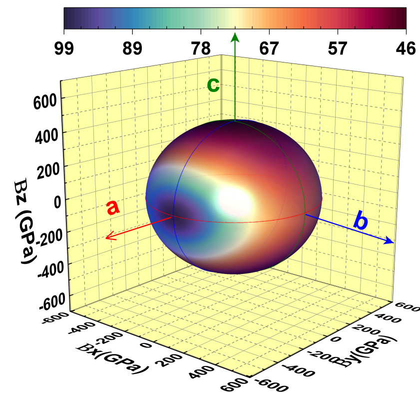

(d) 3D Bulk modulus

Figure III.6: 2D and 3D anisotropy representations of Young's and Bulk moduli for **ZrIrSb**.

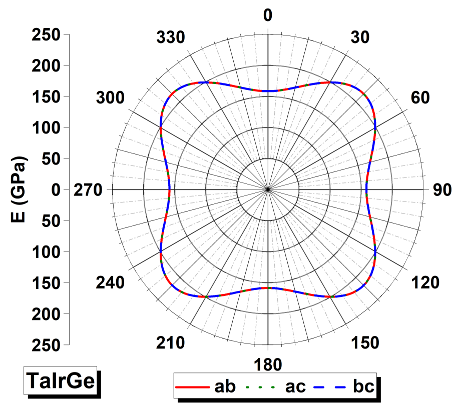

(a) 2D Young's modulus

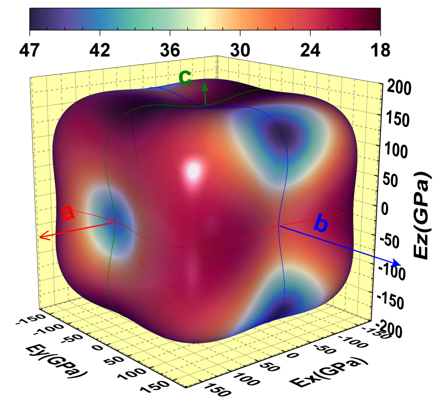

(b) 3D Young's modulus

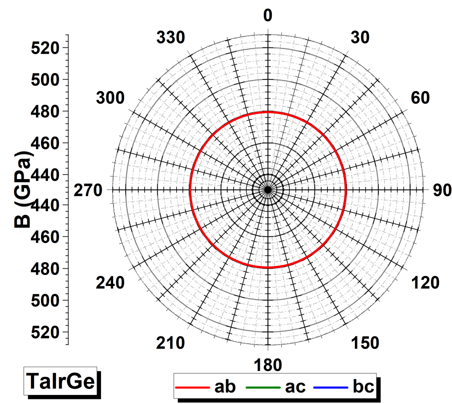

(c) 2D Bulk modulus

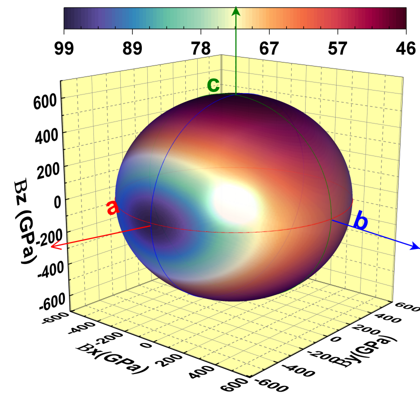

(d) 3D Bulk modulus

Figure III.7: 2D and 3D anisotropy representations of Young's and Bulk moduli for **TaIrGe**.

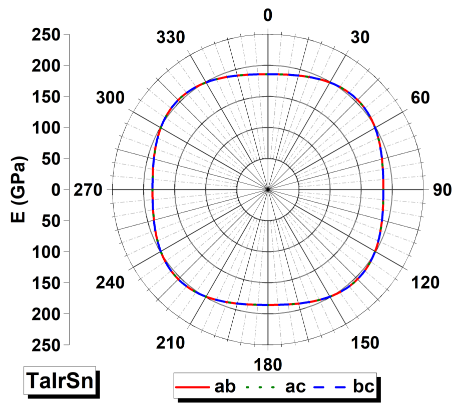

(a) 2D Young's modulus

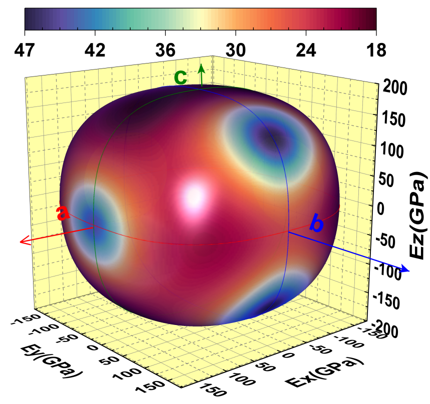

(b) 3D Young's modulus

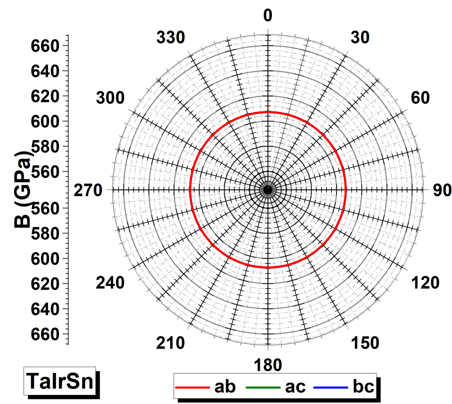

(c) 2D Bulk modulus

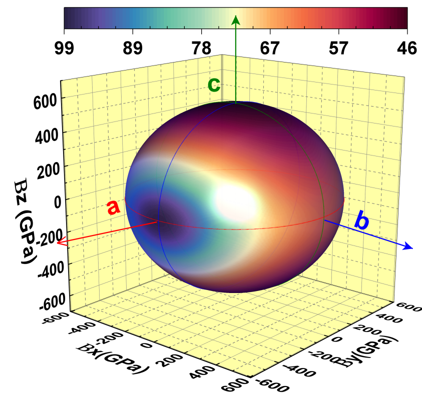

(d) 3D Bulk modulus

Figure III.8: 2D and 3D anisotropy representations of Young's and Bulk moduli for **TaIrSn**.

III.1.6 Optical Properties

The optical properties[128] of Half-Heusler compounds serve as a crucial indicator of their interaction with electromagnetic radiation, directly determining their suitability for applications such as solar cells, absorber layers, optical sensors, and selective coatings. By analyzing the real and imaginary parts of the dielectric function, along with other optical parameters including the absorption coefficient, reflectivity, refractive index, extinction coefficient, and energy loss function, a comprehensive understanding of the influence of chemical composition on optical response was achieved.

For the ZrIrSb compound, the real part of the dielectric function $\varepsilon_1(\omega)$ exhibits the lowest values among the studied systems (TiIrSb, TaIrGe, and TaIrSn). This reduction indicates a weaker polarization capability under the electric field of incident light, implying a lower density of responsive charge carriers. Such behavior can be attributed to the substitution of Ti with Zr, where differences in atomic size and bonding nature modify the

electronic density of states (DOS) near the Fermi level, thereby influencing the material's optical polarization.

A decrease in $\varepsilon_1(\omega)$ at low photon energies suggests that ZrIrSb stores less electromagnetic energy in this region, which is unfavorable for infrared or low-energy optical applications. In contrast, TiIrSb shows higher $\varepsilon_1(\omega)$ values, reflecting stronger polarization and enhanced light–matter interaction, consistent with its denser electronic states near the Fermi level.

Comparison between ZrIrSb and the Ta-based compounds (TaIrGe and TaIrSn) reveals that ZrIrSb exhibits moderate absorption at medium and high photon energies but limited absorption at lower energies, as indicated by its smaller $\varepsilon_2(\omega)$. This behavior corresponds to a relatively wide optical gap, resulting in partial transparency in the infrared region.

Conversely, TaIrGe and TaIrSn display stronger optical responses at low and intermediate energies, reflecting the influence of Ge and Sn in narrowing the band gap and increasing the density of states near the valence band edge. This variation highlights that chemical modification of the A and X sites within the Half-Heusler lattice is an effective strategy for tuning optical properties to meet specific application needs.

Overall, ZrIrSb exhibits a relatively weak low-frequency optical response and enhanced transparency, making it less suitable for high-absorption devices but potentially advantageous for transparent coatings or dielectric layers in multilayer structures, where a low dielectric constant and reduced internal reflection are desirable.

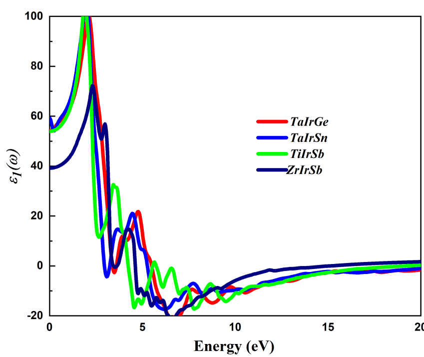

(a) Real part of the dielectric function $\varepsilon_1(\omega)$

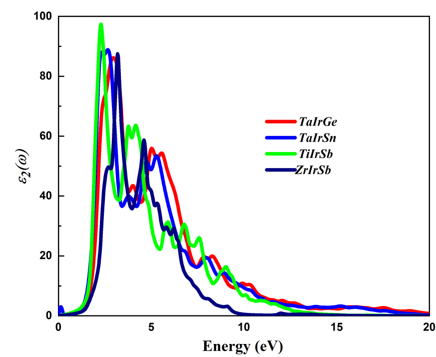

(b) Imaginary part of the dielectric function $\varepsilon_2(\omega)$

Figure III.9: Real and imaginary parts of the dielectric function for ABX Half-Heusler.

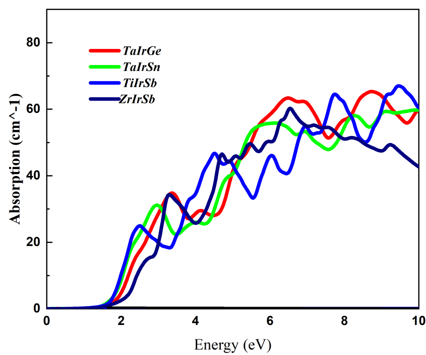

(a) Absorption coefficient $\alpha(\omega)$

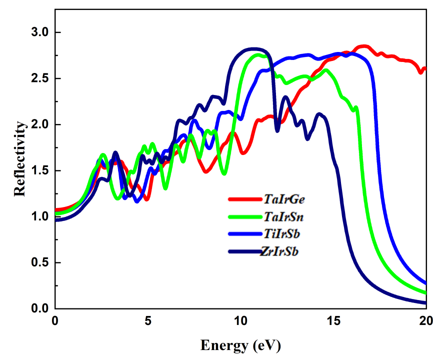

(b) Reflectivity $R(\omega)$

Figure III.10: Absorption coefficient and reflectivity for ABX Half-Heusler.

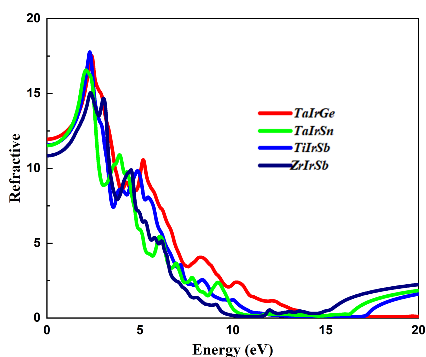

(a) Refractive index $n(\omega)$

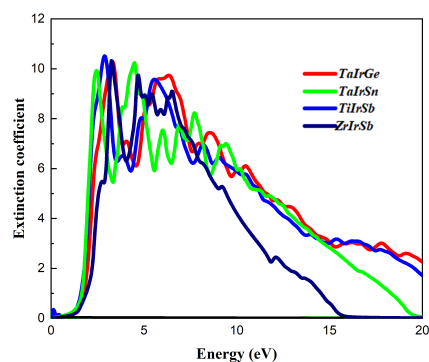

(b) Extinction coefficient $k(\omega)$

Figure III.11: Refractive index and extinction coefficient for ABX Half-Heusler.

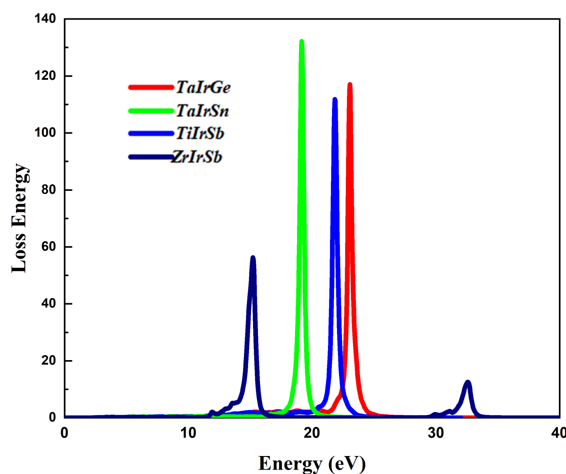

Figure III.12: Energy loss function $L(\omega)$ for ABX Half-Heusler.

III.1.7 Thermoelectric properties of ABX Half-Heusler alloys

Energy production is a fundamental aspect of any economy, requiring the efficient use of resources to minimize or eliminate waste. Given the current dependence on fossil fuels and the environmental challenges associated with waste management, the development of sustainable and efficient energy technologies has become essential. Thermoelectric materials offer a promising solution, as they enable the direct conversion of waste heat into electricity, thereby improving the efficiency of thermal systems and reducing overall energy losses.

In this study, the `BoltzTraP2` code was employed to calculate the electronic transport properties of TiIrSb, ZrIrSb, TaIrSn, and TaIrGe compounds. The analyzed transport parameters include the Seebeck coefficient (S), electrical conductivity ($\frac{\sigma}{\tau}$), and electronic thermal conductivity (κ_e) as functions of the Fermi level energy (E_F) at different temperatures ($T = 300, 600, 800$ K). These calculations provide valuable insights into the thermoelectric behavior of these Half-Heusler compounds, which have been rarely investigated.

The Seebeck coefficient represents the voltage generated across a material when subjected to a temperature gradient, driving the motion of charge carriers (electrons or holes) and inducing an electric current. Figure III.13(a–c) shows S as a function of the Fermi level. The results indicate that S reaches its maximum at $T = 300$ K and gradually decreases with increasing temperature. Variations among the compounds within the energy gap reveal differences in their thermoelectric performance and potential for energy conversion applications.

Electrical conductivity characterizes the ability of a material to transport electric current, which depends on the mobility and concentration of charge carriers. The contribution of free electrons was evaluated using $\frac{\sigma}{\tau}$, with its variation plotted as a function of the chemical potential at different temperatures (Figure III.13(d–f)). The results exhibit compound-dependent variations, with peak conductivity observed in specific chemical potential regions, while near the Fermi level, conductivity remains weak or nearly absent in some directions. This behavior reflects the influence of the electronic structure on transport properties.

The electronic thermal conductivity κ_e was also analyzed as a function of the Fermi level (Figure III.13(g–i)). The total thermal conductivity is expressed as $\kappa = \kappa_e + \kappa_l$, where κ_l represents the lattice contribution. Since electrons move faster than lattice vibrations,

κ_e plays a dominant role in heat transfer. The results show that κ_e varies depending on the compound and is strongly influenced by the position of the Fermi level. Its behavior closely follows that of electrical conductivity, confirming the strong correlation between electron transport and electronic heat conduction.

It was also observed that increasing temperature enhances both $\frac{\sigma}{\tau}$ and κ_e, reflecting the thermal excitation of charge carriers. Regions exhibiting high electrical conductivity correspond to high electronic thermal conductivity, confirming that electron flow predominantly governs electronic heat transfer in these materials. All studied compounds (TiIrSb, ZrIrSb, TaIrSn, and TaIrGe) exhibit low values of $\frac{\sigma}{\tau}$ and κ_e near the Fermi level, while higher values are observed at negative and positive chemical potentials (Figure III.13(d–i)).

It should be noted that the dimensionless figure of merit (ZT) was not calculated in this study. Nevertheless, the analysis of the Seebeck coefficient, electrical conductivity, and electronic thermal conductivity provides meaningful insights into the thermoelectric behavior of TiIrSb, ZrIrSb, TaIrSn, and TaIrGe compounds, offering a basis for future optimization strategies aimed at improving their thermoelectric performance.

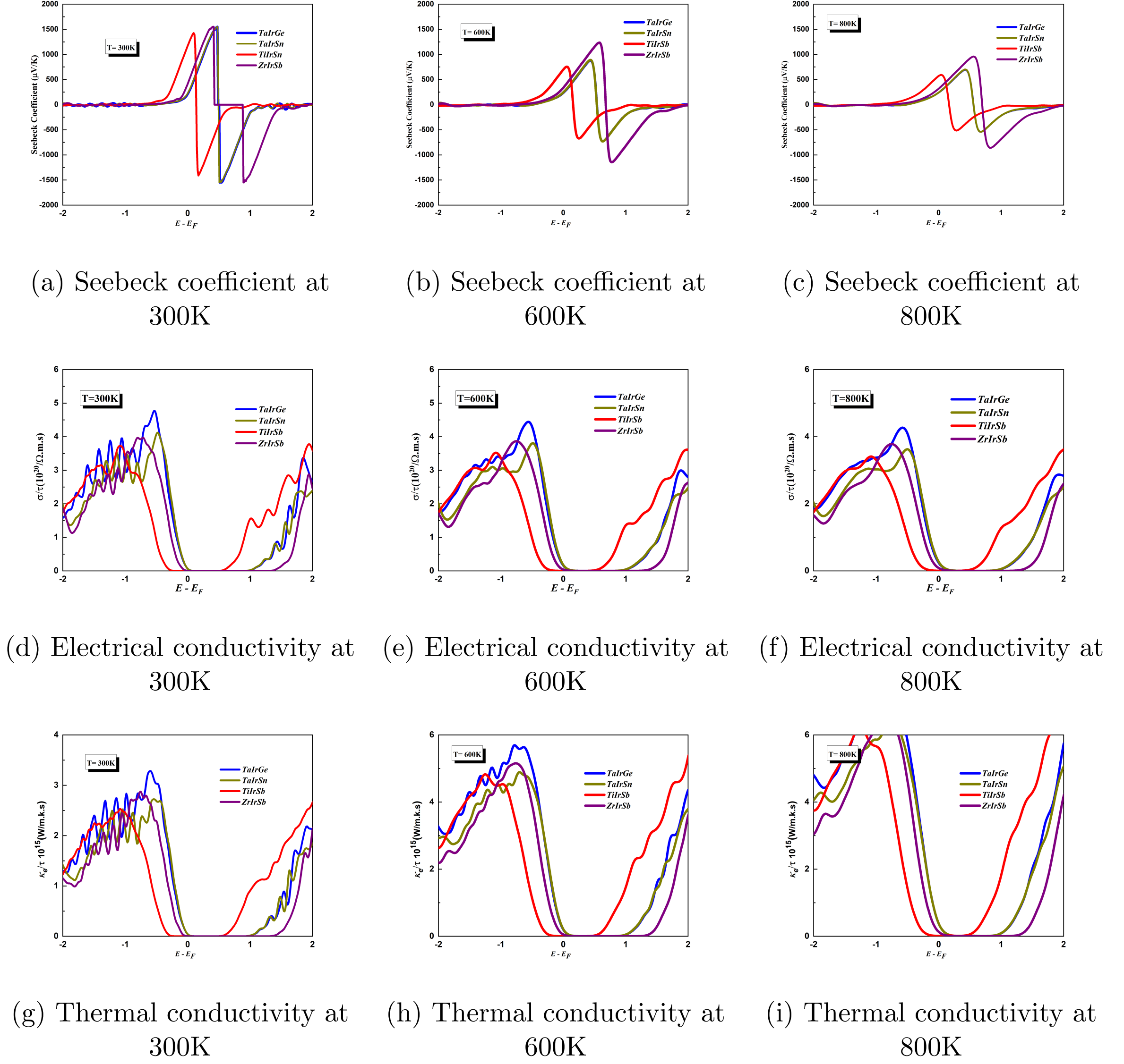

(a) Seebeck coefficient at 300K

(b) Seebeck coefficient at 600K

(c) Seebeck coefficient at 800K

(d) Electrical conductivity at 300K

(e) Electrical conductivity at 600K

(f) Electrical conductivity at 800K

(g) Thermal conductivity at 300K

(h) Thermal conductivity at 600K

(i) Thermal conductivity at 800K

Figure III.13: Thermoelectric properties of ABX at different temperatures

III.1.8 Conclusion

In this chapter, the physical properties of TiIrSb, ZrIrSb, TaIrSn, and TaIrGe compounds were investigated using first-principles calculations based on density functional theory (DFT). The study encompassed structural, electronic, mechanical, optical, and thermoelectric analyses to assess the stability and potential applicability of these materials in advanced technologies.

The results confirmed that all compounds are structurally and mechanically stable, satisfying the Born stability criteria and the elastic constant conditions (C_{ij}). The electronic band structure and density of states (DOS) analyses revealed the presence of well-defined band gaps, confirming the semiconducting nature of the studied Half-Heusler systems.

Regarding the optical properties, the compounds exhibited a strong response in the ultraviolet region, suggesting their suitability for optoelectronic and photovoltaic applications. Thermoelectric calculations performed using the `BoltzTraP2` code showed notable Seebeck coefficients (S) and electrical conductivities (σ/τ), accompanied by moderate electronic thermal conductivities (κ_e), indicating promising thermoelectric performance that can be further enhanced through structural optimization.

Overall, this study demonstrates that the investigated Half-Heusler alloys possess desirable semiconductor characteristics, combining mechanical robustness with favorable electronic, optical, and thermoelectric properties. These features make them promising candidates for multifunctional applications, where performance can be tailored through band gap tuning and controlled defect or substitutional engineering.

III.2 Theoretical insights into off-stoichiometric $Zr_xTi_{1-x}IrSb$

III.2.1 Introduction

Half-Heusler alloys are among the promising materials in the fields of energy and electronics[33], due to their controllable electronic, optical and mechanical properties through modification of the chemical composition. In this context, this chapter aims to shed light on the previously published theoretical study entitled: "Theoretical insights into off-stoichiometric $Zr_xTi_{1-x}IrSb$ half-Heusler alloys: a first principle calculations"[46], which represents an essential part of the research work of this thesis. This study is centered on the theoretical investigation of the phase stability and electronic and optical properties of a series of off-stoichiometric $Zr_xTi_{1-x}IrSb$ alloys at different composition ratios (x = 0, 0.0625,0.125, 0.1875, 0.25, 0.50, 0.75, 1). First-principles calculations were performed using the VASP package and based on GGA-PBE[78, 80] and Meta-GGA-SCAN[120] approximations to analyze the optical, electronic and structural properties of these alloys. The dynamic stability of each composition was evaluated using Phonopy software by calculating vibrational frequencies.

The results showed that these alloys exhibit semiconductor behavior with a controllable energy gap, which makes them strong candidates for applications in electronic and optical devices. The optical properties showed a variable response with different chemical compositions, especially in the visible light range, which enhances their potential for use in optical and photovoltaic applications. In addition, the study confirmed the excellent dynamic stability of all studied compositions, which supports the possibility of their practical fabrication.

Based on these results, this chapter provides an in-depth reading of the effect of partial replacement of titanium with zirconium on the electronic, optical and dynamic structures of TiIrSb alloys, which contributes to enhancing the understanding of the relationship between the structural composition and physical properties of these materials, and directing research efforts towards designing new Half-Heusler(HH) alloys with improved performance that meet the requirements of modern technological applications.

III.2.2 Computational methodology

In our computational work, we have systematically investigated the electronic, dynamic, and optical properties of $Zr_xTi_{1-x}IrSb$ half-Heusler alloys using advanced methods. The projector-augmented plane wave (PAW) method [129], was employed in conjunction with Density Functional Theory (DFT) [75], using the Vienna Ab initio Simulation Package (VASP) [100]. For the exchange-correlation potential, we utilized the Generalized Gradient Approximation developed by Perdew et al. (GGA-PBE) [78], and the meta-GGA-SCAN functional [87, 130]. Given the known tendency of GGA to underestimate band gaps, the SCAN functional was adopted to enhance the accuracy of our band gap calculations.

The basic unit cell of XIrSb (X=Ti, Zr) contains three atoms. To explore the $Zr_xTi_{1-x}IrSb$ alloys comprehensively, we constructed a 2x2x1 supercell with 48 atoms using the Site Occupation Disorder (SOD) package, illustrated in Figure III.15. This allowed us to create various Zr-substituted configurations for x values of 0, 0.0625, 0.125, 0.1875, 0.25, 0.50, 0.75, and 1. Each concentration (x) characterized by n substitutions of Ti by Zr. For our predictions, we considered the valence states of Ti ($3d^2$ $4s^2$), Zr ($4d^2$ $5s^2$), Ir ($5d^7$ $6s^2$), and Sb ($5s^2$ $5p^3$). Within the 2 × 2 × 1 supercell containing N = 16 Ti sites, there are $\frac{N!}{n!(N-n)!}$ possible ionic configurations, However, only the symmetrically unique configurations were computed, as determined by the Site Occupancy Disorder (SOD) program [131]. Specifically, there are 120 unique configurations for x=0.125, 1820 for x=0.25, and 560 for x=0.75. For each unique configuration, total energies were calculated to determine the most stable state. Phonon calculations were performed using the finite difference method with the Phonopy package [102] to confirm the dynamic stability of these configurations. The formation energy E_f [eV/atom] and formation enthalpy $\Delta H_f[eV/atom]$ were calculated to establish thermodynamic stability across different compositions, using the following equations Eq.III.1 and Eq.III.2 respectively:

$$E_f(Zr_xTi_{(1-x)}IrSb) = \frac{[E(Zr_xTi_{(1-x)}IrSb) - 16xE^{bulk}(Zr) - 16(1-x)E^{bulk}(Ti) - 16E^{bulk}(Ir) - 16E^{bulk}(Sb)]}{N} \tag{III.1}$$

$$\Delta H_f(Zr_xTi_{(1-x)}IrSb) = \frac{[E(Ti_{16}Ir_{16}Sb_{16}) - xE(Zr)^{bulk} - (1-x)E(Ti)^{bulk} - E(Ir)^{bulk} - E(Sb)^{bulk}]}{N} \tag{III.2}$$

To ensure the accuracy of our structural and mechanical property calculations for the

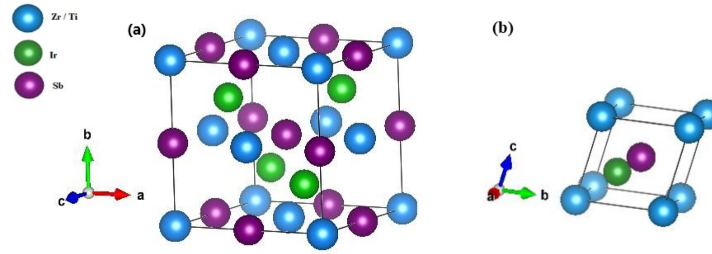

H

Figure III.14: Structure of XIrSb (X = Ti, Zr) compounds, (a) and (b) represent conventional and primitive cells, respectively.

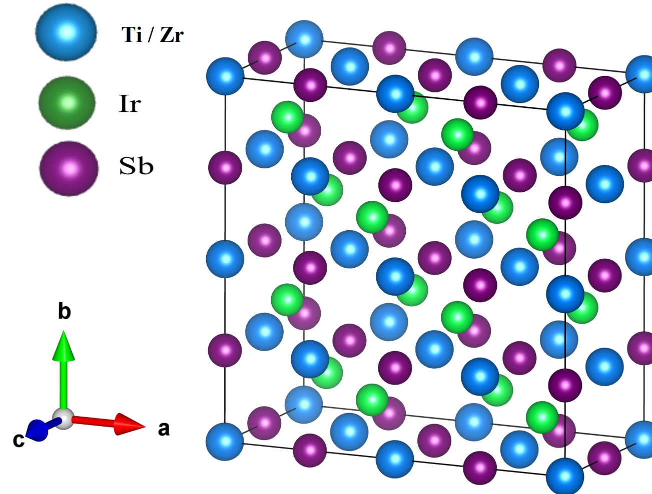

H

Figure III.15: Schematic representation 2×2×1 perfect supercell of XIrSb (M=Ti, Zr) with 48 atoms.

bulk XIrSb (X=Ti, Zr), we used a stringent convergence criterion for the self-consistent electronic loop, with a tolerance energy of $10^{-6}eV$. Additionally, a high-density k-point mesh of 11x11x11 was employed during our total energy calculations, while the kinetic energy cutoff is fixed at 600 eV for the plane-wave expansion of the electronic wave functions. A supercell of $2 \times 2 \times 1$ containing 48 atoms is then generated using SOD to explore the electronic, dynamic, and optical properties of $Zr_xTi_{1-x}IrSb$ alloys. This supercell approach allowed us to simulate various concentrations of Zr by substituting Ti atoms with Zr atoms, specifically at x= 0, 0.0625, 0.125, 0.1875, 0.25, 0.50, 0.75, 1. Given the computational demands of such simulations, we adopted a strategy to balance accuracy and computational efficiency. For the supercell calculations, we reduced the cutoff energy to 390 eV and used a lower sampling density for the k-point mesh, specifically 3×3×5. This adjustment helps to decrease computational costs while maintaining sufficient accuracy for our investigations.

III.2.3 Configuration built using the Site Occupation Disorder (SOD)

After acquiring the relaxed structure, we generated a pristine supercell TiIrSb with dimensions 2x2x1, encompassing a total of 48 atoms (see Fig.III.15). This was achieved using the Site-Occupation Disorder (SOD) package [132], which then enabled us to perform substitutions of atoms within the 2x2x1 supercell to form $Zr_xTi_{1-x}IrSb$ structure at different concentrations, where x={0, 0.0625, 0.125, 0.1875, 0.25, 0.50, 0.75, 1}. In these substitutions, titanium atoms (Ti) were replaced with zirconium atoms (Zr) within the supercell.

For each concentration, a number of possible configurations were created. Table.III.3 shows the results obtained through this process, where $N_S[Sites]$ represents the number of substitutions and the total sites in the supercell, C_T and C indicate the number total and inequivalent configurations respectively [132, 133]. Indeed, the algorithms on which the SOD program is based made it possible to reduce the large number of total configurations to a smaller set of symmetrically unique configurations. For instance, at a concentration of 0.0625, the total number of configurations decreased from 16 to 1. Similarly, for concentrations of 0.125, 0.1875, 0.25, and others, the number of configurations was reduced from 120 to 5, from 560 to 10, and so forth, as detailed in Table.III.3. This approach simplifies our path toward identifying the most stable configuration. For each concentration, we calculated the energy of all configurations to determine the most stable state with the lowest energy (see Fig.III.16). The most stable configuration was then used in our calculations of the physical properties of the alloys, rather than considering all possible configurations. The Fig.III.16 shows the energy values plotted against the concentration x . This plot provides a clear visualization of the stability trends across different compositions of $Zr_xTi_{1-x}IrSb$. As it can be seen, there are significant variations in energy with changing x values, highlighting the importance of accurately determining the most stable configuration for each composition. In the lower concentration range ($0.00 \leq x \leq 0.25$), the energy values show relatively small variations, indicating that the substitution of Zr into TiIrSb does not drastically alter the stability initially. This suggests that low Zr doping levels might be energetically feasible with minimal structural disruption. At intermediate concentrations ($0.25 \leq x \leq 0.50$), there is a noticeable increase in the dispersion of energy values. Specifically, at x= 0.5, a substantial number of configurations exhibit

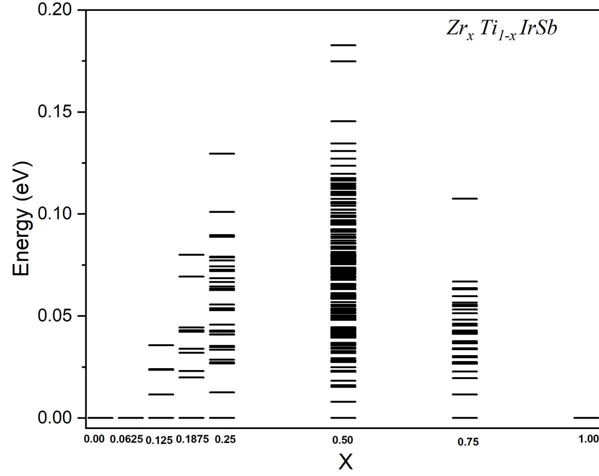

Figure III.16: The lowest energy configurations for each composition of $Zr_xTi_{(1-x)}IrSb$ alloys, determined using the GGA-PBE functional.

Table III.3: The number of possible substitutions in sites $N_S[Sites]$, the total number of configurations (C_T), and the number of inequivalent configurations (C) calculated for $Zr_xTi_{(1-x)}IrSb$ alloys using the SOD package.

Super-cell	$Concentration(x)$	$N_S[Sites]$	C_T	C
2x2x1	0.00	0[16]	1	1
2x2x1	0.0625	1[16]	16	1
2x2x1	0.125	2[16]	120	5
2x2x1	0.1875	3[16]	560	10
2x2x1	0.25	4[16]	1820	33
2x2x1	0.50	8[16]	12870	153
2x2x1	0.75	12[16]	560	33
2x2x1	1.00	16[16]	1	1

higher energy, implying that achieving stability in this region is more challenging. This concentration range is critical as it represents a balance point between Ti and Zr, leading to a variety of local atomic environments and potential strain effects. On the other hand, as the Zr concentration increases further, particularly from x= 0.75 to x= 1, the energy values once again become more localized. However, unlike the low concentration range, the energies here are generally higher compared to the pure TiIrSb (x=0) or ZrIrSb (x=1) compounds, indicating that high Zr doping introduces more significant structural changes and potential instability.

As a result, among all studied compositions,$Zr_{0.50}Ti_{0.50}IrSb$ demonstrates the highest energy dispersion, suggesting that this specific alloy composition might be less favorable due to increased structural strain and disorder.

III.2.4 Thermodynamic Stability of $Zr_xTi_{1-x}IrSb$ Alloys

The thermodynamic stability of $Zr_xTi_{(1-x)}IrSb$, at different concentrations is examined by evaluating their defect formation energy E_f [eV/atom] and enthalpy ΔH_f [eV/atom]. These parameters are crucial in determining the likelihood of a material's stability and its potential practical applications [134, 135]. In our study, the values of E_f[eV/atom] and ΔH_f[eV/atom] were calculated using equations previously outlined Eq.III.1 and Eq.III.2, employing the Generalized Gradient Approximation (GGA).

Fig.III.17 presents the variations of the both parameters as a function of composition (x). The blue squares represent the enthalpy of formation ΔH_f[eV/atom], and the red squares represent the defect formation energy E_f[eV/atom] . As it can be seen from the figure, both properties exhibit negative values across all compositions, indicating the thermodynamic stability of the alloys. The defect formation energy curve (red line) rises with increasing Zr concentration. This trend suggests that the introduction of Zr into the TiIrSb matrix makes the formation of defects energetically more favorable, up to a certain point. The rise in E_f[eV/atom] with increasing Zr content indicates that the defects formed are less likely to destabilize the alloy, thereby contributing positively to its overall stability. The consistent negative values of E_f[eV/atom] across all compositions underscore the alloy's robustness against defect formation. Similarly, the enthalpy of formation ΔH_f[eV/atom] curve (blue line) also rises with increasing Zr content but at a slightly different rate compared to E_f[eV/atom]. The negative values of ΔH_facross all compositions confirm the exothermic nature of the alloy formation, meaning that energy is released during the formation process. This exothermic behavior is a strong indicator of the thermodynamic favorability and stability of the $Zr_xTi_{(1-x)}IrSb$ alloys. In other word, the negative values of both ΔH_f and E_f demonstrate the thermodynamic stability of the compounds. The stability of these alloys implies that they can exist in natural conditions without significant decomposition or transformation. This characteristic makes them suitable for various applications, particularly in environments where thermal and structural stability are crucial. The dynamic stability inferred from these results provides a basis for further investigation into the practical applications of these alloys. They could potentially be used in high-temperature environments or as components in thermoelectric devices, where stability and efficiency are paramount.

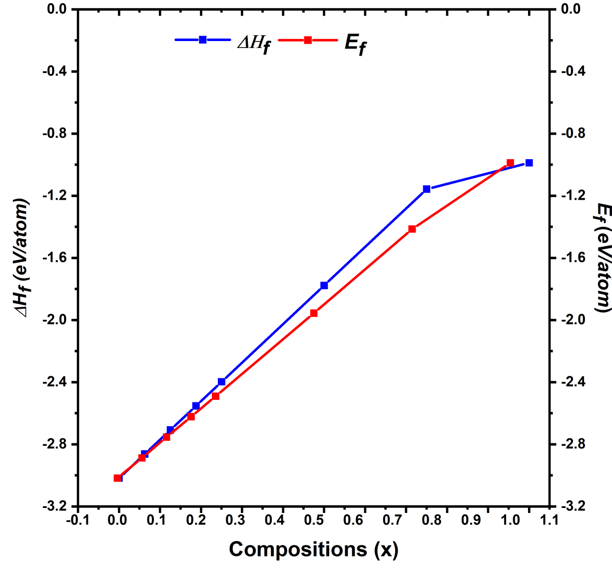

Figure III.17: The variations of formation energy $E_f[eV/atom]$ (blue line) and enthalpy $\Delta H_f[eV//atom]$(red line) for $Zr_xTi_{1-x}IrSb$ as a function of concentration (x)

III.2.5 Dynamical Stability

Phonon calculations are essential for verifying the stability of stoichiometric and non-stoichiometric half-Heusler (HH) alloys[136]. Stability is indicated by the absence of negative frequencies in the phonon dispersion spectra. Moreover, phonon dispersion spectra and phonon density of states (PhDOS) play a pivotal role in determining many physical properties of materials, including structural stability, phase transitions, and the impact of vibrations on thermal and charge transport properties [137, 138]. In this section, we calculate the phonon band dispersion and PhDOS for $Zr_xTi_{1-x}IrSb$ at each concentration x, along the high symmetry directions of the Brillouin zone (BZ). These calculations are crucial as they help in understanding the dynamic behavior of the alloys under various compositional changes. The Fig.III.18 illustrates the phonon band dispersion and PhDOS for pristine TiIrSb and ZrIrSb structures (x = 0.00 and 1.00). The low-frequency range, between 0 cm^{-1} and approximately 130 cm^{-1}, corresponds to the acoustic branches. These branches are primarily contributed by Ir and Sb atoms. Acoustic phonons are significant as they are responsible for the transfer of thermal energy in semiconductors and insulators[139]. Higher frequencies, up to 220 cm^{-1} correspond to the optical branches, which are mainly influenced by Ti and Zr atoms. Optical phonons typically involve higher energy vibrations and can affect the material's interaction with electromagnetic waves and

its thermal properties. On other hand, Fig.III.19 and Fig.III.20 present the phonon dispersion and PhDOS for doped $Zr_xTi_{1-x}IrSb$ alloys across various compositions (x). The positive frequencies observed across all compositions confirm that these alloys are dynamically stable. The stability is crucial for potential applications as it implies that the materials will not undergo spontaneous structural changes under normal conditions. Up to around 200 cm^{-1}, a distinct separation between the upper and lower branches is noted, except for the composition with x = 0.0625, where a narrow gap and contact between modes are observed at the Gamma point of the Brillouin zone (see Fig.III.19). This contact can significantly influence the material's physical properties, such as thermal conductivity and electrical conductivity. The gap formation is primarily due to differences in atomic masses, affecting the vibrational frequencies of phonons, which depend on $\sqrt{\frac{k}{m}}$ (where k represents the force constants and m the atomic masses). The phonon band dispersion and PhDOS curves (see Fig.III.19 and Fig.III.20) indicate that Sb and Ir atoms predominantly contribute to the acoustic branches at low frequencies. These contributions are vital for understanding thermal transport properties, as acoustic phonons play a significant role in heat conduction. On the other hand, Ti and Zr atoms are more involved in high-frequency optical modes. The optical phonons, while not contributing significantly to thermal transport, are crucial for understanding other material properties, such as interactions with light and other electromagnetic waves.

In summary, The detailed phonon analysis of $Zr_xTi_{1-x}IrSb$ alloys underscores their dynamic stability and provides insights into their potential applications. The absence of negative frequencies across all compositions affirms the alloys' stability, while the separation and contact points within the phonon spectra suggest significant implications for thermal and electrical properties. Understanding the contributions of different atoms to the acoustic and optical branches further elucidates the material's behavior, paving the way for its use in high-performance applications where thermal and structural stability are paramount.

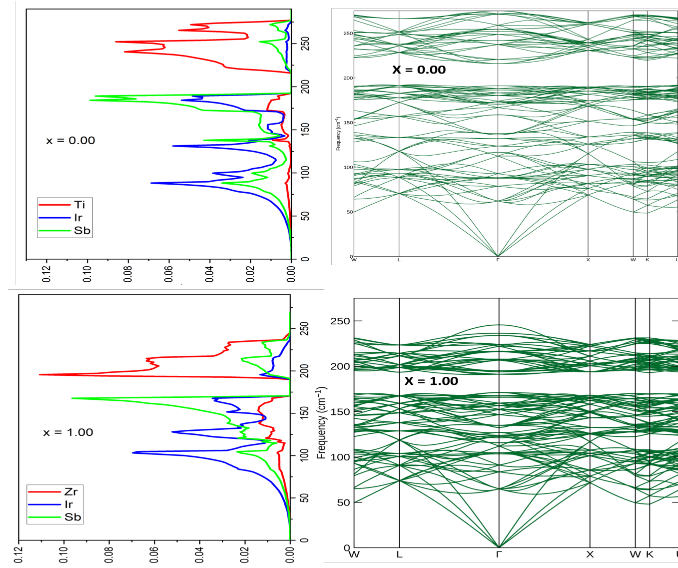

Figure III.18: phonon band dispersion of bulk structure and partial density of states of the pristine 2x2x1 super-cell.

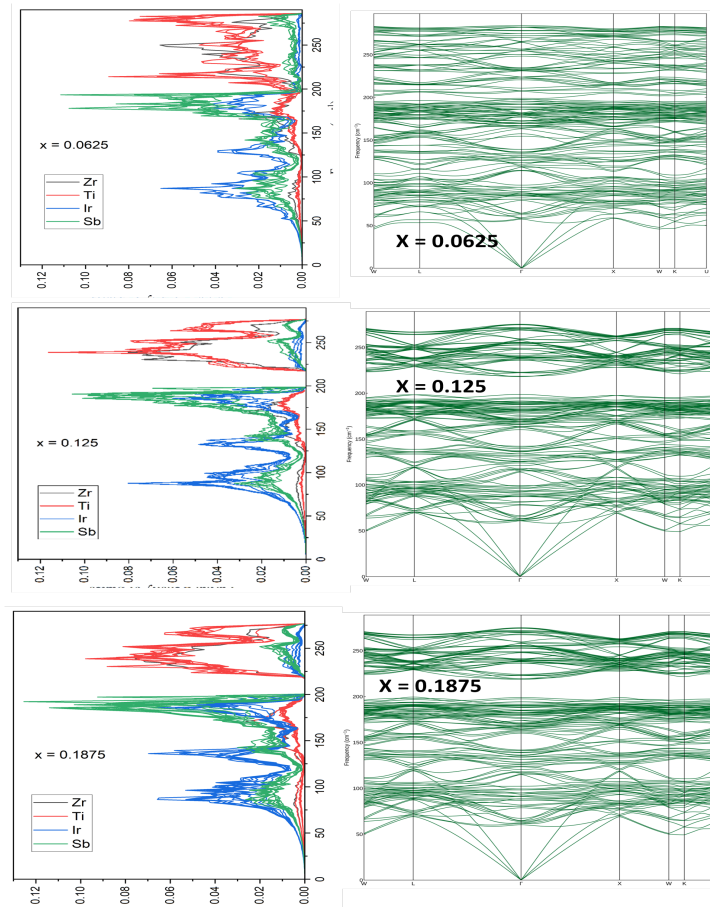

Figure III.19: Phonon band structure and density of states of individual atoms in $Zr_xTi_{1-x}IrSb$ alloys at x={0,0.0625, 0.125, 0.1875.

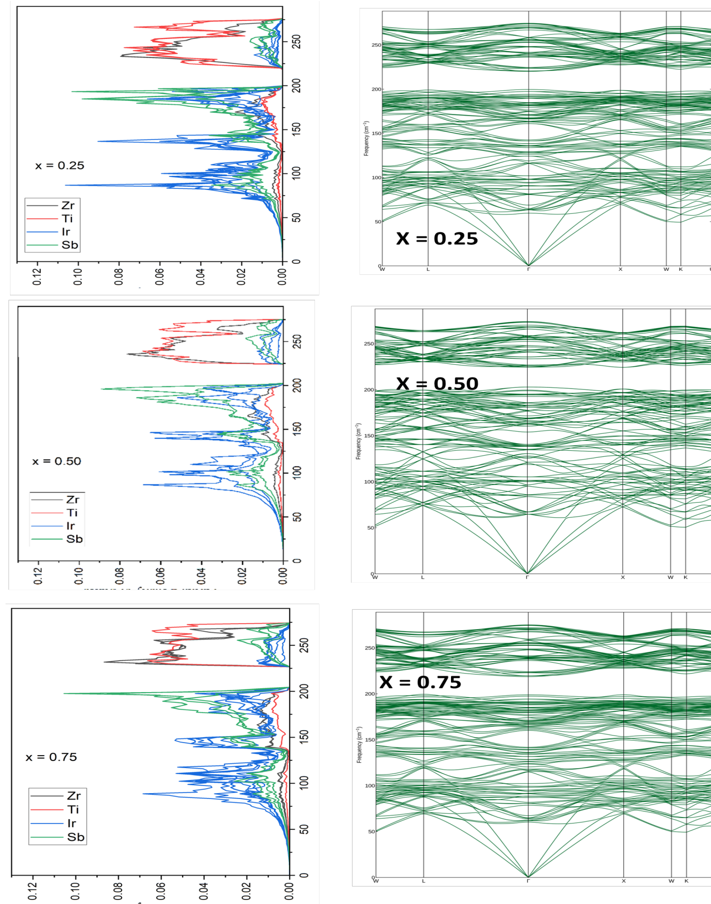

Figure III.20: Phonon band structure and density of states of individual atoms in $Zr_xTi_{1-x}IrSb$ alloys at x=0,0.25, 0.50, 0.75

.

III.2.6 Electronic Properties of $Zr_xTi_{1-x}IrSb$ Alloys

In this section, we present a detailed analysis of the electronic properties of $Zr_xTi_{1-x}IrSb$ alloys, examining various concentrations (x) and the performance of exchange-correlation approximations using PBE and SCAN functionals.

We conducted a thorough examination of the electronic properties of pristine XIrSb (X=Ti,Zr) and $Zr_xTi_{1-x}IrSb$ alloys by analyzing their band gap energies, band structures, and density of states. Fig.III.21 illustrates the calculated band structures of pristine XIrSb (X=Ti,Zr) using both PBE and SCAN functionals. These band structures reveal that both compounds are indirect semiconductors with band gaps occurring between the $\mathbf{\Gamma}$ and X points. Specifically, the valence band maximum (VBM) is located at the $\mathbf{\Gamma}$ point, while the conduction band minimum (CBM) is at the X point. The calculated gap energies are approximately 0.838 eV (0.994 eV) for TiIrSb and 1.411 eV (1.764 eV) for ZrIrSb using PBE (SCAN) functionals, respectively. These values are consistent with previous

studies [14, 124, 139–141],which confirms the reliability of our computational approach.

In contrast, the band structures for the $2 \times 2 \times 1$ supercell (48 atoms) of $Zr_xTi_{1-x}IrSb$ alloys, depicted in Fig.III.22 and Fig.III.23 reveal a direct band gap due to band folding. Increasing the unit cell size by creating a supercell effectively reduces the size of the Brillouin zone. As a result, bands that were outside the smaller Brillouin zone of the primitive cell are folded back into the new, smaller Brillouin zone of the supercell. This can lead to significant changes in the electronic band structure, including the transition from indirect to direct band gaps [138]. The electronic band structures plotted for both TiIrSb and ZrIrSb highlight the indirect nature of the band gaps in the primitive cells. The transition from an indirect to a direct band gap observed in the supercell calculations is a crucial finding for optoelectronic applications, where direct band gaps are more desirable for efficient light emission and absorption processes. The band gap (Eg) values obtained for $Zr_xTi_{1-x}IrSb$ at various concentrations (x) using PBE and SCAN approximations are presented in Fig.III.24 and listed in Table.III.4. The calculated band gap values range from approximately 0.84 eV to 1.41 eV for PBE and 0.99 eV to 1.49 eV for SCAN. These results show a clear dependence on the concentration of zirconium. As Zr concentration increases, the band gap widens, indicating that the electronic structure can be finely tuned by adjusting the Zr/Ti ratio. At $x=0.0625$, the band gap decreases. This decrease is primarily attributed to lattice distortions and changes in the electronic environment caused by the substitution of Ti with Zr. This substitution disrupts the periodicity of the TiIrSb host lattice, introducing localized states and modifying bonding characteristics, which results in a narrower band gap. Additionally, disorder effects and the possible formation of defect states at this specific concentration contribute to the observed discontinuity in the electronic band structure. The ability to tune the band gap is advantageous for designing materials with specific electronic properties for targeted applications. For instance, materials with larger band gaps may be more suitable for high-temperature semiconducting applications, while those with narrower gaps could be better for infrared sensors and detectors. Moreover, the comparison between the PBE and SCAN functionals reveals that SCAN generally predicts larger band gaps. This is expected due to SCAN's more sophisticated treatment of exchange-correlation effects, which provides a more accurate representation of electronic properties. These results highlight the importance of functional choice in computational studies and its impact on predicting material properties.

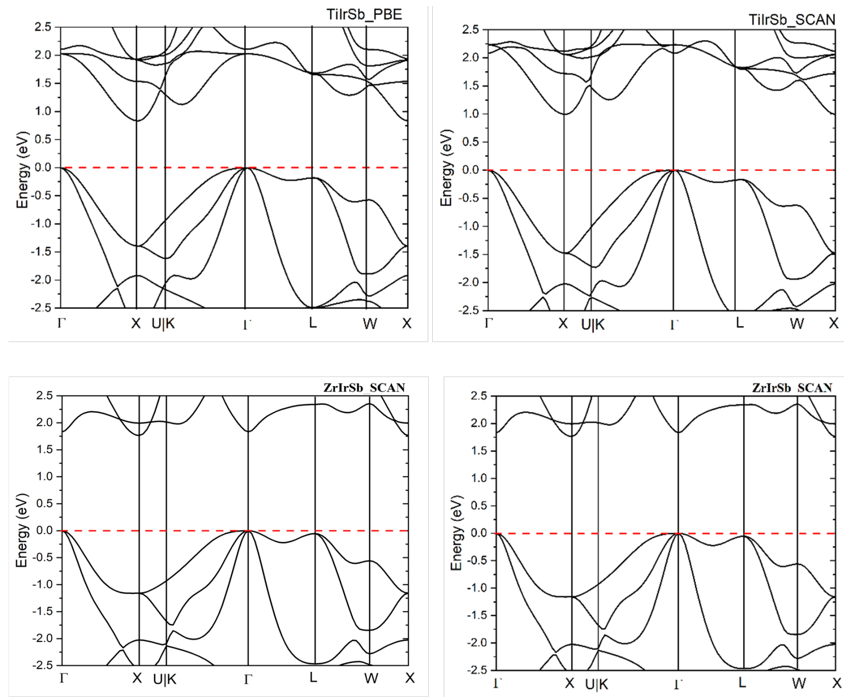

Figure III.21: The band structures of TiIrSb and ZrIrSb are re-displayed for comparison with the defective structures.

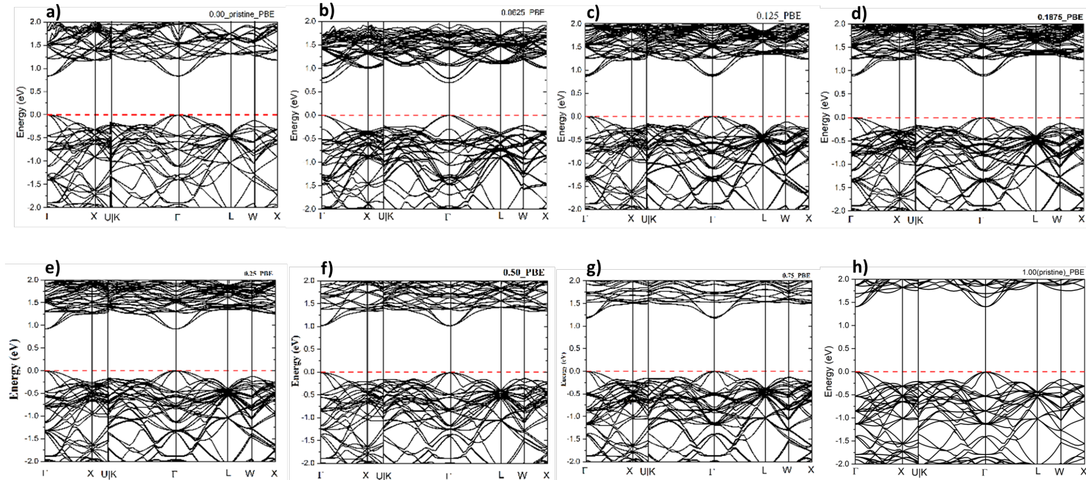

Figure III.22: Calculated band structure of $Zr_xTi_{1-x}IrSb$ alloys using PBE, (a) x=0.00, (b) x=0.0625, (c) x=0.125, (d) x=0.1875, (e) x=0.25, (f) x=0.5, (g) x=0.75, (h) x=1.00.

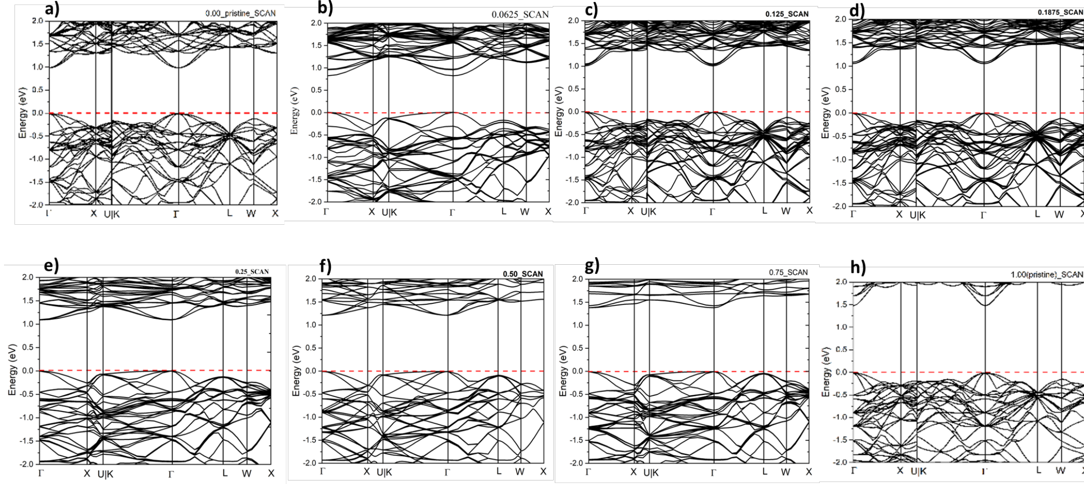

Figure III.23: Calculated band structure of $Zr_xTi_{1-x}IrSb$ alloys using SCAN, (a) x=0.00, (b) x=0.0625, (c) x=0.125, (d) x=0.1875, (e) x=0.25, (f) x=0.5, (g) x=0.75, (h) x=1.00.

Concentrations (x)	**Eg (eV)**	
	PBE	SCAN
0.00	0.836	0.994
0.0625	0.692	0.819
0.125	0.860	1.022
0.1875	0.890	1.057
0.25	0.920	1.092
0.50	1.027	1.213
0.75	1.173	1.386
1.00	1.412	1.486

Table III.4: The calculated energy band gap Eg (eV) of $Zr_xTi_{1-x}IrSb$ alloys using PBE and SCAN.

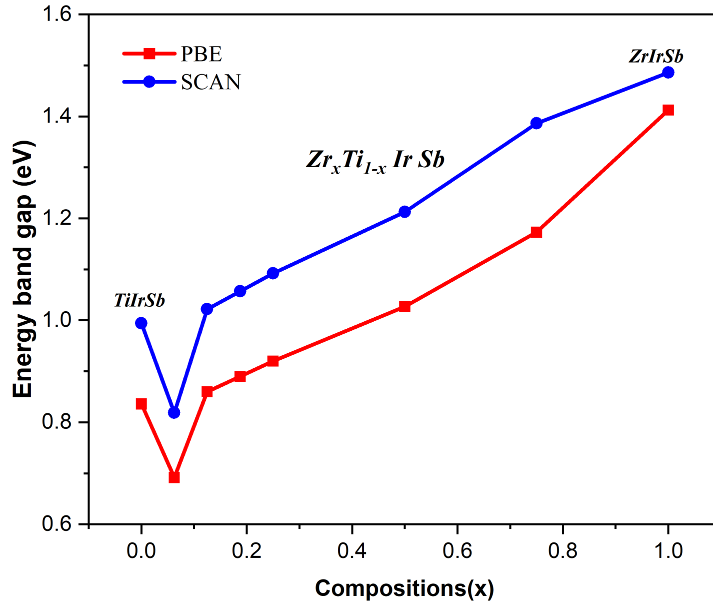

Figure III.24: The variation energies band gap values as a function concentrations x of $Zr_xTi_{1-x}IrSb$ alloys using PBE and SCAN.

To further understand the electronic properties, the Total Density of States (TDOS) and Partial Density of States (PDOS) curves for $Zr_xTi_{1-x}IrSb$ alloys, as shown in Fig.III.25 and Fig.III.26 , provide a detailed insight into the electronic structure and the contributions of different atomic orbitals to the electronic states near the Fermi level. The TDOS curves illustrate the overall density of electronic states available at each energy level, while the PDOS curves break down these states into contributions from specific atomic orbitals. From the PDOS, it is evident that the d-orbitals of both Ti/Zr and Ir atoms play a significant role in the formation of the band gap. The Ir d-orbitals predominantly contribute to the valence band, while the Ti/Zr d-orbitals mainly influence the conduction band. This differentiation underscores the critical role these elements play in determining the electronic properties of the alloy. Furthermore, the PDOS reveals how varying the concentration of Zr modifies the distribution of these states, thus allowing for fine-tuning of the electronic properties. For instance, increasing Zr concentration leads to an increase in the band gap, as reflected in the TDOS and PDOS curves, indicating the material's transition towards a wider band gap semiconductor. This tunability is crucial for optimizing the material for specific applications, such as enhancing thermoelectric performance or adjusting optical properties for use in electronic and optoelectronic devices. The careful analysis of TDOS and PDOS thus provides a deeper understanding of how

atomic-scale modifications impact the macroscopic electronic behavior of $Zr_xTi_{1-x}IrSb$ alloys.

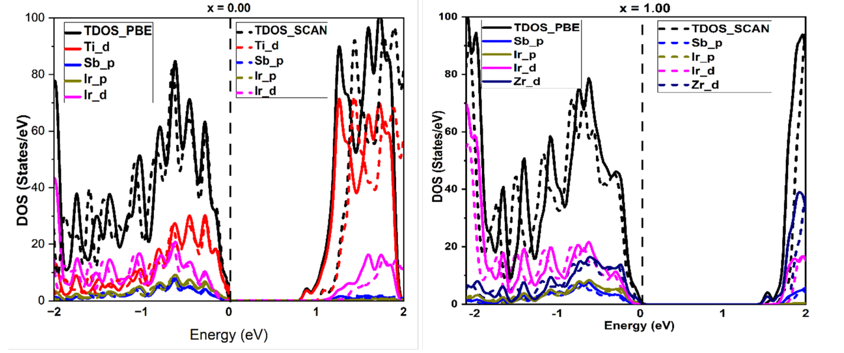

Figure III.25: Total and partial density of states for $Zr_xTi_{1-x}IrSb$ alloys at x= 0, 1, calculated using PBE and SCAN functional.

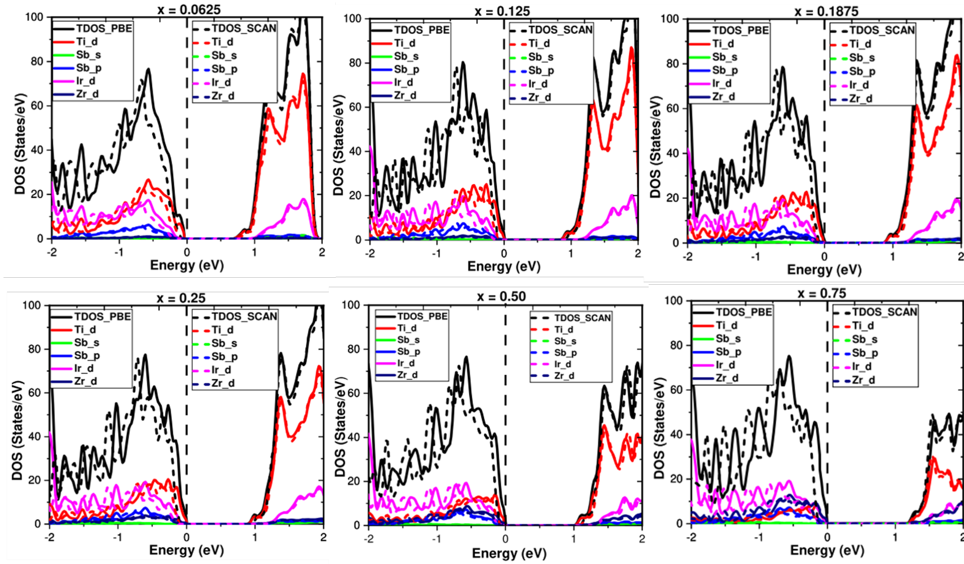

Figure III.26: Total and partial density of states for $Zr_xTi_{1-x}IrSb$ alloys at x= 0.0625, 0.125, 0.1875, 0.25, 0.50, 0.75, calculated using PBE and SCAN functionals.

In this section, we also analyzed the effective masses of electrons and holes in $Zr_xTi_{1-x}IrSb$ alloys at various compositions (x) using both PBE and SCAN functionals. Effective mass is a critical parameter that influences the carrier mobility and overall electronic performance of semiconductor materials. The Fig.III.27 shows the variation of effective masses (in units of the free electron mass m_0 as a function of composition (x) for PBE and SCAN, respectively. These quantities are determined using the following equation:

$$\frac{1}{m^*} = \frac{1}{\hbar^2} \frac{\partial^2 E}{\partial k_i \partial k_j} \tag{III.3}$$

where m^* represents the effective mass, $\hbar$ is the reduced Planck constant ($\hbar = h/2\pi$), and E is the electron energy. The effective mass provides insights into the carrier mobility within the crystal[4].

The effective mass is a key parameter influencing carrier mobility (lower effective mass indicates higher carrier mobility) . For electrons, the blue columns representing m_e^* in the $\Gamma \rightarrow L$ direction are consistently lower than the red columns $\Gamma \rightarrow X$, suggesting higher electron mobility in the $\Gamma \rightarrow L$ direction across most compositions. An exception is observed at x=0.0625, where the electron effective mass in the $\Gamma \rightarrow X$ direction is lower, indicating enhanced mobility in this direction for this specific concentration. Conversely, the cyan columns (m_h^* in $\Gamma \rightarrow L$) are significantly higher than the green columns ($\Gamma \rightarrow X$) for holes, implying lower hole mobility in the $\Gamma \rightarrow L$ direction. Notably, at x = 0.75, there is a marked increase in the effective mass for both electrons and holes, indicating a decrease in carrier mobility. This composition-dependent variation in effective mass is crucial for tailoring the electronic properties of $Zr_xTi_{1-x}IrSb$ alloys for specific applications. For instance, the pristine structure Zr_1Ti_0IrSb (x=1) demonstrates lower effective masses and thus higher mobilities compared to Zr_0Ti_1IrSb (x=0), particularly for electrons in the $\Gamma \rightarrow L$ direction. Understanding these effective mass trends allows for strategic modifications in alloy composition to optimize performance in electronic and optoelectronic devices, ensuring the desired balance between electron and hole mobilities for efficient operation.

Comparing the functionals, the SCAN functional's tendency to predict higher effective masses compared to PBE underscores the importance of the chosen exchange-correlation functional in computational studies. SCAN's more accurate treatment of electron correlations may provide a better representation of the material's behavior, though it predicts less favorable mobility characteristics.

III.2.7 Optical Properties

In this section, we analyze the optical properties of $Zr_xTi_{1-x}IrSb$ compounds, focusing on key parameters such as the extinction coefficient $k(\omega)$, reflectivity (R), refractive index $\eta(\omega)$,energy loss function $L(\omega)$, and absorption coefficient (α). These properties are critical for understanding the interaction of these materials with electromagnetic radiation, and their behavior provides insight into potential applications in optoelectronic devices. Using the Meta-GGA SCAN functional, we calculated the optical properties of

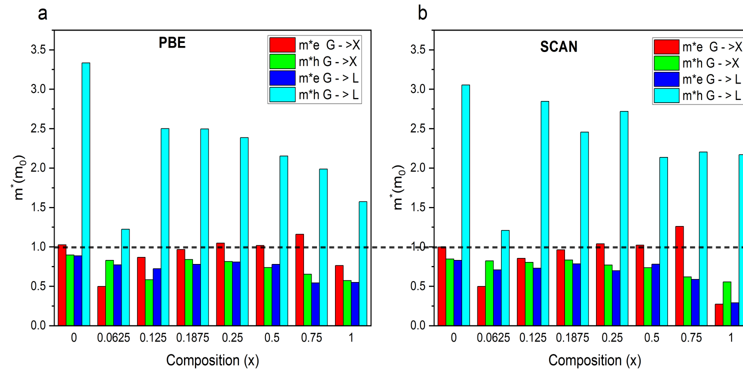

Figure III.27: Variations effective mass $m^*(m_0)$ of electrons and holes in gamma-x and gamma-L direction for $Zr_xTi_{1-x}IrSb$ alloys.

$Zr_xTi_{1-x}IrSb$ alloys, examining their behavior across different frequencies and compositions.

The real $\varepsilon_1(\omega)$ and imaginary $\varepsilon_2(\omega)$ components of the dielectric function, shown in Fig.III.28.a and Fig.III.28.b respectively, provide fundamental insights into the optical properties of $Zr_xTi_{1-x}IrSb$ alloys. The real part $\varepsilon_1(\omega)$ signifies the material's ability to polarize in response to an external electric field, impacting how light propagates through the material by altering its phase velocity, while the imaginary part $\varepsilon_2(\omega)$ represents the absorption losses due to electronic transitions between the valence and conduction bands [137, 142–145]. At 0 eV, all compositions (x) in $Zr_xTi_{1-x}IrSb$ exhibit significant dielectric values, with $Zr_{0.50}Ti_{0.50}IrSb$ having the lowest real part value and $Zr_{1.00}Ti_{0.00}IrSb$ the highest. This difference is also evident in the visible light range (1.7 to 3.3 eV), where peaks in the imaginary part indicate strong optical absorption due to electronic transitions between the valence band maximum (VBM) and conduction band minimum (CBM), particularly involving the d-states of Ti and Zr atoms.The extinction coefficient $k(\omega)$, depicted in Fig.III.28.c, is directly linked to the imaginary part of the dielectric function, quantifying the loss of light intensity due to scattering and absorption as it travels through the material. The equation k=$\frac{\sqrt{\varepsilon_2}}{2}$ shows this relationship. High peaks in $k(\omega)$ around ˜1.7 eV correspond to significant absorption, indicating that the material strongly interacts with light at lower photon energies. These observations are reinforced by the absorption coefficient (α), defined by:

$$\alpha = \frac{4\pi k}{\lambda} \tag{III.4}$$

where λ is the wavelength of light. This correlation between k and α underlines how the material's composition influences its ability to absorb light, making Zr concentration a key

factor in tuning these properties for applications like photovoltaics and photodetectors. The reflectivity index results (R), depicted in Fig.III.28.d, measures the proportion of light reflected by the material's surface, which is affected by both the real (n) and imaginary (k) components of the refractive index. The relationship can be expressed as:

$$R = \left(\frac{(n-1)^2 + k^2}{(n+1)^2 + k^2} \right) \tag{III.5}$$

This equation demonstrates the interdependence of n, k, and R. At zero photon energy, reflectivity values range from 0.51 to 1.07, varying with Zr content. Higher Zr concentrations "$Zr_{1.00}Ti_{0.00}IrSb$" result in higher n and k, indicating more light is reflected, which correlates with increased polarizability and electronic density of states. Conversely, $Zr_{0.50}Ti_{0.50}IrSb$ shows lower reflectivity, indicating increased light transmission. This variation with Zr content allows for the customization of optical properties for specific needs, such as designing anti-reflective coatings. The refractive index $\eta(\omega)$ presented in Fig..III.28.e, is a fundamental optical parameter that describes how light propagates through a material. It is defined as :

$$\eta(\omega) = \sqrt{\frac{\varepsilon_1 + \sqrt{\varepsilon_1^2 + \varepsilon_2^2}}{2}} \tag{III.6}$$

In these alloys, refractive index values range between 2.45 and 4 eV, depending on Zr content. This suggests that varying the Zr concentration allows control over light propagation characteristics, which is valuable for optical devices like lenses and waveguides that require precise control over light paths. The minimum refractive index is observed for $Zr_{0.50}Ti_{0.50}IrSb$, while the maximum is observed for $Zr_{1.00}Ti_{0.00}IrSb$. This variation demonstrates that the refractive index can be tuned by altering the Zr content, which is crucial for applications requiring precise control of light propagation, such as in lenses and waveguides. The energy loss function ($L(\omega)$), shown in Fig.III.28.f, reveals where energy loss due to inelastic electron scattering is most significant. Sharp peaks in the energy loss spectra are observed at 7.89 eV, 9.56 eV, 10.18 eV, 10.50 eV, 10.74 eV, 10.80 eV, and 19.93 eV for compositions with 0.50, 0.25, 0.1875, 0.125, 0.0625, 0.00, and 1.00 Zr content, respectively. For x=0.75, multiple peaks are noted between 11.36 eV and 14.56 eV. These peaks indicate significant energy loss at these energies, corresponding to plasmon excitations and inter-band transitions. The presence of multiple peaks for

x=0.75 suggests complex interactions within the material at this concentration, making it potentially useful for applications in plasmonic devices and sensors. Another parameter called the absorption coefficient, shown in Fig.III.29, provides insights into how well these alloys absorb light across different wavelengths. The absorption spectrum shows high absorption for visible light, with peaks in the green light region (˜2.4 to ˜2.7 eV) for concentrations $0 \leq x \leq 0.50$, while for higher concentrations, the peak shifts towards the violet light region. This shift indicates that by adjusting the Zr concentration, the alloys' light absorption properties can be tailored for specific wavelengths, which is beneficial for photovoltaic cells and photodetectors. Among the studied alloys, $Zr_{0.50}Ti_{0.50}IrSb$ exhibits the least light absorption, making it suitable for applications where lower optical absorption is desired.

Overall, the interrelated analysis of extinction coefficient, reflectivity, refractive index, energy loss function, and absorption coefficient underscores the significant impact of Zr concentration on the optical properties of $Zr_xTi_{1-x}IrSb$alloys. These findings demonstrate the tunability of optical characteristics, making these alloys promising candidates for a range of optoelectronic applications. The variations in these properties with Zr content emphasize the importance of compositional adjustments in optimizing these materials for specific technological uses.

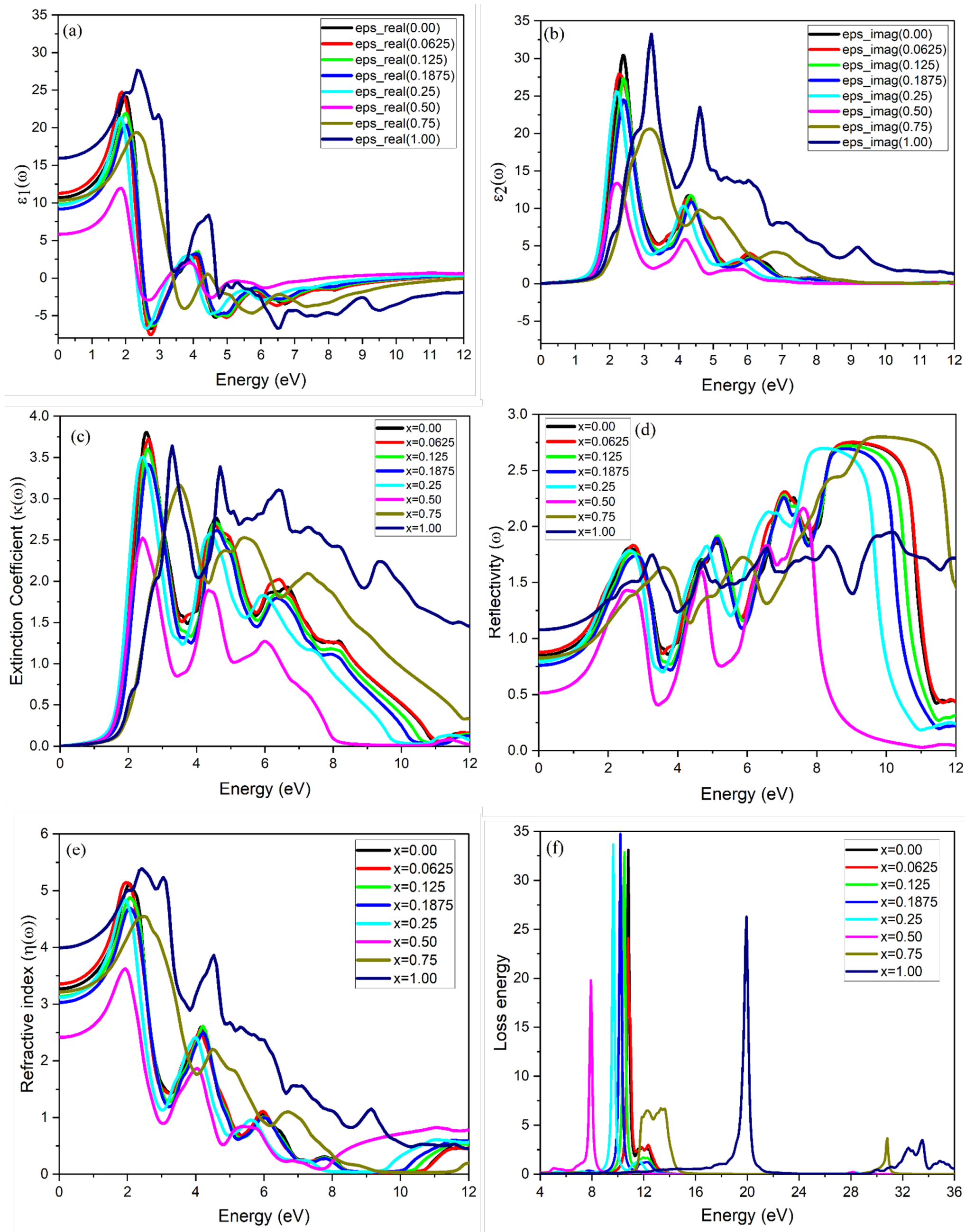

Figure III.28: Calculated optical coefficients: (a) Real part $\varepsilon_1(\omega)$ and (b) imaginary part $\varepsilon_2(\omega)$ of the dielectric function. (c) Extinction coefficient . (d) Reflectivity index. (e) Refractive index. (f) Loss energy for each concentration (x).

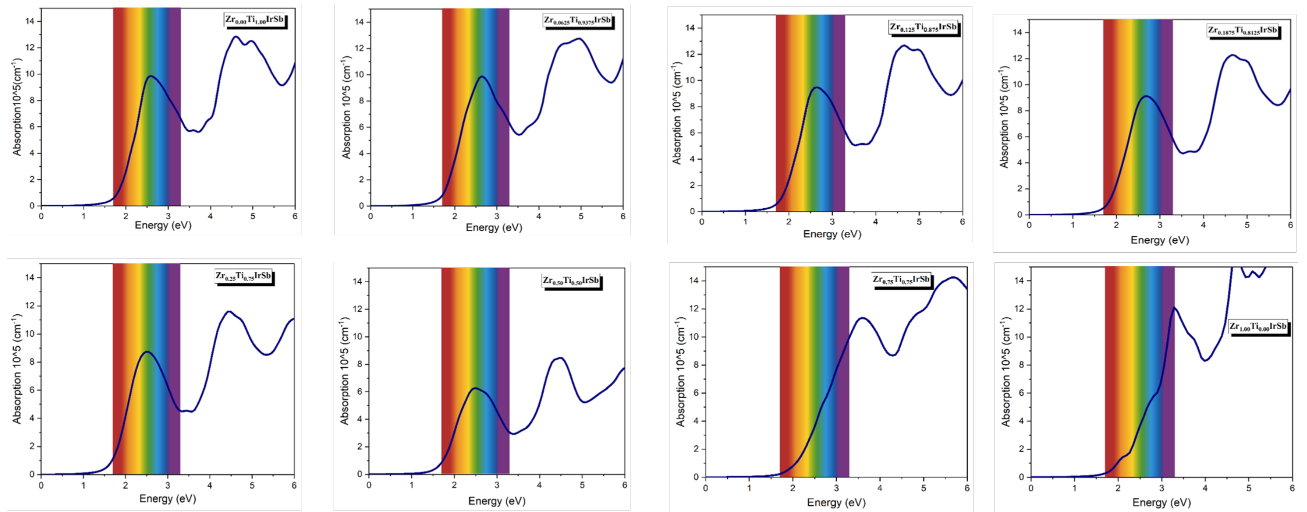

Figure III.29: Absorption coefficient of $Zr_xTi_{1-x}IrSb$ alloys as a function of concentration (x) using SCAN approach.

III.2.8 Conclusion

In this study, we systematically investigated the electronic, dynamic, and optical properties of $Zr_xTi_{1-x}IrSb$ half-Heusler alloys using first-principles calculations within the density functional theory (DFT) framework, employing the SCAN and PBE-GGA exchange-correlation functionals. Our comprehensive analysis began with the structural properties, confirming that the $Zr_xTi_{1-x}IrSb$ alloys crystallize in a cubic MgAgAs-type structure with 18 valence electrons per unit cell. The calculated lattice constants, bulk moduli, and elastic constants showed excellent agreement with previous theoretical predictions, underscoring the reliability of our computational approach. The mechanical stability of these alloys was validated through the fulfillment of Born's stability criteria, indicating robust structural integrity. Furthermore, the alloys exhibit ductile behavior as suggested by Pugh's ratio (B/G), which is advantageous for applications requiring mechanical flexibility and resilience.

Our exploration of the electronic properties revealed that both ternary compounds (x=0 and x=1) exhibit semiconducting behavior with a wide band gap, which increases with the concentration of Zr. This tunability of the band gap through variation in the Zr/Ti ratio highlights the potential of these alloys for various electronic applications, offering the possibility to design materials with specific electronic characteristics. Notably, the SCAN functional provided a more accurate description of the band gap compared to the PBE-GGA approximation, suggesting that SCAN may be a superior choice for future studies of similar materials.

The optical properties of the $ZrxTi_{1-x}IrSb$ alloys also exhibited significant variation with composition. Our analysis showed that these materials exhibit high absorption in the visible light range, making them promising candidates for optoelectronic applications. The ability to tune the dielectric function, extinction coefficient, reflectivity, refractive index, energy loss, and absorption coefficient by adjusting the Zr/Ti ratio further enhances their applicability in advanced optoelectronic devices. This tunability is crucial for the development of materials that can meet specific optical requirements, providing a pathway for the creation of highly efficient optoelectronic components.

Phonon dispersion calculations were conducted to assess the dynamic stability of the $Zr_xTi_{1-x}IrSb$ alloys across all concentrations. The results confirmed that these materials are dynamically stable, indicating that they can maintain their structural integrity under various conditions. This stability is a critical factor for their practical application in a wide range of technological fields, ensuring that the materials can withstand the demands of real-world usage without degradation.

Overall, our comprehensive computational analysis underscores the versatility and potential of $Zr_xTi_{1-x}IrSb$ half-Heusler alloys in electronic and optoelectronic applications. By precisely controlling the Zr/Ti ratio, the electronic, optical, and dynamical properties of these alloys can be finely tuned, opening new avenues for designing materials with specific characteristics tailored to advanced technological applications. Our study highlights the efficacy of using advanced computational techniques to predict and optimize the properties of complex materials, paving the way for future research aimed at developing next-generation materials with enhanced performance and functionality.

III.3 Vacancies and Antisite Point Defects Impact Study in the TiIrSb Structure

III.3.1 Introduction

Point defects are among the most fundamental structural imperfections that occur at the atomic level within crystalline lattices. These defects include vacancies and antisite disorders[4, 48], which profoundly influence the structural, electronic, optical, thermal, and mechanical properties of materials. Their presence is therefore of particular significance in the investigation of advanced alloys with functional and electronic applications[59].

In the present work, focused on TiIrSb Half-Heusler alloys, the examination of vacancies and antisite defects plays a crucial role, as these imperfections can modify the electronic structure, tune the band gap, and affect both the mechanical stability and bonding characteristics of the compound. Such defects may also induce a local redistribution of the electronic charge density, leading to the appearance of defect-induced states within the band gap. Understanding these phenomena is essential for explaining the material's behavior under realistic conditions[9, 11, 29, 42].

To comprehensively evaluate the influence of these point defects, a theoretical framework based on density functional theory (DFT)[75] was employed. Supercells containing specific vacancy or antisite configurations were modeled, and their thermodynamic stability was assessed through the calculation of formation energies. The corresponding electronic and optical properties were also analyzed. This approach provides valuable insights into the correlation between microstructure and physical properties in TiIrSb, thereby contributing to the design of optimized materials for thermoelectric and energy-related applications[28, 146].

III.3.2 Calculation details

In this section, we present the computational procedure adopted to investigate vacancy and antisite defects in the Half-Heusler TiIrSb compound using density functional theory (DFT). All calculations were performed with the Vienna *ab initio* Simulation Package (VASP) employing the projector augmented wave (PAW) method. The Perdew–Burke–Ernzerhof (PBE) functional within the generalized gradient approximation (GGA) was used to de-

scribe the exchange–correlation interactions. A plane-wave energy cutoff of 390 eV was applied throughout all calculations. The Brillouin zone was sampled using a Monkhorst–Pack k-point mesh of $3 \times 3 \times 5$ for structural optimization and a denser grid of $4 \times 4 \times 8$ for electronic structure calculations.

The supercell approach was adopted to model neutral defects. A $2 \times 2 \times 1$ supercell containing 48 atoms was generated from the relaxed conventional TiIrSb cell using the VASPKIT tool. Point defects were then introduced by either removing or substituting atoms within the supercell. For vacancy defects, a single atom was removed from the supercell, yielding three configurations corresponding to V_{Ti}, V_{Ir}, and V_{Sb}, where the subscript denotes the removed atom.

For antisite defects, one atom was replaced by another atom of the same structure, resulting in six possible configurations: Ti_{Ir}, Ir_{Ti}, Ti_{Sb}, Sb_{Ti}, Ir_{Sb}, and Sb_{Ir}. In this notation, the subscript represents the site of the atom that was replaced, while the symbol preceding it denotes the substituting atom.

III.3.3 Effect of Defects on the Crystal Structure

Understanding the influence of structural defects in crystalline materials is fundamental to elucidating their stability and related physical properties. In this context, analyzing relative distortions and variations in crystal density provides valuable insights into how the lattice responds to different types of defects, including vacancies and antisite disorders (see Table III.5).

Compared with the ideal (pristine) structure, the introduction of a vacancy generally results in a slight contraction of the lattice parameters. This behavior occurs because the absence of an atom at its equilibrium position allows neighboring atoms to relax inward to minimize the system's internal energy. The effect is more pronounced when using the SCAN functional than with PBE, as SCAN more accurately captures electronic interactions, leading to shorter interatomic distances and a denser crystal framework. Comparison of the calculated densities shows that vacancies tend to increase the overall mass density, particularly for the titanium vacancy case. The removal of a lighter atom (Ti) is compensated by the inward relaxation of heavier neighboring atoms, which enhances atomic packing.

Antisite defects, on the other hand, induce more complex structural responses. These defects create asymmetric lattice distortions that depend strongly on the chemical nature

and atomic radii of the exchanged atoms. For instance, substituting a Ti atom with Sb causes a slight lattice expansion due to the larger atomic size of Sb, whereas replacing an Ir atom with Ti leads to a minor contraction. This diversity in structural response confirms that both the magnitude and direction of distortion are governed primarily by atomic size mismatch and bonding characteristics.

A comparison between the PBE and SCAN functionals further highlights essential differences in describing these structural changes. SCAN generally provides a more realistic representation of chemical bonding, particularly in systems containing transition metals such as Ir. Consequently, SCAN predicts smaller lattice parameters and higher densities, indicating a more compact and energetically favorable crystal structure.

Overall, these findings demonstrate that the influence of defects in Half-Heusler alloys extends beyond local atomic distortions, inducing global modifications across the entire crystal lattice. Such structural rearrangements significantly affect the material's physical properties, including electronic behavior, mechanical resilience, and thermal transport. Therefore, establishing a clear correlation between structural deformation and functional properties is crucial for a comprehensive understanding of defect-driven behavior in these systems.

In conclusion, this study emphasizes the importance of selecting an appropriate exchange–correlation functional. SCAN has proven to outperform PBE in describing defect-induced lattice distortions, making it a preferable choice for future investigations of defect physics in Half-Heusler alloys.

Table III.5: Relative distortions (%) and density (g/cm^3) for the pristine and defective structures using PBE and SCAN functionals, with volume change (%) relative to the pristine structure.

Defect Type	Functional	a (%)	b (%)	c (%)	Density (g/cm^3)	Volume (%)
			Pristine Structure (TiIrSb)			
—	PBE	12.334	12.334	6.166	**10.249**	—
—	SCAN	12.328	12.328	6.164	**10.261**	—
			Vacancy Defects			
V_{Ti}	PBE	12.317 (-0.13)	12.317 (-0.13)	6.165 (-0.02)	10.233	-0.28
V_{Ti}	SCAN	12.139 (-1.52)	12.139 (-1.52)	6.083 (-1.30)	10.634	-4.28
V_{Ir}	PBE	12.285 (-0.40)	12.285 (-0.40)	6.141 (-0.41)	10.027	-1.19
V_{Ir}	SCAN	12.114 (-1.73)	12.114 (-1.73)	6.055 (-1.76)	10.457	-5.08
V_{Sb}	PBE	12.295 (-0.31)	12.295 (-0.31)	6.151 (-0.24)	10.162	-0.86
V_{Sb}	SCAN	12.118 (-1.70)	12.118 (-1.70)	6.072 (-1.49)	10.554	-4.82
			Anti-site Defects			
Ti_{Ir}	PBE	12.316 (-0.15)	12.316 (-0.15)	6.156 (-0.16)	10.552	-0.44
Ti_{Ir}	SCAN	12.159 (-1.37)	12.159 (-1.37)	6.078 (-1.40)	10.966	-4.15
Ti_{Sb}	PBE	12.356 (0.23)	12.356 (0.23)	6.173 (0.11)	10.329	+0.59
Ti_{Sb}	SCAN	12.002 (-2.64)	12.002 (-2.64)	6.096 (-1.10)	10.731	-7.73
Ir_{Sb}	PBE	12.429 (0.77)	12.429 (0.77)	6.181 (0.24)	9.945	+1.99
Ir_{Sb}	SCAN	12.273 (-0.45)	12.273 (-0.45)	6.105 (-0.96)	10.328	-1.20
Ir_{Ti}	PBE	12.350 (0.13)	12.350 (0.13)	6.172 (0.10)	9.958	+0.36
Ir_{Ti}	SCAN	12.202 (-1.02)	12.202 (-1.02)	6.097 (-1.09)	10.326	-3.03
Sb_{Ti}	PBE	12.306 (-0.23)	12.306 (-0.23)	6.153 (-0.21)	10.186	-0.66
Sb_{Ti}	SCAN	12.154 (-1.41)	12.154 (-1.41)	6.078 (-1.39)	10.571	-4.14
Sb_{Ir}	PBE	12.296 (-0.31)	12.296 (-0.31)	6.149 (-0.28)	10.467	-0.91
Sb_{Ir}	SCAN	12.140 (-1.53)	12.140 (-1.53)	6.072 (-1.49)	10.878	-4.87

III.3.4 Energies and Stability Analysis

To investigate the influence of vacancies and antisite defects on the structural and physical properties of the bulk primitive $TiIrSb$ compound under different growth conditions, we calculated the chemical potential boundaries using the binary phases $TiIr$, $TiIr_2$, $TiSb_2$, and Sb_2Ir. These boundaries were employed to determine the thermodynamic formation region of the $TiIrSb$ compound. The compound is stable when the following condition is

satisfied:

$$\mu_{Ti} + \mu_{Ir} + \mu_{Sb} = \Delta H_{TiIrSb} = -2.35 \text{ eV} \tag{III.7}$$

To prevent the formation of competing binary phases, the following stability limits were imposed:

$$\mu_{Ti} + \mu_{Ir} \leq \Delta H_{TiIr} = -1.66 \text{ eV} \tag{III.8}$$

$$\mu_{Ti} + 2\mu_{Ir} \leq \Delta H_{TiIr_2} = -2.20 \text{ eV} \tag{III.9}$$

$$\mu_{Ti} + 2\mu_{Sb} \leq \Delta H_{TiSb_2} = -1.67 \text{ eV} \tag{III.10}$$

$$2\mu_{Sb} + \mu_{Ir} \leq \Delta H_{Sb_2Ir} = -1.11 \text{ eV} \tag{III.11}$$

Using Eq. III.7, inequalities III.10 and III.11 can be rewritten as:

$$\mu_{Ir} + 2\mu_{Ti} \geq -3.59 \text{ eV}, \quad \mu_{Ti} + 2\mu_{Ir} \geq -3.03 \text{ eV} \tag{III.12}$$

From these inequalities, the stability diagram shown in Fig. III.30 was obtained. The gray region represents the thermodynamically stable range of the compound. Any deviation beyond this boundary indicates a loss of stability, leading to decomposition into more stable binary phases under the corresponding chemical potential conditions.

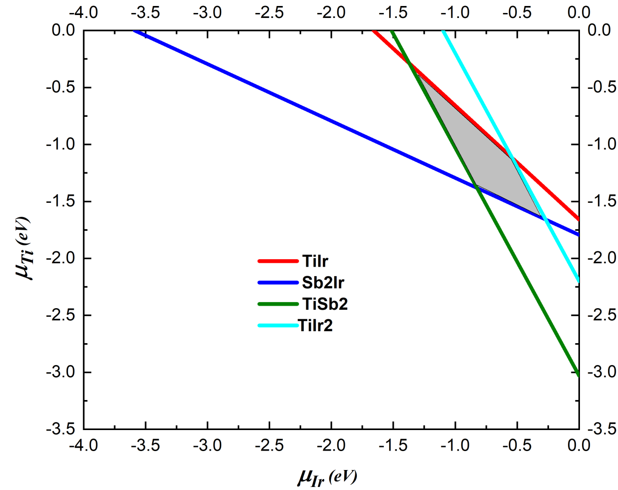

Figure III.30: Thermodynamic stability region of the ternary TiIrSb compound. The gray region represents the stability range where the TiIrSb phase is formed, using the GGA-PBE functional.

Figure III.31 illustrates the variation in the formation energy of neutral point defects in a $2 \times 2 \times 1$ supercell of TiIrSb as a function of the chemical potentials of its constituent elements. For vacancies, the chemical potential varies from element-rich to element-poor conditions, allowing an evaluation of how chemical environments affect defect formation stability.

A decrease in the formation energies of titanium, iridium, and antimony vacancies was observed. However, all values remain positive, indicating that these defects are thermodynamically unfavorable and do not form spontaneously. The positive formation energies confirm that defect creation requires external energy input, thus verifying that the pristine structure corresponds to the most stable configuration.

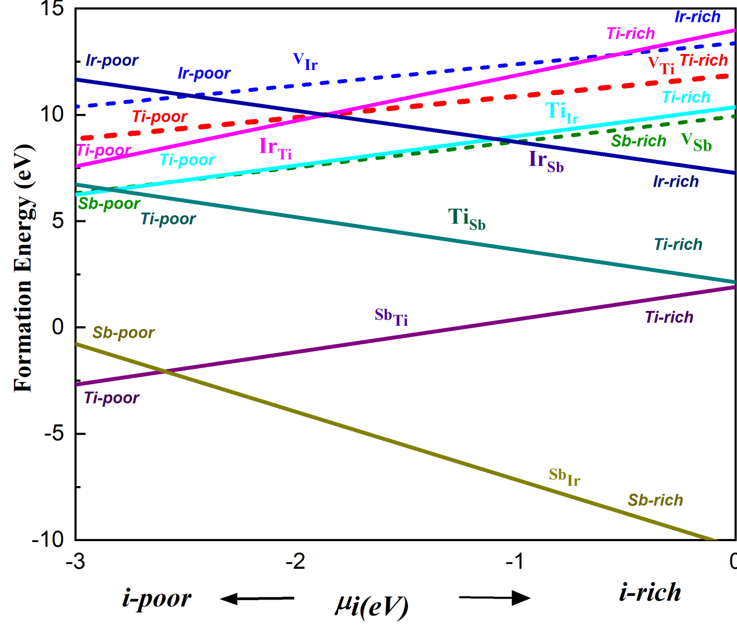

Figure III.31: Formation energy of neutral point defects (vacancies and antisites) as a function of chemical potential variation between rich and poor regions for element i. Here, i represents the removed element in the case of vacancy defects, and the substituted element in the case of antisite defects, using the GGA-PBE functional.

For antisite point defects, notable differences are observed among the six possible substitutions. The formation energies of Ir_{Sb} and Ti_{Sb} antisite defects decrease within the positive region of the curve as the system transitions from Ti- and Ir-poor to Ti- and Ir-rich conditions. This trend indicates that these defects are more likely to form under Ti-rich conditions, where the formation energy is lower, while their formation is less favorable in Ti-deficient environments.

In contrast, the Sb_{Ir} antisite defect exhibits a decreasing formation energy when moving from Sb-poor to Sb-rich conditions, suggesting that it may form spontaneously under Sb-rich growth. The marked reduction in formation energy could also indicate a potential tendency toward partial phase decomposition in these conditions. For Sb_{Ti}, the formation energy changes from negative to positive as the system transitions from Sb-poor to Sb-rich, implying that defect formation becomes less favorable and requires additional energy in Sb-rich regions. Finally, the Ir_{Ti} antisite defect shows an increasing formation energy toward the Sb-rich side, confirming that its formation is energetically less favorable.

III.3.5 Effects of Vacancies on Electronic Properties

Atomic vacancies play a crucial role in tailoring the electronic and magnetic behavior of Half-Heusler compounds. By altering the hybridization between neighboring atoms, they can induce notable modifications in the band structure and density of states (DOS), thereby influencing the overall electronic performance of the material. In this section, the effects of Ti, Ir, and Sb vacancies on the electronic structure of TiIrSb are analyzed, with emphasis on variations in the energy gap, spin symmetry, and the nature of states near the Fermi level.

Ti vacancy: The removal of a Ti atom slightly narrows the energy gap without introducing pronounced defect states within the band gap. This behavior results primarily from the weakened hybridization between Ti and Ir orbitals, which slightly modifies the DOS near the Fermi level. The electronic structure remains largely symmetric between the Spin-Up and Spin-Down channels, as no significant spin polarization is observed. The calculated total magnetic moment ($\mu = 0.0000\,\mu_B$) confirms that the Ti vacancy does not induce magnetism in the system. However, the slight reduction in the energy gap may enhance electrical conductivity due to decreased orbital overlap.

Ir vacancy: Iridium, being a heavy element, plays an essential role in the hybridization network of TiIrSb. When an Ir atom is removed, no new states emerge within the band gap, indicating that the structure rearranges electronically to preserve its semiconducting character. The DOS around the Fermi level remains nearly zero, confirming the insulating nature of the material at zero temperature. Similar to the Ti vacancy, both spin channels remain degenerate, and the total magnetic moment ($\mu = 0.0000\,\mu_B$) suggests that the Ir vacancy does not promote magnetic polarization.

Sb vacancy: In contrast, removing an Sb atom leads to a significant alteration in the electronic structure. The absence of Sb breaks several Ti–Sb covalent bonds, producing unsaturated (dangling) states that give rise to additional energy levels within the band gap. A distinct spin splitting between the Spin-Up and Spin-Down channels is observed, where one channel exhibits a finite DOS at the Fermi level while the other maintains an energy gap. This asymmetry indicates a transition from semiconducting to half-metallic behavior, making this configuration promising for spintronic applications.

Furthermore, the Sb vacancy induces a noticeable local magnetic moment of $\mu = 0.9767\,\mu_B$, revealing an imbalance in the spin population between the two channels. This magnetization arises from the asymmetric hybridization of Ti and Ir d-orbitals, which

enhances spin polarization around the vacancy site. The detailed impact of these defects on the overall magnetic properties will be discussed in the following section.

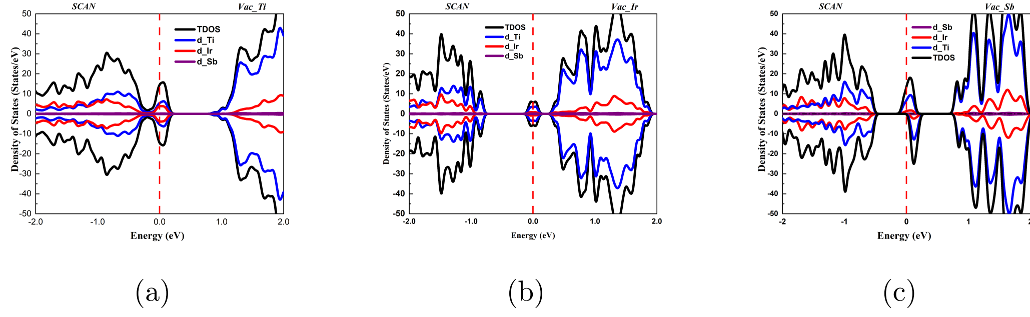

(a) (b) (c)

Figure III.32: Total and Partial Density of States for TiIrSb 2×2×1 Supercell with Vacancy Defects: (a) for V_{Ti}, (b) for V_{Ir} and (c) V_{Sb}, using SCAN functional.

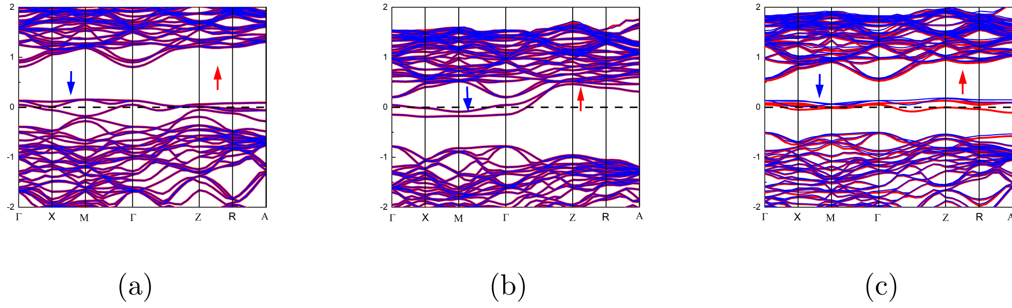

(a) (b) (c)

Figure III.33: Band Structure for TiIrSb 2×2×1 Supercell with Vacancy Defects: (a) for V_{Ti}, (b) for V_{Ir} and (c) V_{Sb}, using SCAN functional.

III.3.6 Effects of Antisite Point Defects on Electronic Properties

In this study, the electronic band structure resulting from the introduction of antisite defects in TiIrSb is analyzed, where six types of substitutions are studied, focusing on the effect of each on the Fermi level, the energy gap, and the emergence of new levels within the band gap. By analyzing the results, some of these states can be classified as contributing to n-type or p-type behavior, and it is possible to understand how these defects affect the electronic and conductivity properties.

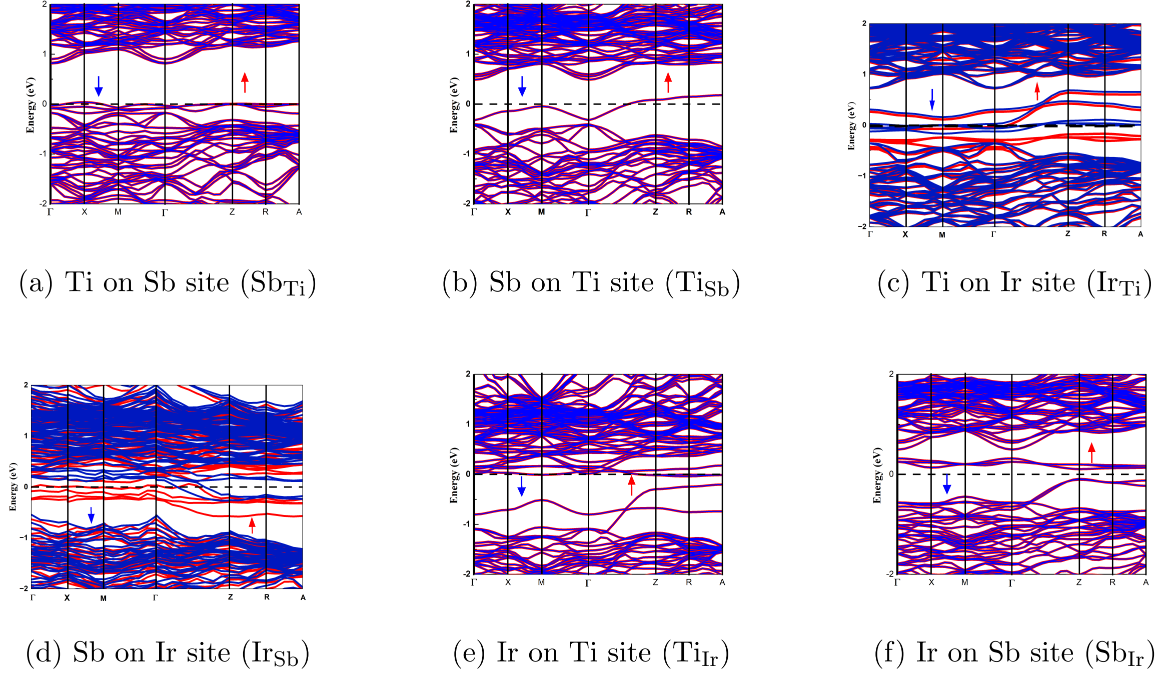

(a) Ti on Sb site (Sb_{Ti}) (b) Sb on Ti site (Ti_{Sb}) (c) Ti on Ir site (Ir_{Ti})

(d) Sb on Ir site (Ir_{Sb}) (e) Ir on Ti site (Ti_{Ir}) (f) Ir on Sb site (Sb_{Ir})

Figure III.34: Electronic band structures for the six studied antisite defects in TiIrSb. Each plot shows the influence of antisite substitution on the band gap and electronic states.

- **Antisite exchange between Ti and Sb:** Sb_{Ti} **versus** Ti_{Sb} By exchanging Ti and Sb in TiIrSb, two antisite defects can be formed, namely the X-on-A antisite Sb_{Ti} and its reverse A-on-X counterpart Ti_{Sb}. Although both defects preserve the local fourfold coordination, their thermodynamic stability and electronic character are markedly different.

  For Sb_{Ti} (X-on-A), the band structure and density of states reveal a localized defect band just above the valence-band maximum and a pronounced DOS peak at the Fermi level, indicating an acceptor-like defect that generates p-type carriers. This behaviour follows the general doping rule established for 18-electron half-Heusler compounds with a 5d element on the B site, where X-on-A antisites are the dominant intrinsic acceptors responsible for p-type self-doping.[125]

  In contrast, the reverse antisite Ti_{Sb} (A-on-X) produces a partially occupied defect band crossing the Fermi level inside the band gap, while the conduction band remains relatively distant. Although this defect is electronically active, its higher formation energy makes its equilibrium concentration much lower than that of Sb_{Ti}(see Fig.III.31), so it plays only a secondary role and does not determine the intrinsic p-type character of TiIrSb.

- **Antisite exchange between Ti and Ir ($\mathbf{Ti_{Ir}}$ / $\mathbf{Ir_{Ti}}$)**

  For the antisite configuration where Ti occupies the Ir site (Ir_{Ti}), the conduction-band minimum is strongly lowered towards the Fermi level and defect-related Ir/Ti-d states appear very close to E_F (Figures. III.34c and III.35c). This provides low-energy electronic states that can be thermally ionized into the conduction band, so that Ir_{Ti} behaves as a donor-like defect and drives TiIrSb towards electron-rich n-type conduction under suitable growth conditions.[125]

  In the reciprocal configuration, where Ir occupies the Ti site (Ti_{Ir}), a nearly flat defect band is formed inside the fundamental gap and is pinned around the Fermi level, with most of its spectral weight located between the valence-band maximum and E_F (Figures III.34e and III.35e). The proximity of this band to the valence-band edge indicates that the Ti_{Ir} antisite primarily behaves as a valence-band-related defect capable of capturing electrons and creating holes near the valence-band maximum, thus favouring p-type behaviour, although its slight crossing of E_F suggests that both electrons and holes can, in principle, participate in transport.

  Overall, antisite exchange between Ti and Ir introduces donor-like Ir_{Ti} centres and hole-producing Ti_{Ir} defects, so that the intrinsic electronic response of TiIrSb reflects a competition between electron-rich n-type and hole-favouring p-type regimes. A more detailed analysis of the associated spin polarization and magnetic moments is presented in subsection III.3.7, where the effect of these defects on the magnetic and electronic properties is discussed.

- **Replacing Ir with Sb atom (Ir_{Sb})**

  In this configuration, the conduction-band edge is strongly pulled towards the Fermi level and locally crosses E_F, while a much narrower gap than in pristine TiIrSb still separates the main valence and conduction manifolds. The finite DOS at the Fermi level, mainly originating from Ti- and Ir-d states, indicates a quasi-metallic (degenerate) electron-rich behaviour, so this defect drives the system towards n-type conductivity with partially occupied conduction states.

- **Replacing Sb with Ir atom (Sb_{Ir})**

  In this case, defect-induced electronic levels appear inside the band gap, leaving a very small residual gap of about 0.20 eV, so that the system remains in a narrow-gap

semiconducting state. Since several of these in-gap states lie just above the Fermi level, they behave predominantly as empty acceptor-like levels that can capture electrons, and under the conditions considered here this defect tends to promote p-type behaviour.

Defects that lower the conduction-band edge or introduce occupied in-gap states push the system towards n-type conductivity, whereas those that raise the valence-band edge or create empty states close to the Fermi level favour p-type behaviour[122]. Some antisite configurations exhibit both donor-like and acceptor-like levels, making their effective character dependent on external conditions such as pressure, temperature, and doping; overall, point defects in TiIrSb induce a rich variety of electronic responses, ranging from electron-rich n-type to hole-favouring p-type regimes.

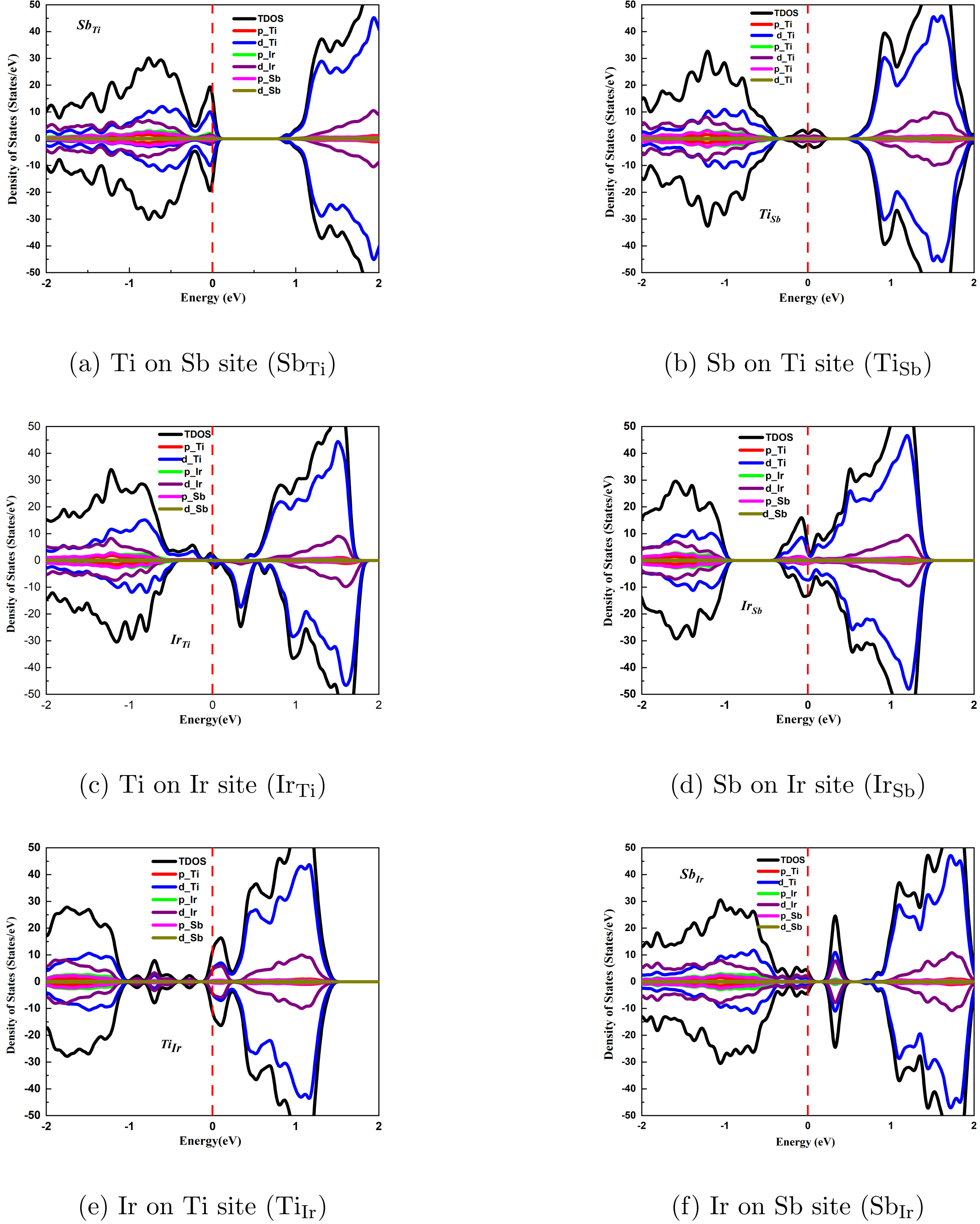

(a) Ti on Sb site (Sb_{Ti})

(b) Sb on Ti site (Ti_{Sb})

(c) Ti on Ir site (Ir_{Ti})

(d) Sb on Ir site (Ir_{Sb})

(e) Ir on Ti site (Ti_{Ir})

(f) Ir on Sb site (Sb_{Ir})

Figure III.35: Electronic Density of States (DOS) for antisite defects in TiIrSb, ordered according to the sequence used in the band structure analysis.

Density of States (DOS) analysis is an important tool for detecting fundamental changes in the electronic structure resulting from the introduction of anti-sits defects in the TiIrSb crystal structure. This analysis helps in understanding how each defect affects the distribution of electronic states across the valence and conduction bands, and enables the identification of new levels within the energy gap (Gap States) and their proximity or overlap with the Fermi level. In addition, spin-resolved DOS analysis allows

the detection of any local magnetic polarization that may arise due to the presence of some defects, providing accurate information about the possibility of symmetry breaking between the spin-up and spin-down channels.

In general, all studied cases, both in the ideal structure (pristine) and with substitution defects, showed that the d orbitals of the titanium atom (Ti-d) represent the main contribution to both the valence band and the conduction band, followed closely by the contribution of the d orbitals of the iridium atom (Ir-d). This result confirms the transition-metal-like nature of the electronic structure, where the overlap between the d orbitals dominates the conduction behavior, while the antimony (Sb) orbitals contribute to the deeper levels of the valence band, without a significant contribution to the conduction levels.

With the introduction of different substitutional defects, in most cases, new levels within the energy gap (defect states) were observed, the locations of which vary depending on the type and location of the defect. In some cases, such as the substitution of Ti by Sb, levels very close to the Fermi level appeared, indicating the formation of acceptor-like states, which enhances p-type behavior. In contrast, when Sb was substituted by Ir, high defect levels appeared that intersect the Fermi level, reflecting the possibility of donor-like states, which enhances n-type behavior. This diversity in locations and occupancy levels reflects the sensitive effect of each type of defect on the electronic levels close to the Fermi level, which is one of the main factors in determining the type of charge carriers.

When analyzing the density of spin-resolved electronic states (DOS), most of the studied cases showed symmetry between the spin-up and spin-down components, reflecting the absence of obvious magnetic moments in these cases, and confirming the general non-magnetic nature of the system. However, in the cases of Ir substitution by Ti atom (Ir_{Ti}) and Ir substitution by Sb atom (Ir_{Sb}), a clear asymmetry was observed between the two spin channels, where the density of states for one channel appeared higher than the other, indicating the emergence of local spin polarization at the defect sites in these two cases. This behavior is attributed to the inhomogeneous nature of the orbital overlap resulting from the large variation in the chemical nature between the substituted atoms, which leads to a specific spin preference in the local defect levels.

Although spin asymmetry in the DOS appears in some cases, the calculated electronic band structure for these states shows exactly identical energy levels between the two spin-degenerate bands. This apparent discrepancy is explained by the localized nature of the

defect-induced spin polarization, which appears in the DOS analysis because it depends on the localized projection onto the atomic orbitals, while the electronic structure represents the delocalized Bloch states that include the effect of the crystal as a whole, and thus may show identical levels when the local magnetic moment is weak or when the symmetry is broken very slightly.

Overall, the DOS analysis shows that the different substitutional (antisite) defects in TiIrSb not only affect the band gap width and Fermi level position, but also the spin symmetry in some cases. This diversity of effects reflects the high sensitivity of the electronic structure of this compound to structural disturbances, making control of the nature of the defects (their type, concentration, and fabrication method) an effective means of tuning the electronic properties according to the desired applications. Some defects show a clear tendency to drive the system towards n-type (electron-rich defects) or p-type (electron-poor defects) behavior, while others exhibit transition states that depend on environmental conditions and defect concentration.

III.3.7 The effect of defects on magnetic and electronic properties

The study of the effect of structural defects, such as antisite defects and vacancies, on the electronic and magnetic properties of half-Heusler compounds is of fundamental importance in understanding the behavior of these materials and their potential for use in advanced technological applications. In TiIrSb, a narrow-gap semiconductor, structural defects can lead to substantial changes in the density of states (DOS) and the electronic structure (band structure), which are directly reflected in the local magnetic properties of the system.

The calculation results indicate that some anti-defects and vacancies in TiIrSb give rise to a local magnetic moment, while others remain non-magnetic. For example Ir_{Ti} and Ir_{Sb} defects exhibit magnetic moments of $\mu = 4.5651\,\mu_B$ and $\mu = 0.8322\,\mu_B$ respectively, while the vacancy V_{Ti} exhibited a magnetic moment of $\mu = 0.9767\,\mu_B$, In contrast, other defects such as $\mathrm{Sb_{Ti}}$, $\mathrm{Ti_{Sb}}$, $\mathrm{Ti_{Ir}}$ and $\mathrm{Sb_{Ir}}$ Non-magnetic ($\mu = 0.0000\,\mu_B$)

The magnetism recorded in some defects is due to local distortions in the electronic configuration, especially in the d orbitals of the transition elements. Substitutional disturbance changes the coordination environment of the atoms surrounding the defect, cre-

ating an imbalance between the spin-up and spin-down channels, and resulting in partial or complete spin polarization in the electronic states close to the Fermi level.

In the case of Ir_{Ti} , replacing the Ti(3d) atom with an Ir(5d) atom increases the number of local valence electrons, which increases the density of states near the Fermi level. Due to the difference in local symmetry, a large spin split occurs in the electronic structure, so that most of the electrons occupy a spin of a certain direction (Spin-up or Spin-down), which leads to the emergence of a relatively high magnetic moment ($\mu = 4.8771\,\mu_B$).

Removal of the Sb atom leaves a local electron gap that leads to a redistribution of charge between neighboring atoms, especially Ti and Ir. This increases the probability of unpaired electrons in the regions near the vacancy, creating a magnetic moment ($\mu = 0.9767\,\mu_B$ accompanied by asymmetric spin peaks in the DOS.

Absence of magnetism in Ti_{Sb} and Ti_{Ir}. In these cases, the Ti (3d) atom replaces another element (Ir or Sb), which leads to a rearrangement of the valence orbitals in a way that maintains spin symmetry (spin balance), where all orbitals remain either filled or empty equally for both spin channels, ensuring zero magnetic moment.

Defects that replace Sb do not cause spin polarization Since Sb is a group 5 p-element with relatively full valence orbitals, its replacement by other elements such as Ti or Ir does not create spin-asymmetric levels, keeping the material non-magnetic. This behavior is seen in the cases of Sb_{Ti} and Sb_{Ir}.

Table III.6: Magnetic moments and electronic impact of vacancies and antisite defects in TiIrSb.

Defect	Magnetic Moment (μ_B)	Comment
	Vacancies	
Vac_{Ti}	0.00	No magnetic states.
Vac_{Ir}	0.00	No magnetic states.
Vac_{Sb}	**0.9767**	**Localized states cause spin polarization.**
	Antisite Defects	
Sb_{Ti}	0.00	No magnetic effect.
Ti_{Sb}	0.00	No magnetic effect.
Ir_{Ti}	**4.5651**	**Strong spin splitting.**
Ir_{Sb}	**0.8322**	**Moderate spin polarization.**
Ti_{Ir}	0.00	No magnetic effect.
Sb_{Ir}	0.00	No magnetic effect.

The magnetic properties of TiIrSb are a direct manifestation of the influence of anti-defects and vacancies on the local electronic structure. Defects that create spin-

unbalanced electronic states produce local magnetic moments that can transform the compound from a non-magnetic to a locally or globally magnetic material. This deep connection between electronic structure and magnetic properties makes it possible to carefully design the properties of materials by controlling the type and density of defects, opening up vast prospects for applications in the fields of spintronics and advanced magnetic sensors.

III.3.8 Impact of Vacancies and Anti-site Defects on Optical Properties

When comparing the optical properties of the pristine TiIrSb structure with those of the vacancy-containing configurations, clear distinctions are observed in both the real and imaginary parts of the dielectric function (Figure III.36(a) and (b)).

In the real part, the pristine structure exhibits low values that gradually increase at low photon energies before slowly decreasing with increasing energy. In contrast, the vacancy-containing systems show an initial decline below 1 eV, followed by a noticeable rise up to around 2 eV, and then a sharp drop at higher energies. These variations reflect the influence of vacancies in modifying the material's polarizability due to the structural disorder they introduce.

For the imaginary part, which represents the optical absorption, the defective structures display pronounced peaks at low energies (0–2 eV) that are absent in the pristine compound. This behavior indicates that the introduction of vacancies generates new electronic transitions within this energy range, originating from defect-induced levels inside the band gap. Furthermore, the vacancy-containing systems exhibit stronger absorption peaks between 2 and 4 eV compared to the pristine one, highlighting the enhanced density of available electronic states due to defect-induced perturbations.

At higher photon energies, the real part of the dielectric function for the defective systems decreases more sharply than that of the pristine structure and may even reach negative values, revealing the strong influence of structural symmetry breaking on the optical response.

Overall, these findings demonstrate that introducing vacancies not only alters the electronic structure but also induces a substantial modification of the optical behavior. Consequently, vacancy engineering emerges as an effective strategy for tuning the optical

response of TiIrSb-based materials to meet the requirements of various optoelectronic and photonic applications.

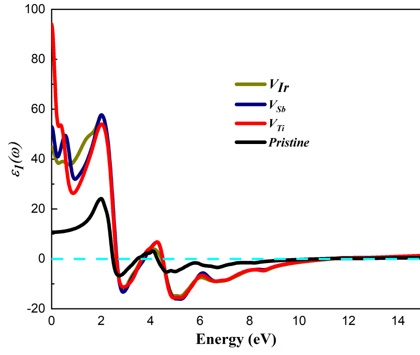

(a) Real part of the dielectric function $\varepsilon_1(\omega)$

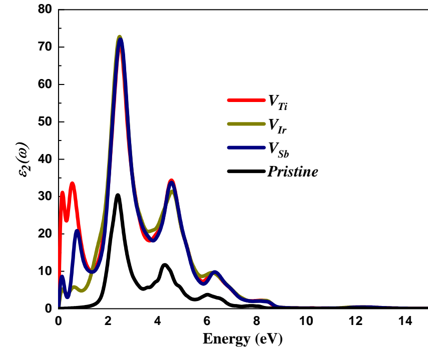

(b) Imaginary part of the dielectric function $\varepsilon_2(\omega)$

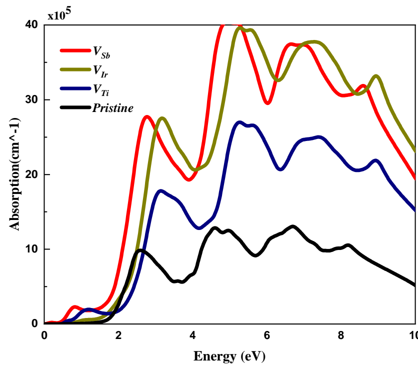

(c) Absorption coefficient $\alpha(\omega)$

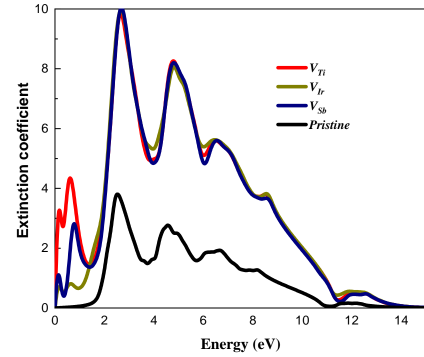

(d) Extinction coefficient $k(\omega)$

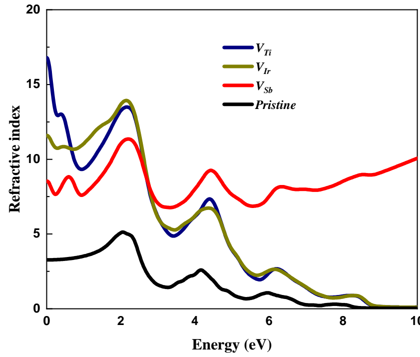

(e) Refractive index $n(\omega)$

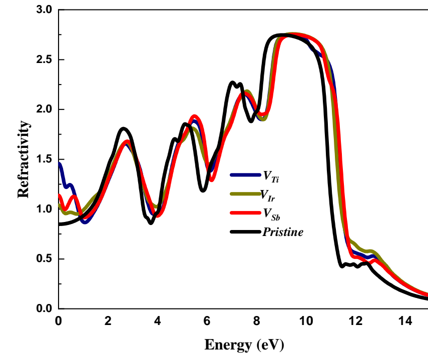

(f) Reflectivity

Figure III.36: The optical properties of TiIrSb with and without a vacancy defect, including: (a) Real part of the dielectric function, (b) Imaginary part of the dielectric function, (c) Absorption coefficient, (d) Extinction coefficient, (e) Refractive index, and (f) Refractivity.

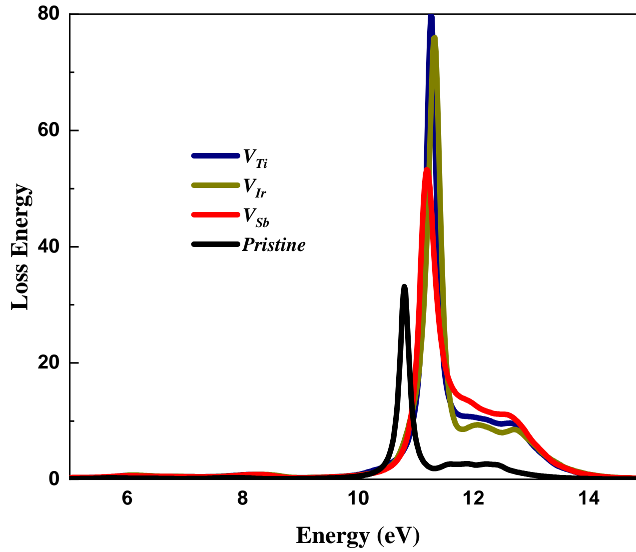

Figure III.37: The variation of the Loss energy as a function of photon energy for the perfect and defective structures (vacancies defects).

The optical absorption coefficient serves as a key parameter for analyzing the response of a material to incident light across a broad range of photon energies. When comparing the absorption behavior of the pristine TiIrSb structure with that of vacancy-containing configurations, distinct variations are observed, clearly reflecting the influence of structural defects on the optical response.

At low photon energies (0–2 eV), the pristine structure exhibits very weak absorption, consistent with the presence of a well-defined energy gap that suppresses optical transitions in this range—an expected feature of semiconducting materials with a relatively wide band gap.

In contrast, the vacancy-containing systems display small but noticeable absorption peaks within the same energy interval. These features originate from defect-induced energy levels that emerge within the band gap, enabling additional electronic transitions. As a result, the material can absorb light at photon energies lower than the intrinsic band gap, effectively narrowing the optical band gap and enhancing its interaction with low-energy radiation.

In the middle-energy range (2–4 eV), all configurations (ideal and vacancy-containing) exhibit pronounced absorption peaks. However, the peaks corresponding to the vacancy-containing structures are noticeably higher than those of the ideal phase. This enhancement indicates an increased density of electronic states in this energy re-

gion, originating from the structural disorder induced by the vacancy, which consequently enhances the probability of optical transitions within this range.

At higher energies (above 5 eV), all systems display a marked rise in absorbance with increasing photon energy. This behavior is typically attributed to electronic transitions from deep valence bands to higher conduction bands. Nevertheless, the vacancy-containing states maintain higher absorption intensities than the ideal structure, reflecting the cumulative effect of vacancies in altering the electronic structure and enhancing the overlap between electronic states.

The extinction coefficient represents the material's ability to absorb light and is directly related to the imaginary part of the dielectric function. In the ideal structure, it remains weak at low photon energies due to the presence of a band gap. However, the introduction of vacancies gives rise to additional peaks in the low-energy region and a noticeable enhancement of the peaks between 2 and 4 eV. At higher energies, the absorption continues to increase, reflecting the influence of defects on the electronic structure.

The refractive index of the defective structures exhibits a considerable increase with more pronounced peaks compared to the ideal structure, particularly in the low- and medium-energy regions. This behavior reflects the impact of vacancies on modifying the local electronic environment and increasing the density of available electronic states for optical transitions. Such changes enhance the interaction between light and matter, leading to a greater capacity of the material to slow down and propagate light waves. Therefore, the presence of vacancies makes the alloy more optically active, with a clear influence across different energy ranges.

The energy-loss function displays distinct peaks within the 10–12 eV range for all studied configurations, with sharper features observed in the defective structures compared to the ideal one. This behavior reveals the strong impact of vacancies on collective electronic excitations, as structural defects promote charge redistribution and increase the density of electronic states in this energy region, confirming that the optical response is directly affected by the presence of vacancies.

Although the introduction of vacancies slightly influences the reflectivity, the results indicate no significant differences between the ideal and defective structures across most of the investigated energy range. The overall optical response remains similar, with only minor variations, particularly at low photon energies where weak vacancy-induced effects appear. In the visible range, the ideal structure exhibits a higher reflectivity peak com-

pared to the defective configurations, suggesting that the presence of vacancies slightly reduces the material's ability to reflect light. This observation confirms that the influence of vacancies on reflectivity is limited, especially within the visible wavelength region.

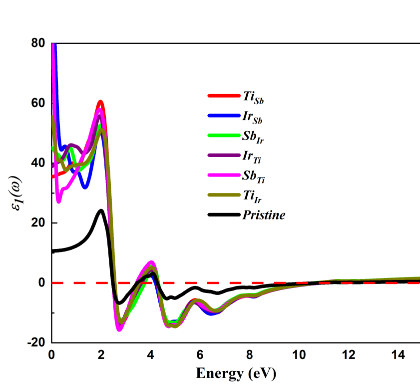

(a) Real part of the dielectric function.

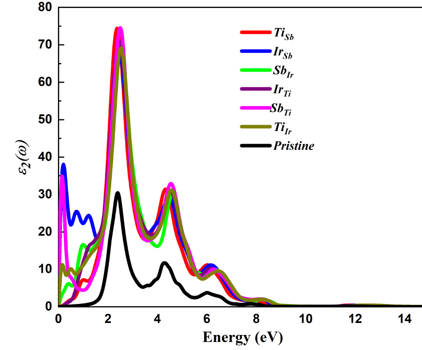

(b) Imaginary part of the dielectric function.

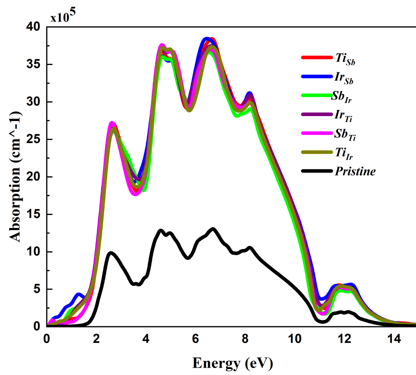

(c) Absorption coefficient.

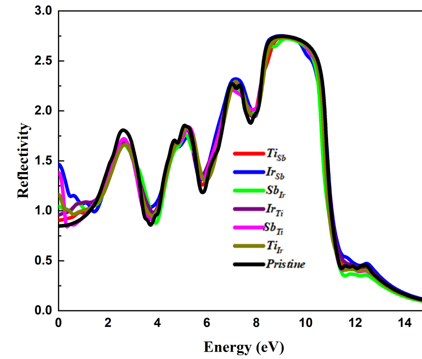

(d) Reflectivity.

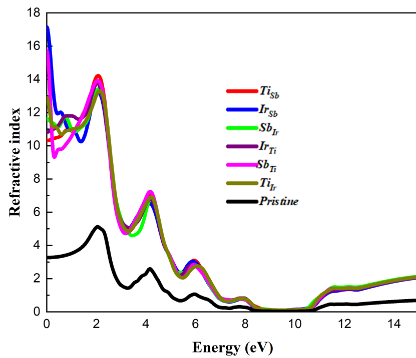

(e) Refractive index.

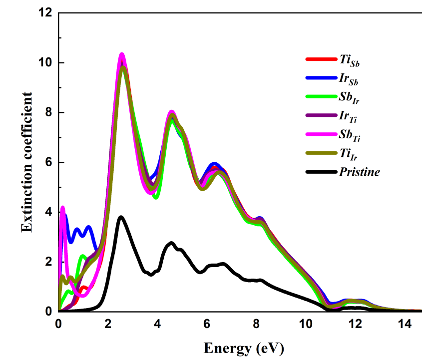

(f) Extinction coefficient.

Figure III.38: Optical properties of the system with anti-site defects.

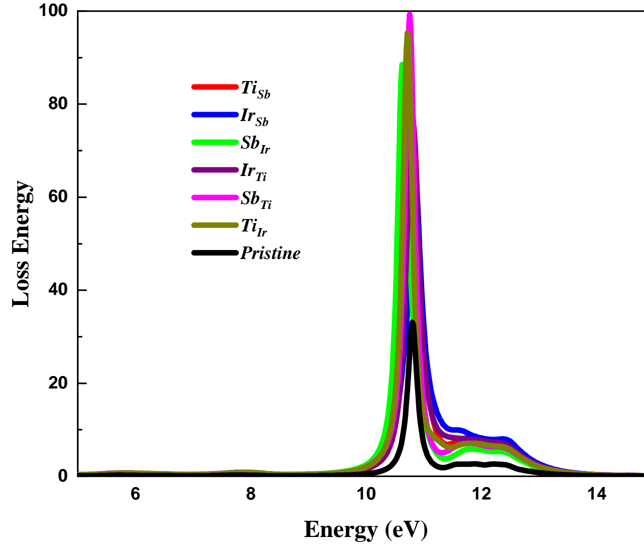

Figure III.39: The variation of the Loss energy as a function of photon energy for the perfect and defective structures (antisite defects).

The optical results obtained for the anti-site defects reveal a clear influence of these imperfections on the material's response to electromagnetic waves across the investigated spectrum. This behavior reflects the impact of structural disorder caused by replacing original atoms with others occupying non-native lattice sites. Such effects are evident through the overall increase in most optical coefficients compared to the ideal structure, a trend also observed in the case of vacancies.

For the real part of the dielectric function (ε_1), the anti-site defects exhibit higher values than the ideal configuration, indicating enhanced electronic polarization resulting from local symmetry breaking and the appearance of additional contributions from new electronic transitions. Similarly, the imaginary part (ε_2) shows a noticeable enhancement, particularly at low and medium photon energies, suggesting the emergence of extra optical transitions between the defect-induced localized states and the intrinsic energy bands.

Regarding the optical absorption coefficient, a significant increase is observed across all studied energy ranges relative to the ideal structure. This confirms that the presence of anti-site defects facilitates additional electronic transitions that require lower photon energies compared to the pristine case. Such behavior aligns with theoretical expectations that structural defects introduce localized energy levels acting as intermediate transition bridges between the valence and conduction bands.

In terms of reflectivity, the anti-site defects display higher values than the ideal struc-

ture, with the reflectivity curve rising at lower photon energies. This trend indicates an increased density of free carriers near the surface, attributed to the presence of defect-induced states. Likewise, both the refractive index and the extinction coefficient show a marked increase, emphasizing the stronger light–matter interaction in the defected structures.

The energy loss function exhibits sharper peaks at specific energies compared to the ideal case, reflecting a higher probability of energy loss as electromagnetic waves propagate through anti-site–containing structures. This behavior highlights the enhanced electronic scattering and the increased degree of structural disorder caused by the defects.

When comparing the optical spectra of anti-site defects and vacancy-containing configurations, it is evident that the ideal structure consistently exhibits the lowest values across all optical parameters. This confirms that the introduction of any type of point defect (vacancy or anti-site) leads to a degradation of the pristine optical performance.

III.3.9 Conclusion

In this chapter, the influence of vacancies and antisite defects on the structural, electronic, and optical properties of the TiIrSb Half-Heusler alloy was systematically investigated using density functional theory (DFT) within the supercell framework. The analysis focused on evaluating the crystal stability by calculating the total energies and monitoring the variations in lattice constants upon the introduction of point defects, providing a detailed comparison between the pristine and defective configurations.

The thermodynamic stability analysis revealed that defect formation in most cases requires additional energy, confirming that the ideal structure is generally more stable. However, the antisite defect Sb_{Ir} represents a notable exception, exhibiting a negative formation energy that indicates enhanced structural stability compared to the perfect compound.

From the electronic perspective, band structure and density of states (DOS) calculations demonstrated that defects significantly modify the electronic band gap. Certain vacancies and antisite configurations either reduce the gap or introduce defect-induced states within it, directly affecting the electronic transitions and the semiconductor behavior of the alloy.

Regarding the optical response, the complex dielectric function was computed to derive key optical constants such as the absorption coefficient, refractive index, and reflectivity.

The obtained results revealed that the introduction of point defects alters the spectral absorption range and modifies energy transfer through the material, as evidenced by a noticeable shift in the absorption edge induced by changes in the electronic structure.

Overall, this study confirms that point defects in TiIrSb are not merely local perturbations but act as critical factors governing the electronic and optical performance of the alloy. These findings open promising perspectives for tailoring the physical properties of Half-Heusler compounds through controlled defect engineering, particularly for electronic, optical, and thermoelectric applications.

Summary and conclusion

In this thesis, a comprehensive study of the physical properties of the TiIrSb, ZrIrSb, TaIrSn, and TaIrGe Half-Heusler compounds, as well as an analysis of the effect of structural defects in TiIrSb, was conducted using density functional theory (DFT). The study focused on evaluating the structural, electronic, optical, and thermoelectric properties, taking into account the possibility of tuning these properties by controlling the structural composition and introducing point defects.

Physical Properties of the ABX Half-Heusler compounds

The results showed that all four Half-Heusler exhibit structural and mechanical stability, as verified by elasticity constant C_{ij} calculations and fulfillment of the Born stability conditions. The study of the electronic band structure and density of states (DOS) revealed that all compounds exhibit semiconductor behavior with suitable energy gaps, enhancing their potential for electronic applications.

Regarding optical properties, the studied compounds exhibited a strong optical response in the visual field and ultraviolet range, making them candidates for solar cell and optoelectronic applications. Thermoelectric calculations using BoltzTraP2 also showed that these compounds possess high Seebeck coefficient (S) and electrical conductivity σ/τ, with variations in thermoelectronic conductivity κ_e, suggesting the potential for improving their thermoelectric performance through appropriate structural modifications.

Study of alloys and the effect of their composition on physical properties

In addition to the pure compounds, the effect of zirconium and titanium alloying in $Zr_xT_{1-x}IrSb$ alloys was studied. The results revealed that these alloys retain the cubic crystal structure of the MgAgAs type with 18 valence electrons per unit cell. The alloys also demonstrated remarkable mechanical stability, with their crystalline structure being verified by meeting the Born criteria and calculating the Pugh ratio (B/G), confirming their high elasticity and ability to withstand mechanical stresses.

Electronically, the alloys exhibited semiconductor behavior with the ability to tune

the energy gap by varying the zirconium/titanium ratio. The high zirconium concentration contributes to widening the energy gap, opening the way for the design of materials with tunable electronic properties. The optical properties of these alloys also demonstrated significant control over absorption, refractive index, and reflectivity, making them candidates for advanced optoelectronic applications.

In terms of dynamic stability, phonon scattering calculations confirmed that these alloys are stable across all concentrations, demonstrating their ability to maintain their structural integrity under various operating conditions, a key factor in industrial applications. The Effect of Point Defects on TiIrSb Compound

The effect of vacancies and antisite defects on TiIrSb was studied. The results showed that these defects lead to fundamental changes in the structural, electronic, and optical properties. At the structural level, calculations showed that the introduction of defects results in a slight change in the lattice constants and overall energy, reflecting the material's ability to adapt to structural disturbances without losing its overall stability.

Electronically, the study of the band structure and density of states (DOS) revealed that point defects lead to a shrinkage of the energy gap or the introduction of additional energy levels within it, indicating a shift in the material's electronic behavior. In particular, the calculations showed that the antisite defect Sb_{Ir} is an exception, as its formation energy is negative, indicating a higher stability of this defect compared to the ideal structure.

In terms of optical properties, the calculations showed that defects affect the spectral absorption range and absorption edge, which could improve or reduce the material's efficiency in optical applications. This effect reflects the crucial role of point defects in tuning optical and electronic properties, which could be of great importance in the design of materials for photovoltaic applications.

Conclusions and Future Research Prospects

This study confirmed that the studied half-Heussler compounds possess outstanding electronic, optical, and mechanical properties, making them strong candidates for advanced technological applications. It also demonstrated that $Zr_xT_{1-x}IrSb$ alloys offer the possibility of tuning physical properties by controlling the chemical composition, paving the way for the design of multifunctional materials.

Regarding the effect of defects in TiIrSb, the results confirmed that vacancies and antisite defects are not merely local disturbances but directly affect the electronic and

optical structure, making them a powerful tool for tuning the material's response and improving its performance in practical applications. In particular, exploiting the antisite defect Sb_{Ir} can be used due to its high stability, which could be useful in improving the material's performance in advanced thermoelectric and electronic applications.

Future Research Prospects

This study opens new avenues for the design of improved-performance materials, particularly in the fields of electronics, solar cells, and thermoelectric materials. It also underscores the importance of DFT-based computer simulations as a powerful tool for predicting material properties and guiding research toward improving their performance. Future research proposals include:

- Studying the effect of high temperatures on defect stability in TiIrSb.
- Analyzing the effect of compound defects (the presence of more than one type of defect in the same material).
- Extending the study to other compounds with promising technological potential.

Bibliography

[1] Teng Fang, Xinbing Zhao, and Tiejun Zhu. Band structures and transport properties of high-performance half-heusler thermoelectric materials by first principles. *Materials*, 11(5), 2018.

[2] International Union of Pure and Applied Chemistry. Periodic table of the elements, 2021. Accessed: 2025-02-26.

[3] F. Heusler, W. Starck, and E. Haupt. Magnetisch-chemische studien. *Verhandlungen der Deutschen Physikalischen Gesellschaft*, 5:219–232, 1903.

[4] N. W. Ashcroft and N. D. Mermin. *Solid State Physics*. Holt, Rinehart and Winston, 1976.

[5] Engineering Stuff. Line defects - imperfections in crystals, 2024. Accessed: 2024-12-28.

[6] Moises Pineda. Planar defects and boundaries, 2010. Accessed: 2024-12-28.

[7] https://www.tf.uni kiel.de/matwis/amat/iss/index.html. Types of planar defects : (a) stacking faults, (b) phase boundarie., 2024. Accessed: 2024-12-28.

[8] Seema Morab, Manickam Minakshi, and Almantas Pivrikas. Review on charge carrier transport in inorganic and organic semiconductors. *Coatings*, 13:1657, 09 2023.

[9] Romain Gautier, Xiuwen Zhang, Linhua Hu, Liping Yu, Yuyuan Lin, Tor OL Sunde, Danbee Chon, Kenneth R Poeppelmeier, and Alex Zunger. Prediction and accelerated laboratory discovery of previously unknown 18-electron abx compounds. *Nature chemistry*, 7(4):308–316, 2015.

[10] Feng Yan, Xiuwen Zhang, Yonggang G. Yu, Liping Yu, Arpun Nagaraja, Thomas O. Mason, and Alex Zunger. Design and discovery of a novel half-Heusler transparent hole conductor made of all-metallic heavy elements. *Nature Communications*, 6(1):7308, June 2015.

[11] Mi Zhong, Wei Zeng, Fu-Sheng Liu, Bin Tang, and Qi-Jun Liu. Explanation for the conductivity difference of half-heusler transparent conductors via ionization energy. *Phys. Chem. Chem. Phys.*, 23:9285–9293, 2021.

[12] Kulwinder Kaur and Ranjan Kumar. Ti based half heusler compounds: A new on the screen with robustic thermoelectric performance. *Journal of Alloys and Compounds*, 727, 08 2017.

[13] Benallou Yassine, Kadda Amara, Bendouma Doumi, Omar Arbouche, Zemouli Mostefa, Belmorsli Bekki, and Allel Mokaddem. Structural stability, electronic structure and novel transport properties with high thermoelectric performances of zrirx (x = as, bi and sb). *Journal of Computational Electronics*, 16:0937, 11 2016.

[14] Djallal Eddine Mellah and Kamel Demmouche. Exchange-correlation and spin-orbit coupling effects in 18-electrons transparent conductors half-heusler: Ab-initio study. *Computational Condensed Matter*, 32:e00690, 2022.

[15] Mike Finnis. *Interatomic Forces in Condensed Matter*. Oxford University Press, 10 2003.

[16] J. Hafner. Ab-initio simulations of materials using vasp: Density-functional theory and beyond. *Journal of Computational Chemistry*, 21(1):29–40, 2000.

[17] J. Tobola, J. Pierre, S. Kaprzyk, and Others. Covalent bonding and the 18-electron rule in transition-metal-based half-heusler compounds. *Physical Review B*, 61:4694–4701, 2000.

[18] W. G. Zeier, A. Zevalkink, S. Gibbs, and other. Thinking like a chemist: Intuition in thermoelectric materials. *Angewandte Chemie International Edition*, 55:6826–6841, 2016.

[19] Wolfgang G. Zeier, Julian Schmitt, Geoffroy Hautier, Hangtian Zhu, Kazuki Imasato, Gregory Pomrehn, Saneyuki Ohno, Shashwat Anand, Umut Aydemir,

Zachary M. Gibbs, Claudia Felser, and G. Jeffrey Snyder. Engineering half-heusler thermoelectric materials using zintl chemistry. *Nature Reviews Materials*, 1(11):16032, 2016.

[20] C. Uher et al. X. Shi, L. Yang. On the design of thermoelectric materials via defect engineering: A case study of half-heuslers. *Energy Environmental Science*, 11:2225–2236, 2018.

[21] P. Rogl et al. G. Rogl, A. Grytsiv. Thermoelectric performance of half-heusler composites. *Journal of Electronic Materials*, 46:1506–1514, 2017.

[22] Thomas Graf, Claudia Felser, and Stuart S. P. Parkin. Simple rules for the understanding of heusler compounds. *Progress in Solid State Chemistry*, 39(1):1–50, 2011.

[23] Y. Liu et al. C. Fu, S. Bai. Realizing high figure of merit in half-heusler thermoelectrics. *Nature Communications*, 6:8144, 2015.

[24] J. Kübler, A. R. Williams, and C. B. Sommers. Formation and properties of heusler phases in materials. *Physical Review B*, 28:1745, 1983.

[25] A. J. Bradley and J. W. Rogers. The crystal structure of heusler alloys. *Proceedings of the Royal Society of London. Series A*, 144:340–359, 1934.

[26] S. Bhattacharya and G. K. H. Madsen. High-throughput exploration of alloying as design strategy for thermoelectric half-heusler compounds. *Physical Review B*, 92:085205, 2015.

[27] G. Joshi, H. Lee, Y. Lan, X. Zhang, G. S. Dyck, D. M. Tanaka, W. W. Wang, J. P. Fleurial, and Z. Ren. Enhanced thermoelectric figure-of-merit in nanostructured p-type half-heusler alloys. *Nano Letters*, 8(12):4670–4674, 2008.

[28] Guo-Xing Miao, Markus Münzenberg, and Jagadeesh S Moodera. Tunneling path toward spintronics. *Reports on Progress in Physics*, 74(3):036501, 2023. Accessed: Oct. 13, 2023.

[29] C. Felser, G. H. Fecher, and B. Balke. Spintronic materials and heusler compounds. *Angewandte Chemie International Edition*, 46:668, 2007.

[30] J. Pierre, R. V. Skolozdra, J. Tobola, S. Kaprzyk, C. Hordequin, M. A. Kouacou, I. Karla, R. Currat, and E. Lelievre-Berna. Magnetic and structural properties of heusler alloys. *Journal of Alloys and Compounds*, 262:101, 1997.

[31] J. H. Wernick, G. W. Hull, T. H. Geballe, J. E. Bernadini, and J. V. Waszczak. Superconducting properties of heusler alloys. *Materials Letters*, 2:90, 1983.

[32] J. Winterlik, G. H. Fecher, A. Thomas, and C. Felser. Superconducting properties in heusler phases. *Physical Review B*, 79:064508(1), 2009.

[33] M. Heusler. On the alloys of copper, manganese, and iron, with remarkable magnetic properties. *Naturwissenschaften*, 16:34–35, 1903.

[34] Sara J. Yahya, Mohammed S. Abu-Jafar, Said Al Azar, Ahmad A. Mousa, Rabah Khenata, Doha Abu-Baker, and Mahmoud Farout. The structural, electronic, magnetic and elastic properties of full-heusler co2cral and cr2mnsb: An ab initio study. *Crystals*, 12(11), 2022.

[35] K. Özdoğan and I. Galanakis. A study on the magnetic properties of inverse heusler compounds. *Journal of Magnetism and Magnetic Materials*, 321:L34–L37, 2009.

[36] Shruti Sharma and Dinesh C. Gupta. Systematic investigation of structural, magneto-electronic, mechanical, thermophysical, optical and thermoelectric properties of hf_2vz (z = ga, in, tl) inverse heusler alloy for spintronics applications. *Scientific Reports*, 14(1):28542, 2024.

[37] Yun liang Li, Yun liang Li, G. D. Liu, Xiaotian Wang, W. Q. Zhao, E. K. Liu, Xiaoli Xi, Wen-Qiong Wang, G. H. Wu, and Xuefang Dai. Electronic structures, magnetic properties and half-metallicity of heusler compounds hf2vz (z = ga, in, tl, si, ge, sn and pb): First-principle calculations. *Journal of Superconductivity and Novel Magnetism*, 31:3063 – 3074, 2018.

[38] Saadi Berri, Miloud Ibrir, Djamel Maouche, and Mourad Attallah. Robust half-metallic ferromagnet of quaternary heusler compounds zrcotiz(z = si, ge, ga and al). *Computational Condensed Matter*, 1:26–31, 2014.

[39] Y. C. Gao, Y. Zhang, and X. T. Wang. Phase stability, band gap, and electronic and magnetic properties of quaternary heusler alloys femnscz (z = al, ga, in). *Journal of the Korean Physical Society*, 66(6):959–965, 2015.

[40] Yue Wang, Xiaoming Zhang, Bei Ding, Zhipeng Hou, Enke Liu, Zhongyuan Liu, Xuekui Xi, Hongwei Zhang, Guangheng Wu, and Wenhong Wang. Magnetic semiconductors based on quaternary heusler compounds. *Computational Materials Science*, 150:321–324, 2018.

[41] Hirofumi Hazama, Masato Matsubara, Ryoji Asahi, and Tsunehiro Takeuchi. Improvement of thermoelectric properties for half-heusler tinisn by interstitial ni defects. *Journal of Applied Physics*, 110(6), 2011.

[42] Asma Wederni, Jason Daza, Wael Ben Mbarek, Joan Saurina, Lluisa Escoda, and Joan-Josep Suñol. Crystal structure and properties of heusler alloys: A comprehensive review. *Metals*, 14(6), 2024.

[43] A. Hirohata, M. Kikuchi, N. Tezuka, K. Inomata, J. S. Claydon, Y. B. Xu, and G. van der Laan. Heusler alloy/semiconductor hybrid structures. *Current Opinion in Solid State and Materials Science*, 10(2):93–107, 2006. Received 13 February 2006; accepted 15 November 2006.

[44] Sandip Bhattacharya and Georg KH Madsen. A novel p-type half-heusler from high-throughput transport and defect calculations. *Journal of Materials Chemistry C*, 4(47):11261–11268, 2016.

[45] I. Galanakis, K. Ozdogan, and E. Sasioglu. Role of defects and disorder in the half-metallic full-heusler compounds. *arXiv preprint arXiv:0709.4519*, 2007. Submitted on 26 Sep 2007 (v1), last revised 28 Sep 2007 (v2).

[46] Mohammed Hadbi, Kamel Demmouche, Djallal Eddine Mellah, and Jose Coutinho. Theoretical insights into off-stoichiometric zr(x)ti(1-x)irsb half-heusler alloys: a first principle calculations. *Journal of Physics: Condensed Matter*, 37(4):045702, nov 2024.

[47] Enamullah and Seung-Cheol Lee. High-efficient and defect tolerant co2mnsb ternary heusler alloy for spintronic application. *Journal of Alloys and Compounds*, 765:1055–1060, 2018.

[48] Charles Kittel. *Introduction to Solid State Physics*. Wiley, 8th edition, 2005.

[49] M. A. Green. Crystal defects and microstructures in semiconductor materials. *Materials Science and Engineering*, A282(1):1–10, 2000.

[50] Miller Elly Shatsala, Maxwell Mageto, George Manyali, and Mwamburi Mghendi. Thermodynamic stability of abx heavy elements of tairge, tiirsb, tairsn and zrirsb tcos using the half-heusler technique. *Energy Procedia*, 93:191–196, 2016. Africa-EU Renewable Energy Research and Innovation Symposium, RERIS 2016, 8-10 March 2016, Tlemcen, Algeria.

[51] Poulumi Dey and Biswanath Dutta. Decisive role of interstitial defects in half-heusler semiconductors: An ab initio study. *Phys. Rev. Mater.*, 5:035407, Mar 2021.

[52] Richard P. Feynman. The feynman lectures on physics, volume ii, chapter 38: Elasticity, 2024. Accessed: March 2, 2025.

[53] Mark Fox. *Optical Properties of Solids*. Oxford University Press, 2nd edition, 2010. Comprehensive textbook covering the optical properties of various solid materials, including semiconductors.

[54] Peter Y. Yu and Manuel Cardona. *Fundamentals of Semiconductors: Physics and Materials Properties*. Springer, 4th edition, 2010. Key reference for understanding optical processes in semiconductors, including absorption and reflectivity.

[55] Neha Singh, A.K. Gupta, and R.K. Singh. Electronic and optical properties of half-heusler compounds: A first principles study. *Physica B: Condensed Matter*, 543:45–51, 2018. Detailed DFT study on the optical properties (dielectric function, absorption, etc.) of half-Heusler compounds.

[56] P. Gorai, V. Stevanović, and E. S. Toberer. Computationally guided discovery of thermoelectric materials. *Nature Reviews Materials*, 4:416–432, 2019. Although focused on thermoelectrics, it covers important optical screening techniques for materials discovery.

[57] M. Rashid, M. A. Ali, S. Ahmad, A. Shakil, and S. A. A. Shah. Electronic structure and optical properties of new half-heusler compounds for optoelectronic applications. *Journal of Alloys and Compounds*, 818:152866, 2020. Focuses on the potential of new half-Heuslers for optoelectronic devices.

[58] Sanjeev Kumar and K. Tankeshwar. Optical properties of half-heusler alloy nimnsb:

Ab initio study. *Materials Science in Semiconductor Processing*, 25:94–99, 2014. First-principles study of the optical properties of a half-Heusler alloy.

[59] J. P. Heremans, M. S. Dresselhaus, L. E. Bell, and D. T. Morelli. When thermoelectrics reached the nanoscale. *Nature Nanotechnology*, 8(7):471–473, 2013. Discussion on nanoscale effects in thermoelectric performance enhancement.

[60] X. Shi, J. Yang, J. R. Salvador, M. F. Chi, J. Y. Cho, H. Wang, S. Bai, J. Yang, W. Zhang, and L. Chen. Multiple-filled skutterudites: High thermoelectric figure of merit through separately optimizing electrical and thermal transports. *Journal of the American Chemical Society*, 133(20):7837–7846, 2011. Focuses on optimizing thermal and electrical transport separately in thermoelectric materials.

[61] G. Slack. Thermal conductivity of pure and impure materials. In *Solid State Physics*, volume 34, pages 1–71. Academic Press, 1979. Foundational reference on thermal conductivity in materials science.

[62] J. Yang, H. Wang, X. Shi, S. Bai, L. Yang, W. Zhang, and L. Chen. Evaluation of half-heusler compounds as thermoelectric materials based on the calculated electrical transport properties. *Advanced Functional Materials*, 18(19):2880–2888, 2008. Detailed evaluation of half-Heusler compounds focusing on electrical transport properties.

[63] G. J. Snyder and E. S. Toberer. Complex thermoelectric materials. *Nature Materials*, 7(2):105–114, 2008. Key review on thermoelectric materials and their complexities.

[64] Jagdish Mehra. *The Conceptual Completion and Extensions of Quantum Mechanics 1932-1941. Epilogue: Aspects of the Further Development of Quantum Theory 1942-1999: Subject Index: Volumes 1 to 6*. Springer Science & Business Media, 2004.

[65] Carlos Fiolhais, Fátima Nogueira, and Miguel A. L. Marques, editors. *A Primer in Density Functional Theory*, volume 620 of *Lecture Notes in Physics*. Springer, 2003.

[66] E. Schrödinger. An undulatory theory of the mechanics of atoms and molecules. *Physical Review*, 28:1049, 1926.

[67] Attila Szabo and Neil S. Ostlund. *Modern Quantum Chemistry: Introduction to Advanced Electronic Structure Theory*. Dover Publications, 1982. Includes details on atomic units used in DFT and quantum chemistry.

[68] Max Born and Robert Oppenheimer. Zur quantentheorie der molekeln. *Annalen der Physik*, 389(20):457–484, 1927.

[69] D. R. Hartree. The wave mechanics of an atom with a non-coulomb central field. part i. theory and methods. *Mathematical Proceedings of the Cambridge Philosophical Society*, 24:89–110, 1928.

[70] V. Fock. Näherungsmethode zur lösung des quantenmechanischen mehrkörperproblems. *Zeitschrift für Physik*, 61:126–148, 1930.

[71] Robert G. Parr and Weitao Yang. *Density-Functional Theory of Atoms and Molecules*, volume 16 of *International Series of Monographs on Chemistry*. Oxford University Press, 1989.

[72] L. H. Thomas. The calculation of atomic fields. *Mathematical Proceedings of the Cambridge Philosophical Society*, 23:542–548, 1927.

[73] E. Fermi. Un metodo statistico per la determinazione di alcune proprietà dell'atomo. *Rendiconti Accademia Nazionale dei Lincei*, 6:602–607, 1927.

[74] Pierre Hohenberg and Walter Kohn. Inhomogeneous electron gas. *Physical Review*, 136:B864–B871, 1964.

[75] Walter Kohn and Lu Jeu Sham. Self-consistent equations including exchange and correlation effects. *Physical Review*, 140:A1133–A1138, 1965.

[76] S. H. Vosko, L. Wilk, and M. Nusair. Accurate spin-dependent electron liquid correlation energies for local spin density calculations: a critical analysis. *Canadian Journal of Physics*, 58(8):1200–1211, 1980.

[77] D. M. Ceperley and B. J. Alder. Ground state of the electron gas by a stochastic method. *Physical Review Letters*, 45:566–569, 1980.

[78] John P. Perdew, Kieron Burke, and Matthias Ernzerhof. Generalized gradient approximation made simple. *Physical Review Letters*, 77(18):3865–3868, 1996.

[79] V. I. Anisimov, J. Zaanen, and O. K. Andersen. The electronic structure of strongly correlated materials. *Physical Review B*, 44(3):943–954, 1991.

[80] John P. Perdew, Kieron Burke, and Matthias Ernzerhof. Generalized gradient approximation made simple. *Physical Review Letters*, 82(12):2544–2547, 1999.

[81] Jian Tao, John P. Perdew, and Kieron Burke. Climbing the density functional ladder: Nonempirical meta-gga functionals. *Physical Review Letters*, 91:146401, 2003.

[82] A. D. Becke and E. R. Johnson. A simple effective potential for exchange and correlation. *The Journal of Chemical Physics*, 124(22):221101, 2006.

[83] E. R. Johnson and A. D. Becke. A post-hartree-fock method for the exchange–correlation functional in density functional theory. *The Journal of Chemical Physics*, 131:224106, 2009.

[84] Y. Zhao and D. G. Truhlar. The m06 suite of density functionals for main group thermochemistry, kinetics, and noncovalent interactions. *Journal of Chemical Physics*, 125:194101, 2006.

[85] Vladimir Staroverov, John P. Perdew, and Gustavo Scuseria. Revised tao-perdew-staroverov-scuseria functional for meta-gga. *Physical Review B*, 70:024101, 2004.

[86] Yao Sun, Yang Weitao, Luan X., and Perdew John P. R2scan: A robust functional for materials science. *Journal of Chemical Physics*, 152:164106, 2020.

[87] Yao Sun, John P. Perdew, and Weitao Yang. Strongly constrained and appropriately normed density functional. *Physical Review Letters*, 115:036402, 2015.

[88] A. D. Becke. Density-functional thermochemistry. iii. the role of exact exchange. *The Journal of Chemical Physics*, 98:5648–5652, 1993.

[89] J. Heyd, G. E. Scuseria, and M. Ernzerhof. Hybrid functionals based on a screened coulomb potential. *The Journal of Chemical Physics*, 118(18):8207–8215, 2003.

[90] C. Adamo and V. Barone. Toward reliable density functional methods without adjustable parameters: The pbe0 model. *The Journal of Chemical Physics*, 116(4):1773–1783, 2002.

[91] N. Troullier and J. L. Martins. Efficient pseudopotentials for plane-wave calculations. *Physical Review B*, 43(3):1993–2006, 1991.

[92] D. Vanderbilt. Soft self-consistent pseudopotentials in a generalized eigenvalue formalism. *Physical Review B*, 41(11):7892–7895, 1990.

[93] L. Kleinman and D. M. Bylander. Efficacious form for model pseudopotentials. *Physical Review Letters*, 48:1425–1428, 1982.

[94] M. C. Payne, M. P. Teter, D. C. Allan, T. A. Arias, and J. D. Joannopoulos. Iterative minimization techniques for ab initio total-energy calculations: Molecular dynamics and conjugate gradients. *Review of Modern Physics*, 64:1045–1097, 1992.

[95] P. E. Blöchl. Projector augmented-wave method. *Physical Review B*, 50:17953–17979, 1994.

[96] Richard M. Martin. *Electronic Structure: Basic Theory and Practical Methods*. Cambridge University Press, 2004.

[97] H. J. Monkhorst and J. D. Pack. Special points for brillouin-zone integrations. *Physical Review B*, 13(12):5188–5192, 1976.

[98] Georg Kresse and Jürgen Hafner. Ab initio molecular dynamics for liquid metals. *Physical Review B*, 47:558–561, 1993.

[99] Georg Kresse and David Joubert. From ultrasoft pseudopotentials to the projector augmented-wave method. *Physical Review B*, 59:1758–1775, 1999.

[100] J. Furthmüller G. Kresse. Efficiency of ab-initio total energy calculations for metals and semiconductors using a plane-wave basis set. *Computational Materials Science*, 6:15–50, 1996.

[101] A. Togo, F. Oba, and I. Tanaka. First-principles calculations of the ferroelastic transition between rutile-type and baddeleyite-type zro2 at high pressures. *Physical Review B*, 78:134106, 2008.

[102] A. Togo and I. Tanaka. First principles phonon calculations in materials science. *Scripta Materialia*, 108:1–5, 2015.

[103] Phonopy Developers. Phonopy: A code for phonon calculations. https://phonopy.github.io/, 2024.

[104] Atsushi Togo, Laurent Chaput, Terumasa Tadano, and Isao Tanaka. Implementation strategies in phonopy and phono3py. *J. Phys. Condens. Matter*, 35(35):353001, 2023.

[105] Atsushi Togo. First-principles phonon calculations with phonopy and phono3py. *J. Phys. Soc. Jpn.*, 92(1):012001, 2023.

[106] Z. Gajek, M. S. K. R. S. L. M., and J. D. D. B. Site occupation disorder in alloys and its role in alloy properties. *Journal of Alloys and Compounds*, 475:134–141, 2009.

[107] SOD Developers. Site occupation disorder (sod) package. https://sod-package.github.io/, 2024.

[108] R. Poirier, R. Debernardi, and B. J. Johnson. The impact of site-occupation disorder on the electronic properties of metal alloys. *Journal of Materials Science*, 50:3340–3348, 2015.

[109] G. K. H. Madsen and D. J. Singh. Boltztrap: A code for calculating the electrical transport properties of materials. *Computer Physics Communications*, 175:67–71, 2006.

[110] Georg K. H. Madsen, Jesús Carrete, and Matthieu J. Verstraete. BoltzTraP2, a program for interpolating band structures and calculating semi-classical transport coefficients. *Comput. Phys. Commun.*, 231:140 – 145, 2018.

[111] Georg K.H. Madsen, Jesús Carrete, and Matthieu J. Verstraete. Boltztrap2, a program for interpolating band structures and calculating semi-classical transport coefficients. *Computer Physics Communications*, 231:140–145, 2018.

[112] BoltzTraP2 Developers. Boltztrap2: A code for transport property calculations. https://boltztrap2.github.io/, 2024.

[113] Vei Wang, Nan Xu, Jin-Cheng Liu, Gang Tang, and Wen-Tong Geng. Vaspkit: A user-friendly interface facilitating high-throughput computing and analysis using vasp code. *Computer Physics Communications*, 267:108033, 2021.

[114] C.S. Becquart and C. Domain. Ab initio calculations about intrinsic point defects and he in w. *Nuclear Instruments and Methods in Physics Research Section B: Beam Interactions with Materials and Atoms*, 255(1):23–26, 2007. Computer Simulation of Radiation Effects in Solids.

[115] Christoph Freysoldt, Blazej Grabowski, Tilmann Hickel, Jörg Neugebauer, Georg Kresse, Anderson Janotti, and Chris G. Van De Walle. First-principles calculations for point defects in solids. *Reviews of Modern Physics*, 86(1):253–305, 2014.

[116] J. P. Perdew, A. Ruzsinszky, G. I. Csonka, O. A. Vydrov, G. E. Scuseria, L. A. Constantin, X. Zhou, and K. Burke. Restoring the density-gradient expansion for exchange in solids and surfaces. *Physical Review Letters*, 100(13):136406, 2008.

[117] Christoph Freysoldt, Jörg Neugebauer, and Chris G. Van De Walle. Fully ab initio finite-size corrections for charged-defect supercell calculations. *Physical Review Letters*, 102:016402, 2009.

[118] Fedwa El-Mellouhi and Normand Mousseau. Self-vacancies in gallium arsenide: An ab initio calculation. *Physical Review B*, 71(12):125207, 2005.

[119] F. Mandl. *Statistical Physics*. Wiley, London, 1971. Page 88.

[120] Jianwei Sun, Adrienn Ruzsinszky, and John P. Perdew. Strongly constrained and appropriately normed semilocal density functional. *Physical Review Letters*, 115(3):036402, 2015.

[121] International Union of Pure and Applied Chemistry. Periodic table of the elements. `https://iupac.org/what-we-do/periodic-table-of-elements/`, 2021. Accessed 2025-12-22.

[122] Xuelian Luo, Xiuwen Zhang, and Alex Zunger. The role of native defects in half-heusler thermoelectric materials. *Advanced Functional Materials*, 29(20):1808104, 2019.

[123] Kulwinder Kaur and Ranjan Kumar. Giant thermoelectric performance of novel tairsn half heusler compound. *Physics Letters A*, 381(44):3760–3765, 2017.

[124] S Chibani, O Arbouche, M Zemouli, K Amara, Y Benallou, Y Azzaz, B Belgoumene, A Bentayeb, and M Ameri. Ab initio prediction of the structural, electronic, elastic,

and thermoelectric properties of half-heusler ternary compounds tiirx (x= as and sb). *Journal of electronic materials*, 47(1):196–204, 2018.

[125] Yonggang G. Yu, Xiuwen Zhang, and Alex Zunger. Natural off-stoichiometry causes carrier doping in half-heusler filled tetrahedral structures. *Phys. Rev. B*, 95:085201, Feb 2017.

[126] Max Born and Kun Huang. *Dynamical Theory of Crystal Lattices*. Oxford University Press, 1954.

[127] S. I. Ranganathan and M. Ostoja-Starzewski. Universal elastic anisotropy index. *Physical Review Letters*, 101(5):055504, 2008.

[128] Stephen L. Adler. Quantum theory of the dielectric constant in real solids. *Physical Review*, 126(2):413–420, 1962.

[129] Marat Valiev and John H. Weare. The projector-augmented plane wave method applied to molecular bonding. *The Journal of Physical Chemistry A*, 103(49):10588–10601, 1999.

[130] Golokesh Santra and Jan Martin. Pure and hybrid scan, rscan, and r2scan: which one is preferred in ks- and hf-dft calculations, and how does d4 dispersion correction affect this ranking? *Molecules*, 27:141, 12 2021.

[131] R Grau-Crespo, S Hamad, C R A Catlow, and N H de Leeuw. Symmetry-adapted configurational modelling of fractional site occupancy in solids. *Journal of Physics: Condensed Matter*, 19(25):256201, may 2007.

[132] Ricardo Grau-Crespo, Said Hamad, C. Richard A. Catlow, and Nora H. de Leeuw. Symmetry-adapted configurational modelling of fractional site occupancy in solids. *Journal of Physics: Condensed Matter*, 19(25):256201, 2007.

[133] S Kumar, Durgesh Kumar Sharma, and S Auluck. Stability, electronic, and optical properties of wurtzite cu 2 cd x zn 1- x sns 4 alloys as photovoltaic materials: First-principles insight. *Physical Review B*, 94(23):235206, 2016.

[134] Meena Rittiruam, Allan Abraham B. Padama, Athorn Vora-ud, Anucha Yangthaisong, Tosawat Seetawan, and Wilson Agerico Diño. Dilute concentrations of sb (bi) dopants in sn-site enhance the thermoelectric properties of tinisn half-heusler

alloys: a first-principles study. *Japanese Journal of Applied Physics*, 59(3):035003, feb 2020.

[135] Scott Kirklin, James E. Saal, Bryce Meredig, Alex Thompson, Jeff W. Doak, Muratahan Aykol, Stephan Rühl, and Chris Wolverton. The open quantum materials database (oqmd): Assessing the accuracy of dft formation energies. *npj Computational Materials*, 1(1):15010, 2015.

[136] S. Baroni, S. de Gironcoli, A. Dal Corso, and P. Giannozzi. Phonons and related crystal properties from density-functional perturbation theory. *Reviews of Modern Physics*, 73(2):515–562, 2001.

[137] Claudia Ambrosch-Draxl and Jorge O. Sofo. Linear optical properties of solids within the full-potential linearized augmented planewave method. *Computer Physics Communications*, 175(1):1–14, 2006.

[138] Pratik R. Raghuvanshi, Debayan Bhattacharjee, and Arindam Bhattacharya. Self-doping for synergistically tuning the electronic and thermal transport coefficients in n-type half-heuslers. *ACS Applied Materials Interfaces*, 13(46):55060–55071, 2021.

[139] Djallal Eddine Mellah, Kamel Demmouche, and Djamel Bezzerga. Strain effects on electronic and dynamical properties of half-heusler semiconductors: insights from meta-gga. *Physica Scripta*, 99(6), 2024.

[140] Muyiwa K Bamgbose. First-principles study of electronic structure and thermoelectric properties of p-type xirsb (x= ti, zr and hf) half-heusler compounds. *Materials Science in Semiconductor Processing*, 129:105792, 2021.

[141] Yassine Benallou, Kadda Amara, Bendouma Doumi, Omar Arbouche, Mostefa Zemouli, B Bekki, and Allel Mokaddem. Structural stability, electronic structure, and novel transport properties with high thermoelectric performances of zrirx (x== as, bi, and sb). *Journal of Computational Electronics*, 16:1–11, 2017.

[142] Shunji Ozaki and Sadao Adachi. Optical constants of znsxse1-x ternary alloys. *Journal of Applied Physics*, 75(11):7470–7475, 06 1994.

[143] John S. Toll. Causality and the dispersion relation: Logical foundations. *Phys. Rev.*, 104:1760–1770, Dec 1956.

[144] S. Saib, N. Bouarissa, P. Rodríguez-Hernández, and A. Muñoz. Structural and dielectric properties of aln under pressure. *Physica B: Condensed Matter*, 403(21):4059–4062, 2008.

[145] Eduardo Cisternas, Rodrigo Aguilera-del Toro, Faustino Aguilera-Granja, and Eugenio E Vogel. Effect of substitutional metallic impurities on the optical absorption properties of tio2. *Nanomaterials*, 14(14):1224, 2024.

[146] G Jeffrey Snyder and Eric S Toberer. Complex thermoelectric materials. *Nature materials*, 7(2):105–114, 2008.